



DARK MATTER AND VACUUM STABILITY IN A
3-LOOP RADIATIVE SEESAW MODEL

MASTER'S THESIS

Tim Huesmann

Universität Münster
Institute of Theoretical Physics
AG Klasen

First Examiner: Prof. Dr. Michael Klasen
Second Examiner: Jun.-Prof. Dr. Kai Schmitz

Münster, August 25, 2025

Contents

1	Introduction	1
2	Dark Matter	3
2.1	Evidence	3
2.2	Dark matter candidates	5
2.2.1	Properties of dark matter particles	5
2.2.2	Dark matter candidates	6
2.3	Genesis of dark matter	6
3	Neutrinos	9
3.1	Neutrinos in the Standard Model	9
3.2	Neutrino oscillations	10
3.3	Neutrino experiments	13
4	Scotogenic Model	15
4.1	Particle content	15
4.2	Neutrino masses	16
4.3	Dark matter	18
4.4	Vacuum stability	18
4.5	Lepton flavor violation	19
5	Numerical Analysis of the Scotogenic Model	21
5.1	Tool chain	21
5.2	Constraints	23
5.2.1	Theoretical constraints	23
5.2.2	Experimental constraints	23
5.3	The viable parameter space	24
5.4	Analysis of the RGE effects	25
6	KNT-Model	31
6.1	Particle content	31

6.2	Neutrino mass	32
6.3	Parametrization of the Yukawa couplings	33
6.4	Dark matter	35
6.5	Vacuum stability	35
6.6	Lepton flavor violation	37
7	Numerical Analysis of the KNT-Model	39
7.1	Constraints	39
7.1.1	Theoretical Constraints	39
7.1.2	Experimental Constraints	39
7.2	Ranges of the parameters	40
7.3	Viable Parameter Space	42
7.4	Analysis of the RGE-effects	42
7.5	Influence of the scalar couplings on the RGEs	47
8	Conclusion	53
A	Lepton Flavor Violation	55
A.1	Scotogenic Model	58
A.2	KNT-Model	59
B	Methods	61
B.1	Monte-Carlo-Markov-Chain	61
B.1.1	MCMC	61
B.1.2	Ensemble Sampler	65
B.2	Importance Sampling	76
B.3	Normalizing Flows	77
C	RGEs of the Scotogenic Model	81
C.1	Gauge couplings	81
C.2	Yukawa couplings	82
C.3	Quartic scalar couplings	82
D	RGEs of the KNT-Model	83
D.1	Gauge couplings	83
D.2	Yukawa coupling	84
D.3	Quartic scalar couplings	84
	Bibliography	85

1 Introduction

The Standard Model of particle physics is one of the most successful theoretical frameworks in science. It was able to explain a wide range of observed phenomena and to predict new particles, which were then found experimentally. The crowning achievement of the Standard Model was the discovery of the Higgs boson at the LHC in 2012 [[1],[2]]. This was the last missing particle predicted by the Standard Model, and its discovery confirmed the mechanism of electroweak symmetry breaking and mass generation for charged fermions and gauge bosons. Despite all these successes, the Standard Model is not a complete description of all fundamental interactions because it does not feature gravity. In addition, there are also some phenomena in particle physics, which are not explained by the Standard Model. Thus, there is evidence that motivates extensions to the Standard Model.

This thesis deals with two open questions of particle physics. One of these questions is the nature of dark matter. Many astrophysical observations give evidence that there has to be a form of matter which does not interact electromagnetically, but its presence can be deduced from its gravitational effect. However, dark matter particles have not been detected yet. Hence, we do not know the structure of dark matter, but the Standard Model does not provide a suitable dark matter candidate. Therefore, the evidence of dark matter is a good motivation to go beyond the Standard Model.

Another open question of particle physics is the origin of neutrino masses. In the Standard Model, neutrinos are massless. In contrast to that, the discovery of neutrino oscillations [[3],[4]] gives evidence that neutrinos are actually massive. This shows that there is still a missing piece in the Standard Model which explains neutrino masses.

An elegant explanation for the origin of neutrino masses is given by the so-called seesaw mechanisms. Seesaw models typically introduce heavy degrees of freedom, such as right-handed neutrinos or scalar triplets, and generate neutrino masses at tree level through effective dimension-five operators. One problem of these models is that the new particles have to carry large masses to obtain the tiny neutrino masses. Thus, their mass scales are far beyond the experimental reach, making it impossible to find them experimentally and confirm the model.

In this thesis, we study radiative seesaw models. These models generate neutrino masses at

loop-level. Therefore, the smallness of the neutrino masses can be explained by loop suppression and the masses of the new particles can be smaller compared to conventional seesaw models. The masses of the new particles are typically in the TeV regime. Furthermore, some of the introduced particles in these models are suitable dark matter candidates.

This thesis is structured as follows. In Chapter 2, we present evidence for dark matter. In addition, we explain the properties dark matter candidates have to satisfy and present some dark matter candidates. At the end of this chapter, we also explain the genesis of dark matter, where we focus on the freeze-out mechanism. Chapter 3 deals with neutrinos. There, we explain why neutrinos are massless in the Standard Model and how the existence of their masses is deduced from the discovery of neutrino oscillations. We also mention some relevant experiments for this discovery. Chapter 4 introduces the Scotogenic Model [[5],[6]]. There, the new particle content is given and the neutrino mass generation is explained. Furthermore, we mention the suitable dark matter candidates in this model, derive the conditions to satisfy vacuum stability, and explain lepton flavor violating processes in this model. In Chapter 5 we deal with the numerical analysis of the Scotogenic Model. Therefore, we explain the setup used for the analysis and show the viable parameter space of the model. After that, we analyze the effects of the renormalization group equation on the viable parameter space. Chapter 6 introduces the KNT-Model [7] and explains the neutrino mass generation in this model. As for the Scotogenic Model, we also mention the suitable dark matter candidates, derive the vacuum stability conditions and explain lepton flavor violating processes. After that, we also perform a numerical analysis for the KNT-Model, where we scan the viable parameter space and analyze the effects of the renormalization group evolution. This is done in Chapter 7. In the end, we draw our conclusion in Chapter 8.

2 Dark Matter

Dark matter is a form of matter that does not interact with electromagnetic radiation. The structure of dark matter is one of the biggest open questions in particle physics, because until today dark matter has not been detected yet, although there is much evidence for such a kind of matter. Throughout the years, physicists have come up with many approaches to explain dark matter.

2.1 Evidence

The history of the discovery of dark matter in the Universe goes back to Fritz Zwicky. In 1933 he studied the redshifts of galaxy clusters to obtain the radial velocities of these galaxies. Throughout his work, he found that the Coma cluster had a large velocity dispersion. Because of this observation, he used the virial theorem to estimate the mass of the cluster. The virial theorem claims that the radial velocity v depends on the distance from the center r and the mass contained within this distance $M(r)$ in the following way

$$v(r) = \sqrt{\frac{GM(r)}{r}}. \quad (2.1)$$

Zwicky found that the estimated mass of the Coma cluster is larger than the observed mass. He concluded that there has to be a certain amount of non luminous matter[8]. Three years later, Smith observed the same phenomenon while studying the Virgo cluster[9]. This phenomenon can be observed for different galaxies, for example the M33 galaxy, which is shown in Figure 2.1 taken from [10]. There, the observed rotation curve and the expected rotation curve without considering dark matter are shown. It can be seen that these curves differ from each other and that the observed velocities are much higher than the expected ones, but the observed rotation still shows a $\frac{1}{\sqrt{r}}$ -proportionality. Thus, it is still possible that this behavior can be described by the virial theorem if one considers a higher mass density. This leads to the conclusion that there should be a form of matter that has not been detected yet.

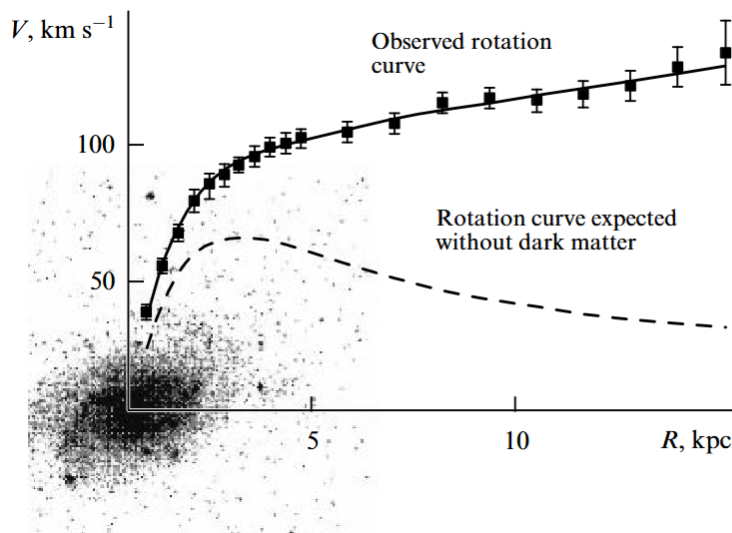


Figure 2.1: Decomposition of the rotation curve of the M33 galaxy taken from Ref. [10]

Another evidence for the existence of dark matter comes from observations of cluster collisions, which are known as bullet clusters. The biggest part of baryonic matter in a bullet cluster consists of hot gas. Hence, it is possible to obtain its mass distribution by X-ray emission. The total mass distribution can be measured via gravitational lensing. The X-ray image and the total mass distribution of a bullet cluster are shown in Figure 2.2 taken from [11]. The distribution of the hot gas and the total mass distribution differ from each other and the Figure shows that dark matter and baryonic matter have to be spatially separated from each other to reach this total mass distribution. This is a special feature of bullet clusters, because the hot gas of the two colliding galaxies interacts with itself while the dark matter particles experience negligible interactions with each other and the visible matter. Thus, the hot gas experiences a collisional shock wave and the dark matter clouds of the two systems just pass through each other, which leads to spatial separation. This observation puts strict constraints on alternative interpretations, in which dark matter is replaced by modifications of gravity because those modifications cannot be separated from visible matter.

Another good evidence for the existence of dark matter is the cosmic microwave background because of its observed temperature fluctuations, which are an imprint of primordial density fluctuations. Dark matter does not interact with photons. It only influences via gravity, while baryonic matter interacts with photons via radiation pressure. Hence, dark matter contributes to the gravitational pull without having an effect on the radiation pressure. Therefore, it deepens the gravitational well, which changes the balance of acoustic oscillations. A model, which explains the CMB spectrum very well, is the Λ CDM model, which includes dark matter and dark energy. Fitting the data with this model shows that

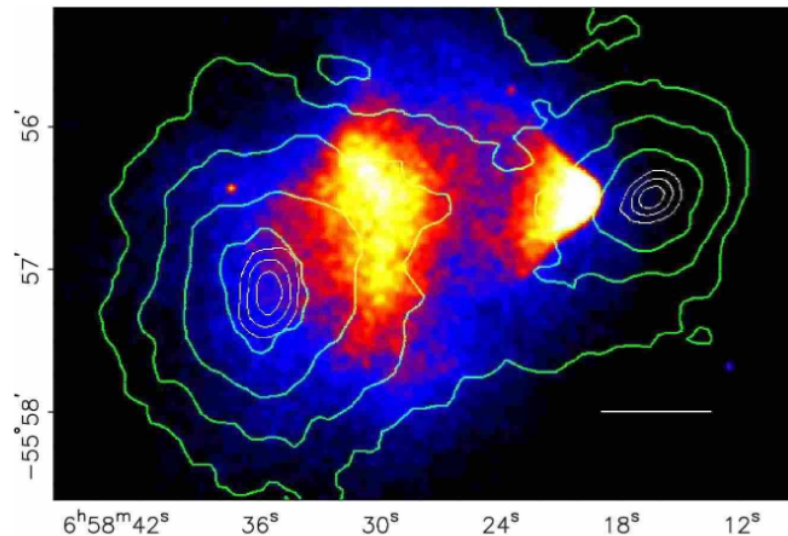


Figure 2.2: The collision of a pair of clusters of galaxies, with the colored map representing the X-ray image of the hot baryonic gas. This is displaced from the distribution of the total mass reconstructed through weak lensing, shown with green contours. The white bar corresponds to the length of 200 kpc. From Clowe et al. (2006) in [11]

the matter of the universe consists of 5% baryonic matter, 25% dark matter and 70% dark energy. The most recent measurements lead to a relic abundance of $\Omega h^2 = 0.120 \pm 0.001$ for dark matter.

2.2 Dark matter candidates

2.2.1 Properties of dark matter particles

Throughout the years, people came up with different approaches to explain dark matter. Since dark matter has not been detected yet, there is still a lot of free space to integrate dark matter into your theory, but there are still some properties that all these approaches have to satisfy.

First of all dark matter candidates are not able to carry an electric charge because otherwise they would interact with electromagnetic radiation. In this case, dark matter would be visible and would have been detected. Additionally, dark matter particles have to be stable for a time longer than the universe because it is still abundant in the presence, which is shown by the evidence. Another property of dark matter is that it has to be non-relativistic because it should be able to build structure formation, which is not possible if the particles are relativistic because of their speed. There are also limits on the mass of dark matter candidates. The lower limit arises from the request that the De Broglie wavelength of a dark

matter particle has to fit within the small gravitationally bound of dwarf galaxies [12]. Thus, the lower limit of the dark matter mass is $2.2 \cdot 10^{-21}$ eV. The upper limit of dark matter has to be smaller than the mass of a small dwarf galaxy, which is known to be the smallest astrophysical structure for hosting dark matter. These galaxies typically have masses on the order of a few 10^5 solar masses. Hence, the span of dark matter mass M is given by

$$10^{-21} \text{ eV} < M < 10^{37} \text{ kg} . \quad (2.2)$$

The Standard Model particles, which come closest to the required properties of dark matter are neutrinos, because they are neutral and stable, but the experimental bounds on their tiny masses require that they move at relativistic speeds during the early stages of structure formation in the universe. Thus, the Standard Model neutrinos are not suitable dark matter candidates and many scientists assume that dark matter is made of one or more undiscovered particles. This is why they come up with models beyond the Standard Model to explain dark matter.

2.2.2 Dark matter candidates

Historically, there have been many approaches to explaining dark matter. One approach is to modify the theory of gravity, which results in a theory like MOND [13]. Other approaches try to explain the observations by suggesting a dark matter candidate. These approaches range from suggesting very massive dark matter candidates like MACHOs and primordial blackholes to particle dark matter in the form of axions or WIMPs. Some historic dark matter candidates are given in Table 2.1 taken from [14].

In this thesis, we focus on WIMPs as dark matter candidate. WIMPs are weakly interacting massive particles. In our case, WIMPs appear in minimal models with only a few free parameters. WIMPs satisfy the above mentioned criteria very well. Their mass is usually of the order $\mathcal{O}(100 \text{ GeV})$ because they yield the correct relic density in this case [15]. Additionally, they are stable, which is satisfied through an additional symmetry. In our minimal models, stability is guaranteed via a \mathbb{Z}_2 -Symmetry.

2.3 Genesis of dark matter

The dark matter relic density can be produced via different mechanisms. The most famous is the freeze-out mechanism. This is also the mechanism which is considered responsible for the relic density in this thesis. Here, we briefly explain the formalism of this mechanism which

Candidate	Date	Reference(s)
Primordial BH	1966, 1971	Zeldovich & Novikov, Hawking [16]
MACHOs	1981, 1986	Petrou; Paczynski [17]
Gravitinos	1981, 1982	Fayet; Witten; Pagel & Primack [18]
Axions	1983	Preskill, Wise & Wilczek [19]
Neutralinos	1984	Ellis et al. [20]
Strangelets	1984	Witten; Fahri & Jaffe [[21], [22]]
Q -balls	1984	Witten [23]
Extra-dimensional DM	1984	Kolb & Slansky; Servant & Tait [24]
WIMPs	1985	Steigman & Turner [25]
Sterile neutrinos	1993	Dodelson & Widrow [26]
Fuzzy DM	2000	Hu, Barkana & Gruzinov [27]
Sub-GeV DM	2003	Boehm, Fayet et al. [28]

Table 2.1: List of some historic dark matter candidates taken from [14]

is given in [29].

In this scenario, it is considered that the dark matter density is in thermal equilibrium after the big bang, which means that the amount of dark matter which is produced and annihilated is the same. In this case, the number density n_{eq} is proportional to T^3 with T being the temperature of the universe. After the big bang, the universe expands and the temperature drops down. At some point the energy is too low to produce dark matter particles, but the annihilation still continues at this point. In the case that the expansion is slow enough to maintain the equilibrium, the number density would be given by

$$n_{eq} = g \left(\frac{m_\chi T}{2\pi} \right)^{\frac{3}{2}} e^{-\frac{m_\chi}{T}} . \quad (2.3)$$

Here, m_χ is the dark matter mass and g is the number of degrees of freedom. In reality, the universe expands too fast to maintain equilibrium and n_{eq} is not the real number density. The evolution of the number density is described by the Boltzmann equation

$$\dot{n}(t) = 3H(t)n(t) = -\langle \sigma_{\chi\chi} v \rangle [n(t)^2 - n_{eq}(t)^2] . \quad (2.4)$$

Here, $H(t)$ is the Hubble parameter and $\langle \sigma_{\chi\chi} v \rangle$ is the thermally averaged dark matter self annihilation cross section which is given by

$$\langle \sigma_{12 \rightarrow 34} v \rangle = \frac{\int d^3 p_1 \int d^3 p_2 \sigma_{12 \rightarrow 34} v n_{eq1} n_{eq2}}{\int d^3 p_1 \int d^3 p_2 n_{eq1} n_{eq2}} . \quad (2.5)$$

The indices 1, 2 represent the educts and 3, 4 the products of the process. The velocity v is given by

$$v = \frac{\sqrt{(p_1 \cdot p_2 - m_1^2 m_2^2)}}{E_1 E_2} . \quad (2.6)$$

In our case, the annihilation process has the form $\chi\chi \rightarrow \phi\phi$, where ϕ represents Standard Model particles. Furthermore, we can rewrite the Boltzmann equation by introducing new quantities $Y = \frac{n}{s}$ and $x = \frac{m_\chi}{T}$. Here, s is the entropy which is proportional to T^3 and its evolution is given by

$$\frac{ds}{dt} + 3Hs = 0 . \quad (2.7)$$

Using the new quantities and $\frac{dT}{dt} = -HT$ allows us to rewrite the Boltzmann equation as follows

$$\frac{x}{Y_{eq}} \frac{dY}{dx} = -\frac{n_{eq} \langle \sigma_{\chi\chi \rightarrow \phi\phi} v \rangle}{H} \left(\frac{Y^2}{Y_{eq}^2} - 1 \right) . \quad (2.8)$$

In principle, the Boltzmann equation has to be solved numerically, but it is possible to determine an analytical expression for the relic density using some approximations given in [29]

$$\Omega h^2 \approx 0.12 \frac{x_{fo} 1.43 \cdot 10^{-9} \text{ GeV}^{-2}}{20 \langle \sigma_{\chi\chi \rightarrow \phi\phi} v \rangle} . \quad (2.9)$$

Freeze-out generally occurs in the range $x_{fo} = 20$ to $x_{fo} = 30$. Therefore, we see that the relic density is antiproportional to the thermally averaged cross section.

3 Neutrinos

One remaining question in particle physics is how neutrinos obtain their mass. In the Standard Model, neutrinos are massless, but the discovery of neutrino oscillations gives evidence that neutrinos are massive. This chapter explains why neutrinos do not carry a mass in the Standard Model and why neutrino oscillations give evidence for their mass. Furthermore, we also describe some experiments in this context. This chapter is based on [[30], Chapter 14]

3.1 Neutrinos in the Standard Model

In the Standard Model, all interactions are described by the gauge symmetry $SU(3)_c \times SU(2)_L \times U(1)_Y$. Additionally, the Standard Model contains three generations of massive fermions. There are five different representations of the gauge group for each generation

$$\left(1, 2, -\frac{1}{2}\right), \left(3, 2, \frac{1}{6}\right), \left(1, 1, -1\right), \left(3, 1, \frac{2}{3}\right), \left(3, 1, -\frac{1}{3}\right). \quad (3.1)$$

The matter content together with the corresponding representation is given in table 3.1. The electric charges of the particles are given by

$$Q_{EM} = T_{L3} + Y. \quad (3.2)$$

In addition to the matter content the Standard Model contains a Higgs doublet H with the charges $(1, 2, 1/2)$ and a vacuum expectation value (vev)

$$\langle H \rangle = \left(0, \frac{v}{\sqrt{2}}\right). \quad (3.3)$$

The vev breaks the gauge symmetry and after electroweak symmetry breaking the gauge group is $SU(3)_c \times U(1)_{EM}$. As shown in Table 3.1, neutrinos are singlets in this gauge group because they neither obtain a strong charge nor an electric charge. They only interact weakly. These neutrinos are called active neutrinos because they can interact with other Standard Model particles. As seen in Table 3.1, these neutrinos are left-handed. It is also possible to define right-handed neutrinos, which are singlets under the Standard Model gauge group with

the charges $(1, 1, 0)$. Thus, the right-handed neutrino would not interact with the Standard Model gauge bosons. This is why they are called sterile neutrinos and are not part of the Standard Model.

In the Standard Model, fermions obtain their masses through Yukawa interactions, which

$L_L(1,2,-1/2)$	$Q_L(3,2,1/6)$	$E_R(1,1,-1)$	$U_R(3,1,2/3)$	$D_R(3,1,-1/3)$
$(\nu_e, e)_L$	$(u,d)_L$	e_R	u_R	d_R
$(\nu_\mu, \mu)_L$	$(c,s)_L$	μ_R	c_R	s_R
$(\nu_\tau, \tau)_L$	$(t,b)_L$	τ_R	t_R	b_R

Table 3.1: Matter content of the Standard Model

couple the left-handed doublets with the Higgs doublet and the right-handed fields

$$\mathcal{L}_{\text{Yukawa}} = Y_{ij}^d \bar{Q}_{Li} H D_{Rj} + Y_{ij}^u \bar{Q}_{Li} \tilde{H} U_{Rj} + Y_{ij}^l \bar{L}_{Li} H E_{Rj} . \quad (3.4)$$

Here, the indices i, j are flavor indices and $\tilde{H} = i\tau_2 H^*$. These terms lead to the following fermion masses after electroweak symmetry breaking

$$m_{ij}^f = Y_{ij}^f \frac{v}{\sqrt{2}} . \quad (3.5)$$

This mechanism does not work for neutrinos because the Standard Model does not contain right-handed neutrinos as explained above. Hence, neutrinos cannot gain masses via Yukawa interactions in the Standard Model. In principle, it would be possible that neutrino masses occur at loop level, but this does not happen in the Standard Model because of an accidental lepton flavor number symmetry

$$U(1)_{L_e} \times U(1)_{L_\mu} \times U(1)_{L_\tau} . \quad (3.6)$$

The only possible neutrino mass term in the Standard Model is proportional to $\bar{L}_L L_L^C$, which would break the lepton number symmetry. That is why the existence of neutrino masses is a good motivation to go beyond the Standard Model.

3.2 Neutrino oscillations

There are three different neutrino flavors and they are able to transform into each other. This phenomenon is called neutrino oscillation. Experimental evidence for this phenomenon was found in the Super-Kamiokande-Experiment [3] and in the Sudbury Neutrino Observatory [4]. The oscillation of the interacting (flavor) eigenstates of neutrinos is only possible if the propagating (mass) eigenstates are not the same as the interacting eigenstates. Thus, the

discovery of neutrino oscillations gives evidence for massive neutrinos. The flavor eigenstates $|\nu_\alpha\rangle$ and the mass eigenstates $|\nu_i\rangle$ can be transformed into each other by the neutrino mixing matrix, which is called Pontecorvo-Maki-Nakagawa-Sakata-Matrix (PMNS-Matrix) U_{PMNS}

$$\begin{aligned} |\nu_\alpha\rangle &= \sum_{i=1}^3 (U_{\text{PMNS}}^*)_{\alpha i} |\nu_i\rangle \\ |\nu_i\rangle &= \sum_{\alpha=1}^3 (U_{\text{PMNS}})_{i\alpha} |\nu_\alpha\rangle . \end{aligned} \quad (3.7)$$

If we want to calculate the probability for neutrino oscillations, we have to look at the evolution of a flavor eigenstate after traveling a distance L ($L \approx ct$ for relativistic neutrinos)

$$|\nu_\alpha(t)\rangle = \sum_{i=1}^3 (U_{\text{PMNS}}^*)_{\alpha i} |\nu_i(t)\rangle . \quad (3.8)$$

Now we assume that $|\nu\rangle$ is a plane wave and its time evolution is given by

$$|\nu_i(t)\rangle = e^{-iE_i t} |\nu_i(0)\rangle , \text{ with } E_i = \sqrt{p_i^2 + m_i^2} . \quad (3.9)$$

The probability $P_{\alpha\beta}$, that a neutrino of flavor α oscillates into a neutrino of flavor β is given by

$$\begin{aligned} P_{\alpha\beta} &= |\langle \nu_\beta | \nu_\alpha(t) \rangle|^2 = \left| \sum_{i,j=1}^3 U_{\alpha i}^* U_{\beta j} \langle \nu_j | \nu_i(t) \rangle \right|^2 \\ &= \left| \sum_{i,j=1}^3 U_{\alpha i}^* U_{\beta j} e^{-iE_i t} \langle \nu_j | \nu_i \rangle \right|^2 . \end{aligned} \quad (3.10)$$

Now we can use the identity $\langle \nu_j | \nu_i \rangle = \delta_{ij}$, which gives us

$$P_{\alpha\beta} = \left| \sum_{i=1}^3 U_{\alpha i}^* U_{\beta i} e^{-iE_i t} \right|^2 \quad (3.11)$$

$$= \sum_{i,j=1}^3 U_{\alpha i}^* U_{\beta i} U_{\alpha j} U_{\beta j}^* e^{-i(E_i - E_j)t} . \quad (3.12)$$

For relativistic neutrinos, we get $p_i \approx p_j \equiv p \approx E$. Thus, we are able to approximate the energy

$$E_i = \sqrt{p_i^2 + m_i^2} \approx p + \frac{m_i^2}{2E} . \quad (3.13)$$

This approximation leads us to

$$e^{-i(E_i - E_j)t} \approx \cos\left(\frac{m_i^2 - m_j^2}{2E}t\right) - i \sin\left(\frac{m_i^2 - m_j^2}{2E}t\right). \quad (3.14)$$

Using this approximation, we can express $P_{\alpha\beta}$ as

$$\begin{aligned} P_{\alpha\beta} &= \delta_{\alpha\beta} - 2 \sum_{i,j=1}^3 \operatorname{Re}[U_{\alpha i}^* U_{\beta i} U_{\alpha j} U_{\beta j}^*] \sin^2(X_{ij}) \\ &+ \sum_{i,j=1}^3 \operatorname{Im}[U_{\alpha i}^* U_{\beta i} U_{\alpha j} U_{\beta j}^*] \sin(2X_{ij}) \end{aligned} \quad (3.15)$$

with

$$X_{ij} = \frac{(m_i^2 - m_j^2)L}{4E}. \quad (3.16)$$

These equations show that the oscillation depends on the mass differences between the neutrinos and the entries of the PMNS-Matrix, but not on the absolute mass scale of the neutrinos. Even the mass hierarchy of neutrinos is still unknown. That is why there are two mass schemes, the normal hierarchy (NH) with

$$m_1 < m_2 < m_3 \quad (3.17)$$

and the inverted hierarchy (IH) with

$$m_3 < m_1 < m_2. \quad (3.18)$$

An illustration of the different mass hierarchies is shown in Figure 3.1

The PMNS-Matrix can be parametrized by three angles $\theta_{12}, \theta_{13}, \theta_{23}$ and three phases, the CP phase δ_{CP} and two Majorana phases α_1, α_2

$$U_{\text{PMNS}} = \begin{pmatrix} 1 & 0 & 0 \\ 0 & c_{23} & s_{23} \\ 0 & -s_{23} & c_{23} \end{pmatrix} \begin{pmatrix} c_{13} & 0 & s_{13}e^{-i\delta_{CP}} \\ 0 & 1 & 0 \\ -s_{13}e^{i\delta_{CP}} & 0 & c_{13} \end{pmatrix} \begin{pmatrix} c_{12} & s_{12} & 0 \\ -s_{12} & c_{12} & 0 \\ 0 & 0 & 1 \end{pmatrix} \begin{pmatrix} e^{i\frac{\alpha_1}{2}} & 0 & 0 \\ 0 & e^{i\frac{\alpha_2}{2}} & 0 \\ 0 & 0 & 1 \end{pmatrix} \quad (3.19)$$

with $c_{ij} = \cos(\theta_{ij})$ and $s_{ij} = \sin(\theta_{ij})$. The neutrino oscillation parameters are probed in some experiments.

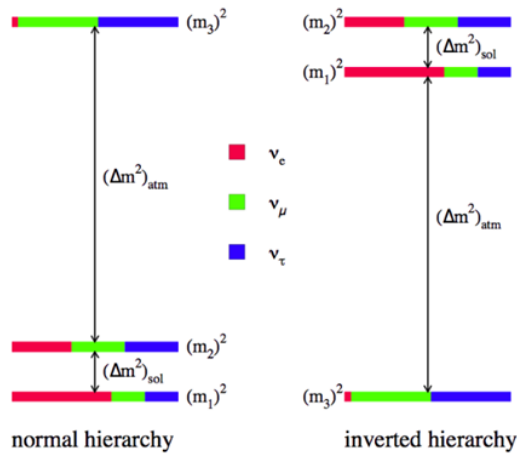


Figure 3.1: Pictorial representation of the possible neutrino mass hierarchies taken from [31].
 Note: Δm_{atm}^2 is equivalent to Δm_{32}^2 and Δm_{sol}^2 is equivalent to Δm_{21}^2 .

3.3 Neutrino experiments

Neutrino oscillations were studied by many experiments using different neutrino sources. The main neutrino sources are the sun, the earth's atmosphere, accelerators, and nuclear reactors. In the sun, electron neutrinos are produced in thermonuclear reactions, which generate solar energy. These electron neutrinos can oscillate into muon and tauon neutrinos. That is why the number of detected electron neutrinos from the sun is smaller than the theoretical prediction. This observation was a main step in the discovery of neutrino oscillations. Solar neutrino experiments are very sensitive to the upper row of the PMNS matrix because electron neutrinos are always involved in these experiments. Solar neutrino experiments are for example Super-Kamiokande and Borexino.

In the earth's atmosphere, neutrinos are produced in the decays of pions and kaons, which are generated by interactions of cosmic rays with nucleons in the atmosphere. The atmospheric neutrinos consist of all flavors. Some detectors for atmospheric neutrinos are, for example IceCube, ANTARES and KM3NeT.

Accelerator neutrinos are produced by collisions of high-energy protons with a target. In these collisions, pions and kaons are produced, which decay into neutrinos. The most abundant product in the collisions are pions. Thus, muon neutrinos are dominant in the neutrino beam coming from accelerators. The main experiments with accelerator neutrinos are K2K, T2K, MINOS and NO ν A.

Nuclear reactors are a good source of electron antineutrinos in the MeV energy region. These antineutrinos are generated in nuclear fissions of heavy isotopes like ^{235}U , ^{238}U , ^{239}Pu and ^{241}Pu . An experiment probing reactor neutrinos is, for example, KamLAND.

An overview of the experiments and their contribution to the neutrino oscillation parameters

is given in table 3.2, which is taken from [30]. The measured parameters are given in table 3.3 taken from [30].

Experiment	Dominant	Important
Solar Experiments	θ_{12}	$\Delta m_{21}^2, \theta_{23}$
Reactor LBL (KamLAND)	Δm_{21}^2	θ_{12}, θ_{13}
Reactor MBL (Daya-Bay, Reno, D-Chooz)	$\theta_{13}, \Delta m_{31,32}^2 $	$\theta_{23}, \Delta m_{31,32}^2 , \theta_{13}, \delta_{CP}$
Atmospheric Experiments (SK, IC-DC)		
Accel LBL $\nu_\mu, \bar{\nu}_\mu$, Disapp (K2K, MINOS, T2K, NO ν A)	$ \Delta m_{31,32}^2 , \theta_{23}$	
Accel LBL $\nu_e, \bar{\nu}_e$, Disapp (MINOS, T2K, NO ν A)	δ_{CP}	θ_{13}, θ_{23}

Table 3.2: Experiments contributing to the present determination of the oscillation parameters. Table taken from [30]

	Normal hierarchy	Inverted hierarchy
$\sin^2 \theta_{12}$	$0.307^{+0.013}_{-0.013}$	$0.307^{+0.013}_{-0.013}$
$\sin^2 \theta_{23}$	$0.558^{+0.015}_{-0.021}$	$0.553^{+0.016}_{-0.014}$
$\sin^2 \theta_{13}$	$0.0219^{+0.0007}_{-0.0007}$	$0.0219^{+0.0007}_{-0.0007}$
δ_{CP} [rad]	$1.19^{+0.22}_{-0.22}\pi$	$1.21^{+0.22}_{-0.22}\pi$
Δm_{21}^2 [10^{-5} eV 2]	$7.53^{+0.18}_{-0.18}$	$7.50^{+0.18}_{-0.18}$
Δm_{32}^2 [10^{-3} eV 2]	$+2.455^{+0.028}_{-0.028}$	$-2.529^{+0.029}_{-0.029}$

Table 3.3: The fit values for the neutrino oscillation parameters for both hierarchies taken from [30]

The neutrino oscillation experiments are not sensitive to the absolute neutrino mass scale because the absolute neutrino mass has no impact on the oscillations, but there is an experiment that tries to find the mass of the electron neutrino. This is the KATRIN experiment. If the mass of the electron neutrino is known, the other masses can be determined from the mass differences which are known from the oscillation experiments. The current upper limit measured by the KATRIN experiment is $m_{\nu e} < 0.45$ eV [32].

4 Scotogenic Model

The Scotogenic Model, proposed by Zhijian Tao in 1996 [5] and Ernest Ma in 2006 [6], is a simple extension of the standard model. In this model the left-handed neutrinos obtain masses from a one-loop radiative seesaw mechanism and the model also delivers a bosonic and a fermionic dark matter candidate.

4.1 Particle content

In the Scotogenic Model the standard model is extended by three generations of right-handed singlet fermions N_i and a scalar doublet η . Additionally, a \mathbb{Z}_2 -symmetry is introduced, under which all Standard Model particles are even and the new particles are odd. This symmetry implies that the lightest odd particle has to be stable. Thus, it is a suitable dark matter candidate, if it is neutral. The new particle content of the model is given in Table 4.1. The Lagrangian is extended by the following terms

$$\mathcal{L} = \mathcal{L}_{\text{SM}} - \frac{1}{2} M_i \bar{N}_i N_i^c + y_{ij} \bar{N}_i \eta L_j + h.c. + V(H, \eta) . \quad (4.1)$$

Here, L_j is the SU(2)-doublet for the j th lepton generation. $V(H, \eta)$ is the scalar potential, which is given by

$$\begin{aligned} V(H, \eta) = & m_H^2 H^\dagger H + m_\eta^2 \eta^\dagger \eta + \frac{\lambda_1}{2} (H^\dagger H)^2 + \frac{\lambda_2}{2} (\eta^\dagger \eta)^2 + \lambda_3 (H^\dagger H) (\eta^\dagger \eta) \\ & + \lambda_4 (H^\dagger \eta) (\eta^\dagger H) + \left(\frac{\lambda_5}{2} (\eta^\dagger H)^2 + h.c. \right) . \end{aligned} \quad (4.2)$$

H is the Standard Model Higgs doublet. Hence, m_H and λ_1 are the parameters known from the Standard Model Higgs potential. The \mathbb{Z}_2 -symmetry is considered unbroken and η does not require a vev. Therefore, we ensure that the lightest odd particle is stable even after symmetry breaking. After electroweak symmetry breaking (EWSB), there are four physical particles, the Standard Model Higgs boson h , the charged component of the other scalar

doublet η^\pm and two neutral components $\eta^0 = \frac{\eta_R + \eta_I}{\sqrt{2}}$. The squared masses of these particles are given by:

$$m_h^2 = \lambda_1 v^2 \quad (4.3)$$

$$m_\pm^2 = m_\eta^2 + \frac{1}{2} \lambda_3 v^2 \quad (4.4)$$

$$m_R^2 = m_\eta^2 + \frac{1}{2} (\lambda_3 + \lambda_4 + \lambda_5) v^2 \quad (4.5)$$

$$m_I^2 = m_\eta^2 + \frac{1}{2} (\lambda_3 + \lambda_4 - \lambda_5) v^2. \quad (4.6)$$

In this case, $v = 246.22$ GeV denotes the vacuum expectation value of the Standard Model Higgs.

Field	Generations	Spin	$U(1)_Y \times SU(2)_L \times SU(3)_c$	\mathbb{Z}_2
N	3	$\frac{1}{2}$	(0, 1, 1)	-1
η	1	0	$(\frac{1}{2}, 2, 1)$	-1
SM particles	-	-	-	+1

Table 4.1: Particle content of the scotogenic model.

4.2 Neutrino masses

In this model, neutrino masses are generated by a radiative seesaw mechanism through a one-loop interaction of the neutrinos with the Higgs boson. This is shown in Figure 4.1. The neutrino mass matrix is given by

$$(M_\nu)_{ij} = \sum_{k=1}^3 \frac{M_k y_{ki} y_{kj}}{32\pi^2} \left[\frac{m_R^2}{m_R^2 - M_k^2} \log\left(\frac{m_R^2}{M_k^2}\right) - \frac{m_I^2}{m_I^2 - M_k^2} \log\left(\frac{m_I^2}{M_k^2}\right) \right]. \quad (4.7)$$

This mass term will vanish if $\lambda_5 = 0$, because, as one could see in equation 4.6 $m_R = m_I$ if $\lambda_5 = 0$. This would lead to a larger symmetry, because the Majorana masses of the neutrinos violate lepton number conservation. Therefore, λ_5 can be considered small and the neutrino mass can be expanded for small λ_5 , which leads to the following expression for the neutrino mass with $m_R \approx m_I \equiv m_{R,I}$

$$(M_\nu)_{ij} = \sum_{k=1}^3 \frac{\lambda_5 v^2}{8\pi^2} \frac{M_k y_{ki} y_{kj}}{m_{R,I}^2 - M_k^2} \left(1 - \frac{M_k^2}{m_{R,I}^2 - M_k^2} \ln \frac{m_{R,I}^2}{M_k^2} \right). \quad (4.8)$$

The neutrino mass can be written in matrix form

$$M_\nu = y^T \Lambda y \quad (4.9)$$

Here, we define the diagonal matrix Λ as

$$\Lambda = \text{diag}(\Lambda_1, \Lambda_2, \Lambda_3), \quad \Lambda_i = \frac{\lambda_5 v^2}{8\pi^2} \frac{M_k}{m_{R,I}^2 - M_k^2} \left(1 - \frac{M_k^2}{m_{R,I}^2 - M_k^2} \ln \frac{m_{R,I}^2}{M_k^2} \right). \quad (4.10)$$

The neutrino mass matrix M_ν can be diagonalized by the PMNS matrix U_{PMNS}

$$\hat{M}_\nu = \text{diag}(m_1, m_2, m_3) = U_{\text{PMNS}}^T M_\nu U_{\text{PMNS}}. \quad (4.11)$$

Here, m_i denotes the mass of the neutrino mass eigenstates. The equation above can be transformed to

$$\begin{aligned} 1 &= \sqrt{\hat{M}_\nu} U_{\text{PMNS}}^T y^T \Lambda y U_{\text{PMNS}} \sqrt{\hat{M}_\nu} \\ 1 &= \left(\Lambda^{1/2} y U_{\text{PMNS}} \hat{M}_\nu^{1/2} \right)^T \Lambda^{1/2} y U_{\text{PMNS}} \hat{M}_\nu^{1/2}. \end{aligned} \quad (4.12)$$

Thus, the matrix product $\Lambda^{1/2} y U_{\text{PMNS}} \hat{M}_\nu^{1/2}$ has to be an orthogonal matrix R and we can calculate the Yukawa couplings by

$$y = \sqrt{\Lambda}^{-1} R \sqrt{\hat{M}_\nu} U_{\text{PMNS}}^\dagger. \quad (4.13)$$

This is a modified version of the Casas-Ibarra parametrization [33] and will be useful for the numerical analysis of the parameter space of this model because this parametrization allows us to express the Yukawa couplings in terms of three free angles, which are the degrees of freedom of an orthogonal matrix.

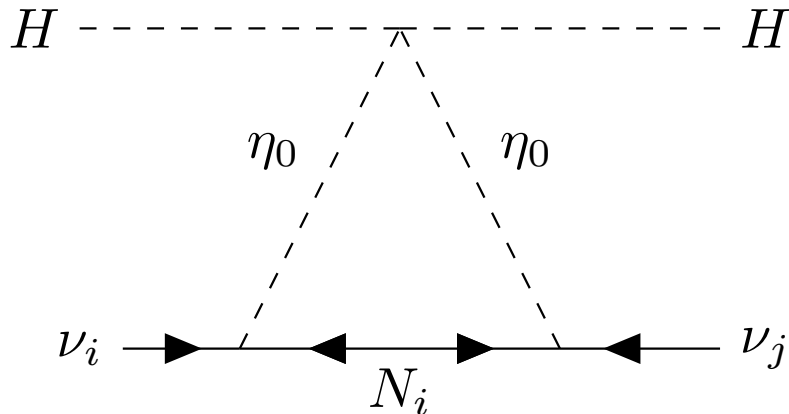


Figure 4.1: Neutrino mass generation in the scotogenic model

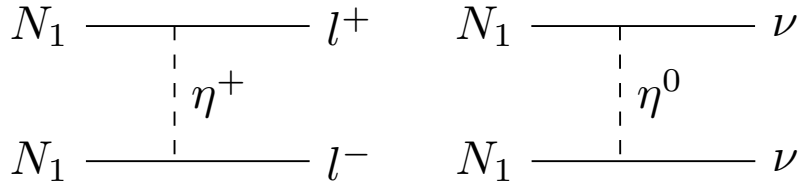


Figure 4.2: Annihilation channels for Fermionic Dark Matter in the scotogenic model

4.3 Dark matter

As mentioned above, the \mathbb{Z}_2 -symmetry of the scotogenic model ensures that the lightest odd particle is stable. Thus, it is a suitable Dark Matter candidate, if it is electrically neutral. Therefore, this model delivers scalar candidates $\eta_{R,I}$ and fermionic candidates N_i . Throughout this thesis, we will focus on the case in which the lightest right-handed neutrino N_1 is the Dark Matter particle. The annihilation channels of this particle are given in Figure 4.2. Hence, N_1 annihilates via t-channel diagrams. Regarding these annihilation channels, we can calculate the thermally averaged cross section using [[34], Appendix C]

$$\langle\sigma v\rangle = \sum_{\alpha,\beta} \frac{|y_{1\alpha}|^2 |y_{1\beta}|^2}{48\pi} \frac{m_{N_1}^2 (m_\eta^4 + m_{N_1}^4)}{(m_\eta^2 + m_{N_1}^2)^4} v^2. \quad (4.14)$$

Equation 2.9 shows that the cross section must be of order $\mathcal{O}(10^{-9})$ to satisfy the relic density. This cross section is velocity suppressed and in the freeze-out scenario, we can approximate $v^2 \approx \frac{6}{x_{fo}}$. In this thesis, we assume that the masses are in the range of 100 GeV up to 10 TeV. In this case, the Yukawa couplings have to be of the order $\mathcal{O}(1)$, which means that they are sizable. In addition to that, equation 4.14 shows that the Yukawa couplings have to become larger to satisfy the correct relic density if the masses become larger because the cross section is antiproportional to $m_{N/\eta}^2$.

4.4 Vacuum stability

We want to ensure that the vacuum in our model is stable. Therefore, the potential has to be bounded from below. Thus, the quartic couplings in the scalar potential have to satisfy some conditions. We derive these conditions using the ideas of [35]. This article states that a potential of the form $\lambda_{ab}\varphi_a^2\varphi_b^2$ is bounded from below if the matrix of the scalar couplings λ_{ab} is copositive. Copositivity is defined as follows: A symmetric matrix A is copositive if the quadratic form $x^T A x \geq 0$ is for all vectors $x \geq 0$. This means that if the matrix of the couplings λ_{ab} is copositive, the potential is always positive, because a vector given by

the parameters φ_a^2 is always bigger than 0. Thus, we have to bring the quartic terms of the potential from equation 4.2 into the following form

$$V_{ab} = \varphi_a^2 \lambda_{ab} \varphi_b^2. \quad (4.15)$$

Therefore, the field bilinears can be parametrized as $|H|^2 = h^2$, $|\eta|^2 = n^2$ and $H^\dagger \eta = hn\rho e^{i\phi}$ with the parameters $\rho \in [0, 1]$ and $\phi \in [0, 2\pi]$. Using this parameterization the quartic terms of the potential V_4 can be written as

$$V_4 = x^T \Lambda x, \text{ with } x = \begin{pmatrix} h^2 \\ n^2 \end{pmatrix} \quad (4.16)$$

with the matrix Λ

$$\Lambda = \frac{1}{2} \begin{pmatrix} \lambda_1 & \lambda_3 + \rho^2(\lambda_4 - |\lambda_5|) \\ \lambda_3 + \rho^2(\lambda_4 - |\lambda_5|) & \lambda_2 \end{pmatrix}. \quad (4.17)$$

If Λ is copositive, the potential is bounded from below. Thus, we have to minimize Λ and calculate the copositivity criteria to ensure that Λ is copositive for all values. The potential reaches its minimum for $\rho = 0$, if $\lambda_4 - |\lambda_5| \geq 0$ and if $\lambda_4 - |\lambda_5| \leq 0$, the potential reaches its minimum for $\rho = 1$. The copositivity criteria given in [35] lead to the following constraints for the quartic couplings

$$\begin{aligned} \lambda_1 &> 0 \\ \lambda_2 &> 0 \\ \lambda_3 &> -\sqrt{\lambda_1 \lambda_2} \\ \lambda_3 + \lambda_4 - |\lambda_5| &> -\sqrt{\lambda_1 \lambda_2}. \end{aligned} \quad (4.18)$$

4.5 Lepton flavor violation

The Standard Model has an accidental lepton flavor symmetry. This symmetry can be broken if the Standard Model is extended. This is the case in the Scotogenic Model. Here, lepton flavor violating processes are allowed at one-loop level. The diagrams for the decay of a lepton of flavor α into a lepton of flavor β and a photon are shown in Figure 4.3. Hence, we see that lepton flavor violating processes are possible due to the interaction of leptons with

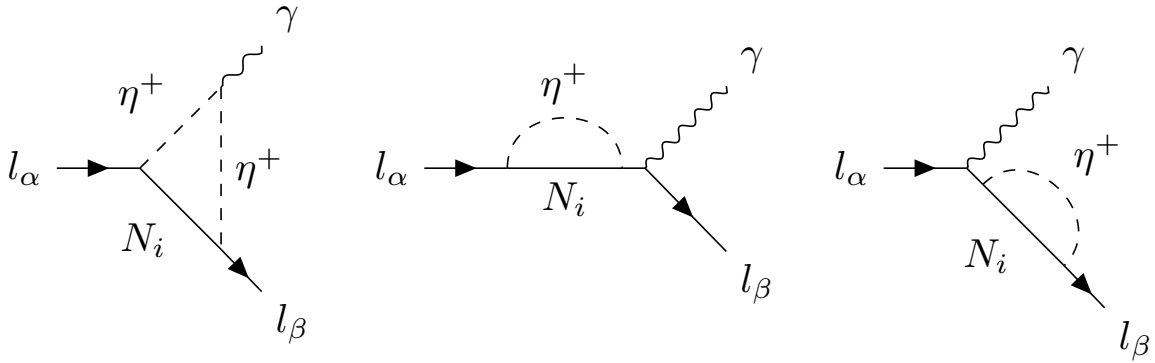


Figure 4.3: 1-loop Feynman diagrams leading to the lepton flavor violating process $l_\alpha \rightarrow l_\beta \gamma$

the right-handed fermions N_i and the charged part of the scalar doublet η^+ . The branching ratio of this process is given by

$$\text{BR}(l_\alpha \rightarrow l_\beta \gamma) = \frac{3\pi\alpha_{em}}{2G_F^2 m_\eta^2} |y_{i\beta}^* y_{i\alpha}|^2 F_2\left(\frac{m_{N_i}^2}{m_\eta^2}\right) \text{BR}(l_\alpha \rightarrow l_\beta \nu \bar{\nu}) \quad (4.19)$$

with the loop factor

$$F_2(t) = \frac{2t^3 + 3t^2 - 6t^2 \ln t - 6t + 1}{6(t-1)^4}. \quad (4.20)$$

This branching ratio is calculated in Appendix A using [36]. There are also decays of the form $l_\alpha \rightarrow 3l_\beta$ are also allowed and the diagrams are similar to those shown in Figure 4.3. The only difference is that the photon decays into $l_\beta \bar{l}_\beta$ and the photon can also be replaced by a Z-boson. In addition, there are box diagrams and Higgs-penguins contributing to this process. These are given in [37]. The term Higgs-penguin is used to denote loop diagrams, where a Higgs boson mediates flavor changing processes between fermions. There are experiment limits for the branching ratio of lepton flavor violating processes. These limits place stringent constraints on our model. The most stringent limit comes from the processes in which a muon decays into an electron. As shown in equation 4.19, these constraints affect the size of the Yukawa couplings and the masses of the new particles in the Scotogenic Model.

5 Numerical Analysis of the Scotogenic Model

This chapter contains a numerical analysis of the Scotogenic Model. Therefore, a parameter scan of this model is performed. In the first section of this chapter, the computer tools that are used for the scan are explained. After that, the constraints and the ranges for the scan are imposed. To perform the parameter scan, we use `emcee` [38] which is an implementation of a Monte-Carlo-Markov-Chain Ensemble sampler [39]. The use of `emcee` and the statistical treatment of the data is explained in Appendix B. After scanning the parameter space, we analyze the effects of the renormalization group equations (RGEs) on the viable points of the parameter space. Our analysis is based on [40], where the same analysis was performed for the Scotogenic Model and we try to confirm their results.

5.1 Tool chain

In the analysis of the model, different computer tools are used. These tools are connected to a tool chain which is shown in Figure 5.1. This tool chain can be divided into two parts. In the first part, the model is defined and implemented in the setup. In the second part, the numerical scan is performed.

The first step is to define the model and implement it in the tool chain. This can be done with the tool `SARAH`[41]. `SARAH` is a tool to analyze new models. It takes the definition of the new content of the model as input. These input files can be written by hand or generated by the program `MINIMAL-LAGRANGIANS`, which has been developed by Simon May [42]. After specifying the new particle content and the symmetries, `MINIMAL-LAGRANGIANS` is able to generate the most general Lagrangian for a model and the input files for `SARAH`. Thus, `SARAH` takes the new model content and the Lagrangian as input and is able to calculate analytical expressions for vertices, particle mass eigenstates up to one-loop level, mixing matrices and the renormalization group equations up to two-loop level. Furthermore, it uses these results to generate input for the next tools in our tool chain, `SPheno` and `micrOMEGAs`. The steps leading to the use of `SARAH` are the part of the tool chain, where the model is defined and implemented. Hence, these steps are performed only once.

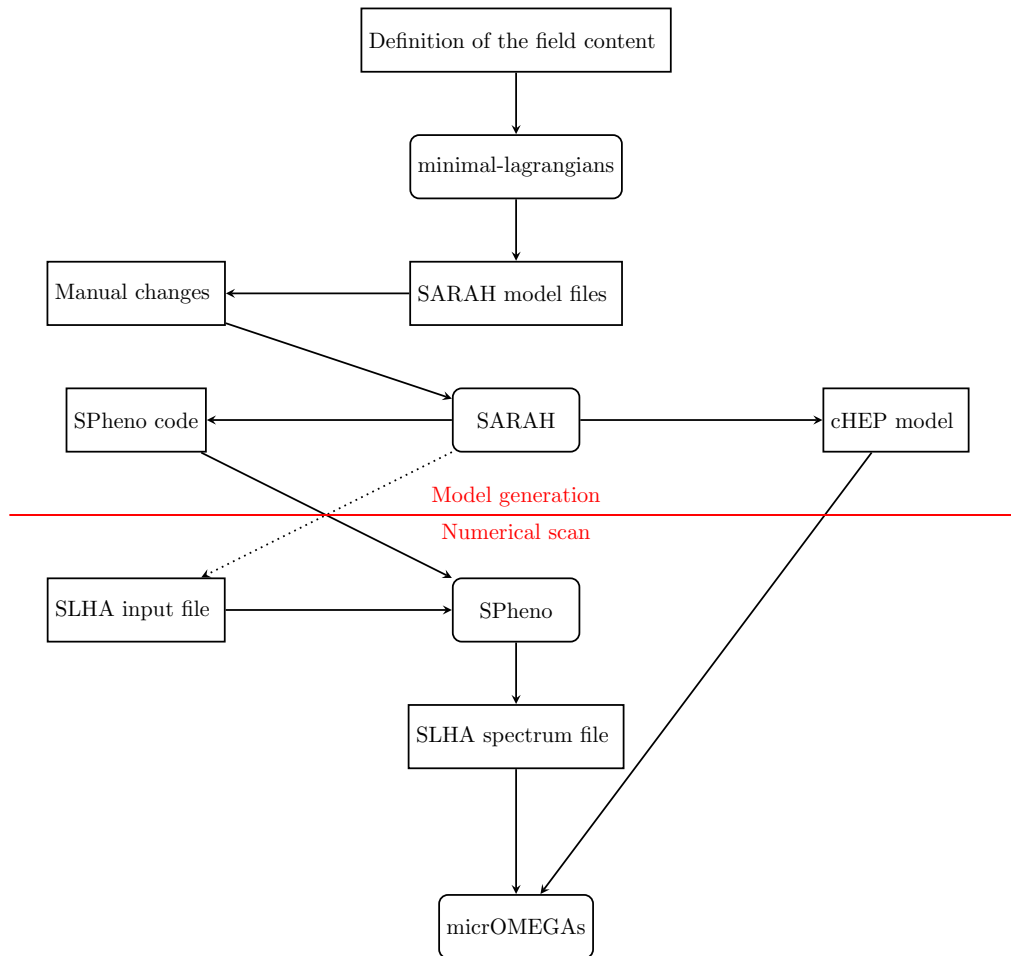


Figure 5.1: Tool chain used for the parameter scan, splitting up the process into the model generation and the numerical analysis.

The next step in the tool chain is performed by SPheno[43]. SPheno takes the model parameters as input and calculates the mass spectrum, particle decay modes, mixing matrices, contributions of BSM physics to the ρ -parameter and the branching ratio of lepton flavor violating processes. In addition to that, SPheno generates input for micrOMEGAs, the next tool in our tool chain. MicrOMEGAs [44] takes the output of SPheno and the model files generated by SARAH as input. It calculates the dark matter relic density and shows the contributing annihilation channels. These steps are performed several times to check if a proposed point satisfies the limits for lepton flavor violating processes and the constraint on the relic density.

5.2 Constraints

In this section, we want to specify the constraints that have to be satisfied by the points of the parameter space.

5.2.1 Theoretical constraints

To ensure that the vacuum is stable and the potential is bounded from below, the scalar couplings have to satisfy the constraints given in 4.18. In addition, we demand that the scalar couplings and the Yukawa couplings be perturbative to ensure that the tree-level and one-loop results can be trusted. So, we impose

$$|y_{ij}|^2, |\lambda_{2,3,4,5}| < 4\pi . \quad (5.1)$$

5.2.2 Experimental constraints

We require that our model satisfies some experimental limits. Therefore, we have to ensure that the points of our parameter space are in accordance with the experimental limits for the branching ratios of lepton flavor violating processes. Furthermore, the points must yield the correct relic density and the constraints from neutrino masses and mixing angles have to be satisfied. Notice that our experimental analysis is based on [40]. Thus, we use the same experimental limits that were used in this work.

To ensure that the constraints from neutrino masses and neutrino oscillation data are satisfied, we use a modified version of the Casas-Ibarra parametrization [33] given in equation 4.13. This allows us to calculate the Yukawa couplings in dependence on the neutrino data and 3 additional angles, which parametrize the orthogonal matrix. In our numerical scan, we use the neutrino data in the 3σ interval given in [45]. In our analysis, we focus on the normal hierarchy.

Lepton flavor violating processes usually set very stringent constraints on the model. Therefore, we make sure that the following experimental limits are satisfied

$$BR(\mu \rightarrow e\gamma) < 5.7 \cdot 10^{-13} [46] \quad (5.2)$$

$$BR(\mu \rightarrow 3e) < 1.0 \cdot 10^{-12} [47] \quad (5.3)$$

$$CR(\mu - e, Ti) < 4.3 \cdot 10^{-12} [48] \quad (5.4)$$

$$BR(\tau \rightarrow \mu\gamma) < 4.4 \cdot 10^{-8} [49] \quad (5.5)$$

$$BR(\tau \rightarrow e\gamma) < 4.4 \cdot 10^{-8} [49] . \quad (5.6)$$

In the numerical analysis, the branching ratios are calculated by SPheno [43].

As explained in the previous chapter, we consider the thermal freeze-out scenario with the lightest right-handed fermion N_1 as dark matter particle. Therefore, we have to ensure that N_1 is the lightest \mathbb{Z}_2 odd particle. In addition to that, we want to avoid coannihilations. To ensure this, it is requested that all other odd particles are at least 20% heavier than N_1 . We saw that N_1 annihilates into leptonic final states via t-channel and the relic density depends on the mass of N_1 , the mass of the scalar boson η and the Yukawa couplings. Hence, the relic density gives restrictions on all of these parameters. We require that every point yields a relic density of $\Omega h^2 \approx 0.12$. Here, we allow a deviation of 15% from this value.

5.3 The viable parameter space

Now we are able to perform the scan over the parameter space of the Scotogenic Model. The Scotogenic Model introduces 17 new parameters as follows: 3 fermion masses M_i , 5 parameters in the scalar sector, which are taken to be the scalar couplings $\lambda_{2,3,4,5}$ and the charged scalar mass M_{\pm} , and 9 new Yukawa couplings y_{ij} , which are taken as real parameters throughout our analysis. Using the Casas-Ibarra parametrization given in equation 4.13, we are able to express the 9 Yukawa couplings in terms of the neutrino data and an orthogonal matrix, which can be parametrized by 3 angles α_i . This allows us to reduce the number of free parameters from 17 to 11. We perform the parameter scan in the following ranges:

$$100 \text{ GeV} < M_i < 10 \text{ TeV}$$

$$100 \text{ GeV} < M_{\pm} < 10 \text{ TeV}$$

$$|\lambda_{2,3,4}| < 4\pi$$

$$10^{-12} < |\lambda_5| < 10^{-8}$$

$$0 < \alpha_i < 2\pi . \quad (5.7)$$

Notice that the masses and the scalar couplings are transferred on a logarithmic scale in order to scan them logarithmically.

The viable parameter space is shown in Figure 5.2. It is projected onto two different planes. In the left panel, it is projected onto the plane of dark matter mass versus the maximum magnitude of the Yukawa couplings y_{ij} and the right panel shows the plane of the dark matter mass versus the charged scalar mass.

First of all, it is observable that the dark matter mass never exceeds 5 TeV in our scan. The plot on the left shows that the largest Yukawa coupling is always sizable. This observation was expected because the Yukawa couplings have to be large enough to satisfy the correct relic density, as we explained in Section 4.3. We also see that the lower limit for the maximum size of the Yukawa couplings becomes smaller if the dark matter mass decreases. In the right panel of Figure 5.2 it is observable that the mass of the charged scalar increases if the dark matter mass increases. This is also expected because the charged scalar mass has to be larger than the dark matter mass. Otherwise, the dark matter particle would not be stable. However, we also see that the dark matter mass never exceeds values over 8 TeV.

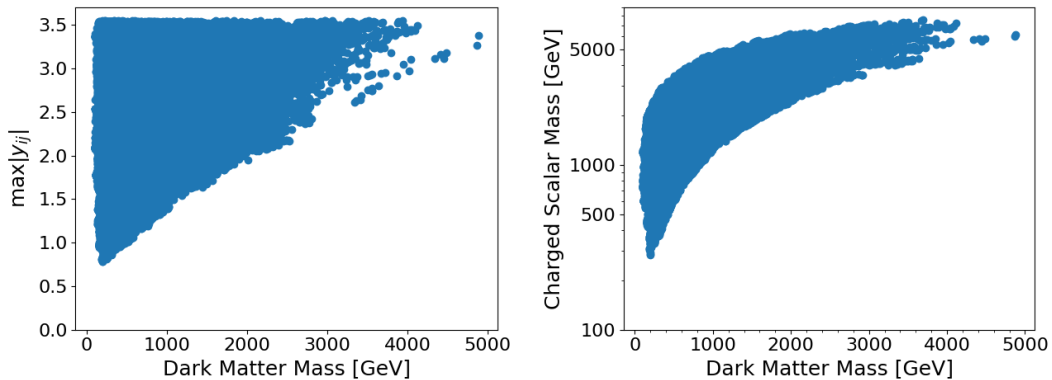


Figure 5.2: Our set of viable points projected onto two different planes. Left: Dark matter mass versus the largest Yukawa coupling y_{ij} . Right: Dark matter mass versus the charged scalar mass.

5.4 Analysis of the RGE effects

After scanning the parameter space, we want to analyze the effects of the renormalization group equations (RGEs) on the parameter space because the evolution of the RGEs might lead to a violation of the theoretical constraints at higher scales. The relevant RGEs for our analysis are given in Appendix C. These equations are derived by SARAH [41]. We follow the renormalization group evolution for each viable point from the weak scale up to a scale

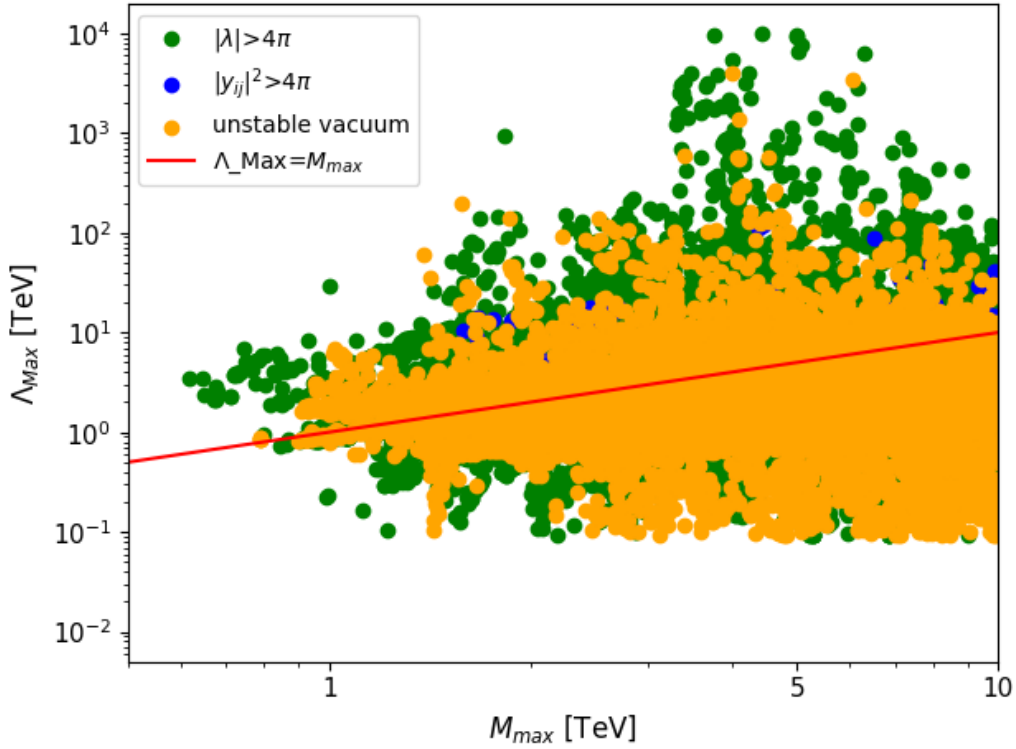


Figure 5.3: Scale of inconsistency Λ_{\max} as a function of the heaviest mass in the model. All models below the red line are inconsistent. The color coding shows the reason for the inconsistency.

Λ_{\max} , where one of the theoretical constraints is violated. Thus, either the vacuum becomes unstable or the couplings become non-perturbative at Λ_{\max} . The evolution of the RGEs is done by SciPy [50].

In Figure 5.3, we show Λ_{\max} for every point in dependence on the highest mass scale M_{\max} in the model. In addition to that, we also draw a red line in the plot, which stands for $\Lambda_{\max} = M_{\max}$. This red line marks the consistency limit because every point below the red line is inconsistent. The reason for this is that in these models the scale of inconsistency Λ_{\max} is lower than a mass scale intrinsic to the model. We find that only 10.61% of the points feature a Λ_{\max} larger than M_{\max} . So, almost 90% of the viable points are inconsistent. In Table 5.1, the amount of points that are consistent up to M_{\max} , $2M_{\max}$, $3M_{\max}$, $4M_{\max}$ and $5M_{\max}$ is given. There, we confirm that most points are not consistent up to high energy scales. Almost 99% of the points become inconsistent before reaching $5M_{\max}$.

Furthermore, we color-coded the points in Figure 5.3 to differentiate between the different reasons for the inconsistency. The points where the vacuum becomes unstable are drawn in orange and the points violating the perturbativity criterion are marked in green for the scalar couplings and in blue for the Yukawa couplings. In our analysis, we find that 61.09% of the

Consistency Scale	Fraction of the parameter space
M_{\max}	10.61%
$2M_{\max}$	2.92%
$3M_{\max}$	1.88%
$4M_{\max}$	1.39%
$5M_{\max}$	1.07%

Table 5.1: Fractions of the parameter space that are consistent up to certain energy scales.

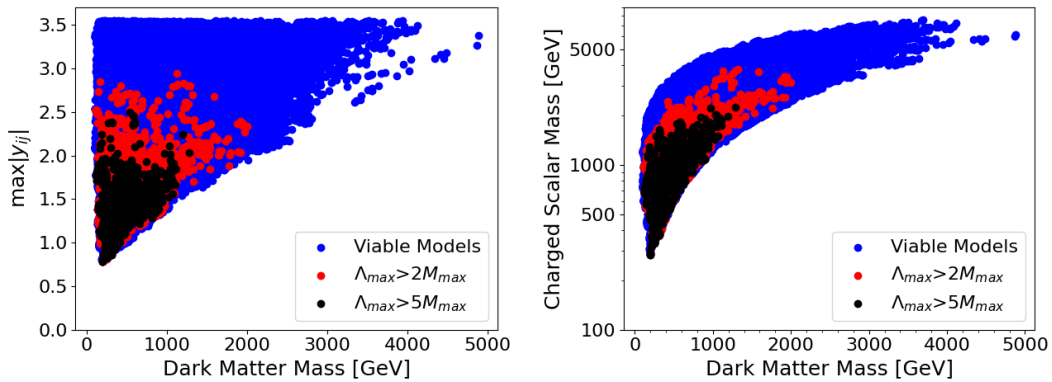


Figure 5.4: The modification of the parameter space once renormalization effects are taken into account. Requiring consistency of the model up to a scale $2M_{\max}$ ($5M_{\max}$) leaves only about 3% (1%) of the viable parameter space. Left: The dark matter mass versus the maximum value of the Yukawa coupling y_{ij} . Right: The dark matter mass versus the charged scalar mass.

points violate vacuum stability, for 37.81% the scalar couplings become non-perturbative and for 1.08% the Yukawa couplings become non-perturbative. Thus, the violation of vacuum stability appears to be the main reason for inconsistency. In Figure 5.3 it is observable that this condition tends to be violated at low scales. In addition to that, 94.37% of the points violate vacuum stability because λ_2 becomes negative.

We also investigated the regions of the parameter space, where the points remain consistent after taking RGE-effects into account. This is illustrated in Figure 5.2. There, the points that are consistent up to $2M_{\max}$ respectively $5M_{\max}$ are marked in red respectively black. We observe that the points consistent up to high scales are located in regions of the parameter space that feature small Yukawa couplings. This provides evidence that there is a dependence between the size of the Yukawa couplings and the scale of inconsistency. Our assumption is that there are terms in the RGEs that are dependent on the sizable Yukawa couplings and lead to inconsistencies. As mentioned above, the main reason for inconsistencies is the

violation of vacuum stability because λ_2 becomes negative. Regarding the RGE of λ_2 , we assume that the main driving force for this is the following term

$$\beta_{\lambda_2} \propto -4\text{Tr}(y^\dagger y y^\dagger y) . \quad (5.8)$$

If the Yukawa couplings become large, this term also increases. According to that, it drives λ_2 to negative values. In the case that this term is the dominant one in the RGEs, we are able to calculate an analytical estimate for Λ_{max} given by

$$\log\left(\frac{\Lambda_{\text{est}}}{\mu_o}\right) = -\frac{4\pi^2}{\text{Tr}(y^\dagger y y^\dagger y)} \Big|_{\mu=\mu_o} . \quad (5.9)$$

We calculate the estimate for every point that violates vacuum stability directly from low-energy data and compare the estimated scale with Λ_{max} . This is shown in Figure 5.5. In the left panel, the ratio $\Lambda_{\text{max}}/\Lambda_{\text{est}}$ versus the dark matter mass is shown. This plot shows that the ratio is almost 1 for most of the points. In addition to that, the normalized density for the ratio $\Lambda_{\text{max}}/\Lambda_{\text{est}}$ is illustrated in the right panel of Figure 5.5. This distribution has a peak at $\frac{\Lambda_{\text{max}}}{\Lambda_{\text{est}}} = 1$. Hence, we can conclude that our analytical estimate is a good estimate for Λ_{max} if the vacuum stability is violated. This confirms that the term $-4\text{Tr}(y^\dagger y y^\dagger y)$ is the main driving force in the RGEs. Thus, the violation of vacuum stability is closely related to the size of the Yukawa couplings. As a consequence, we get stringent constraints on our parameter space if we request consistency up to high scales because the picture of the parameter space (Fig. 5.2) shows that large parts of the viable parameter space feature large Yukawa couplings. As mentioned before, this size of the Yukawa couplings is required to obtain the correct relic density. Therefore, this constraint restricts big parts of the parameter space.

This result is also the main result of [40]. Hence, we can confirm their discovery that the violation of vacuum stability is an intrinsic feature of the Scotogenic Model with fermionic WIMP dark matter. To avoid the violation of the vacuum stability constraints, one has to find a way to decrease the size of the Yukawa couplings and still satisfy the constraint arising from the relic density. In [40], some approaches to achieve this are mentioned. One approach could be to consider coannihilations between the singlet fermions and the scalar particles to obtain the relic density. As shown in [51], this would lead to smaller Yukawa couplings. It would also be possible to consider scalar dark matter instead of fermionic dark matter because the relic density of scalar dark matter is mostly determined by gauge interactions. In this case, the Yukawa couplings can be taken to be small. Another approach is to consider the freeze-in scenario [52] instead of the freeze-out. This scenario has been studied for the Scotogenic Model in [53]. In the case that the lightest singlet fermion is the dark matter particle, the

Yukawa couplings associated with this particle have to be tiny to prevent thermalization in the early universe. The remaining Yukawa couplings can naturally be small to explain the tiny neutrino masses.

The points that violate the perturbativity criterion for the scalar couplings make 37.81% of

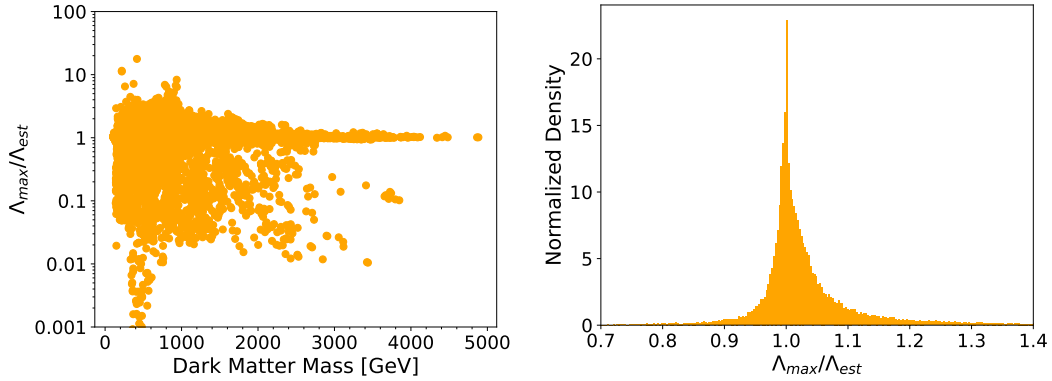


Figure 5.5: Ratio of estimated and numerically determined scale of inconsistency for viable points that violate the vacuum stability condition. Left: Ratio of the two scales versus the dark matter mass. Right: Distribution of the ratio of the scales.

the total number of points. This is also a large part of the parameter space. In [40], they claim that these points tend to feature large scalar couplings. Thus, we compare the size of the scalar couplings of the perturbativity violating points to all viable points. In order to do that, we determine the largest scalar coupling $|\lambda_{\max}| = |\max(\lambda_2, \lambda_3, \lambda_4, \lambda_5)|$ for every point. In Figure 5.6, we illustrate the normalized density of the largest scalar coupling for all viable points in the left panel and for the points that violate the perturbativity condition in the right panel. Comparing these two distributions, we observe that the points violating the perturbativity criterion feature larger scalar couplings compared to all viable points. Hence, we assume that in this case the scalar couplings dominate the RGEs and drive themselves to non-perturbative magnitudes. The main driving force in the RGEs is most likely a term with the following structure

$$\beta_\lambda = b\lambda^2, \quad (5.10)$$

where b is a coefficient depending on the scalar coupling. However, the phenomenology of the model does not require large values for the scalar couplings. This is why it should be possible to set lower limits on the scalar couplings without modifying the rest of the parameter space. In this case, most of the points that violate the perturbativity criterion could be eliminated. This was also checked in [40]. Thus, the main restriction of the parameter space arises from the violation of vacuum stability due to the sizable Yukawa couplings.

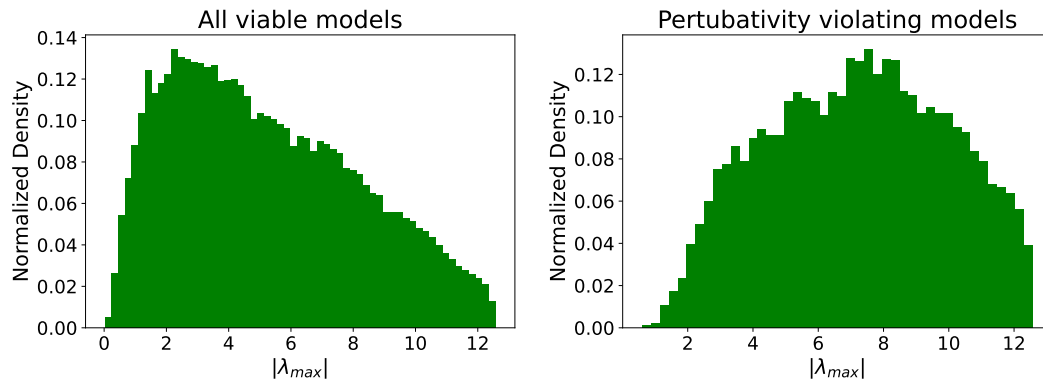


Figure 5.6: Normalized density for the largest scalar coupling $|\lambda_{max}|$ for all viable point (left) and the points that violate the perturbativity criterion (right).

6 KNT-Model

The KNT-Model, proposed by Lawrence M. Krauss, Salah Nasri and Mark Trodden in 2002[7], extends the Standard Model with the aim to introduce neutrino masses. In this model, the left-handed neutrinos obtain their masses from a three-loop radiative seesaw mechanism. Furthermore, the model delivers a fermionic dark matter candidate.

6.1 Particle content

The KNT-Model extends the Standard Model by two singlet charged scalars S_1 and S_2 and three generations of right-handed fermions N_i . In addition, a \mathbb{Z}_2 symmetry is introduced, under which all Standard Model fields and S_1 are even and S_2 and the right-handed fermions are odd. This symmetry ensures that Dirac mass terms are forbidden. Additionally, this symmetry stabilizes the lightest odd particle. Thus, the lightest odd particle can be a dark matter candidate if it is neutral. Therefore, only the new fermions N_i are suitable dark matter candidates because S_2 is charged. The particle content of this model is given in Table 6.1 The Lagrangian of the Standard Model is extended as follows:

$$\mathcal{L} = \mathcal{L}_{SM} + \tilde{Y}_{ij} L_i^T C i \tau_2 L_j S_1^\dagger + Y_{ij} N_i S_2^\dagger l_{jR} + M_i N_i^T C N_i + h.c. + V(H, S_1, S_2) . \quad (6.1)$$

Here, L_i is the SU(2)-doublet for the i th lepton generation and l_{jR} denotes the right-handed lepton singlet for the j th generation. The Yukawa couplings \tilde{Y}_{ij} are antisymmetric. $V(H, S_1, S_2)$ is the scalar potential, which is given by

$$\begin{aligned} V(H, S_1, S_2) = & -M_H^2 |H|^2 + M_{S_1}^2 |S_1|^2 + M_{S_2}^2 |S_2|^2 + \frac{\lambda_H}{2} |H|^4 + \frac{\lambda_{S_1}}{2} |S_1|^4 + \frac{\lambda_{S_2}}{2} |S_2|^4 \\ & + \lambda_{HS_1} |H|^2 |S_1|^2 + \lambda_{HS_2} |H|^2 |S_2|^2 + \lambda_{S_1 S_2} |S_1|^2 |S_2|^2 + \frac{1}{2} (\lambda'_{S_1 S_2} (S_1 S_2^*)^2 + h.c.) . \end{aligned} \quad (6.2)$$

The \mathbb{Z}_2 symmetry is considered unbroken in this model as well as in the Scotogenic Model. This ensures that the lightest odd particle remains stable. After electroweak symmetry breaking the masses of the scalar particles are given by

$$\begin{aligned} m_H^2 &= \lambda_H v^2 \\ m_{S_1}^2 &= M_{S_1}^2 + \frac{1}{2} \lambda_{HS_1} v^2 \\ m_{S_2}^2 &= M_{S_2}^2 + \frac{1}{2} \lambda_{HS_2} v^2 . \end{aligned} \quad (6.3)$$

Here, $v = 246.22$ GeV is the vacuum expectation value of the Standard Model Higgs.

Field	Generations	Spin	$U(1)_Y \times SU(2)_L \times SU(3)_c$	Z_2
N_i	3	$\frac{1}{2}$	(0,1,1)	-1
S_1	1	0	(1,1,1)	+1
S_2	1	0	(1,1,1)	-1
SM particles	-	-	-	+1

Table 6.1: Particle content of the KNT Model.

6.2 Neutrino mass

In this model, neutrino masses are generated by a three-loop diagram, which is shown in figure 6.1. The calculation of the neutrino mass matrix is given in [54], and the neutrino mass matrix is given by

$$(M_\nu)_{\alpha\beta} = \frac{\lambda'_{S_1 S_2} m_{l_i} m_{l_k}}{(4\pi^2)^3 m_{S_1}} \tilde{Y}_{\alpha i} \tilde{Y}_{\beta k} Y_{ij} Y_{kj} F\left(\frac{M_j^2}{m_{S_2}^2}, \frac{m_{S_1}^2}{m_{S_2}^2}\right). \quad (6.4)$$

In this case m_{l_i} denotes the lepton masses with the flavor indices $i = (e, \mu, \tau)$ and $F(x, y)$ is a loop function given by

$$F(x, y) = \frac{\sqrt{x}}{8y^{\frac{3}{2}}} \int_0^\infty dr \frac{r}{r+x} \left(\int_0^1 dx \ln \frac{x(1-x)r + (1-x)y + x}{x(1-x)r + x} \right)^2. \quad (6.5)$$

Due to the antisymmetry of \tilde{Y} , its determinant is $\det(\tilde{Y}) = 0$. Therefore, equation 6.4 implies that the determinant of M_ν is also $\det(M_\nu) = 0$. This means that one of the eigenvalues of M_ν has to be 0. According to that, we can set one of the three neutrino masses to 0.

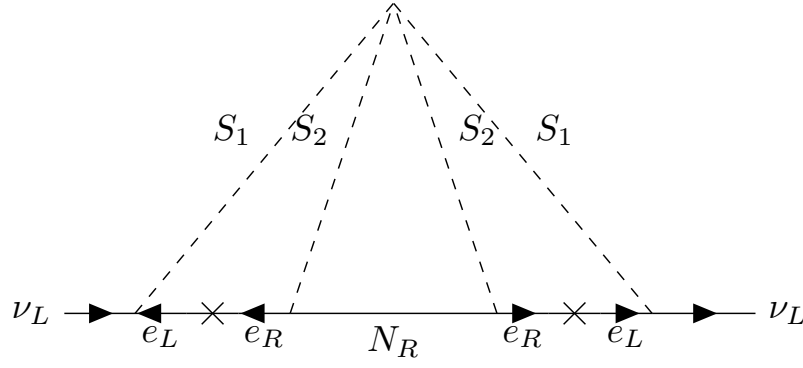


Figure 6.1: Neutrino mass generation in the KNT model.

6.3 Parametrization of the Yukawa couplings

In the Scotogenic Model, we could parametrize the Yukawa couplings with a modified version of the Casas-Ibarra parametrization, which is given in equation 4.13. Now we want to derive a similar parametrization for the Yukawa couplings in the KNT-Model. This is done in this section. Our parameterization for the Yukawa couplings is inspired by [55].

First of all, the neutrino mass matrix given in 6.4 can be written as

$$M_\nu = c\tilde{Y}M_eY(M_{\text{eff}})^{-1}Y^TM_e\tilde{Y}^T \quad (6.6)$$

with the prefactor $c = \frac{\lambda'_{S_1 S_2}}{(4\pi^2)^3 m_{S_1}}$, the lepton mass matrix $M_e = \text{diag}(m_e, m_\mu, m_\tau)$ and the diagonal matrix

$$(M_{\text{eff}})^{-1} = \text{diag}(F_1, F_2, F_3) \text{ with } F_i = F\left(\frac{M_i^2}{m_{S_2}^2}, \frac{m_{S_1}^2}{m_{S_2}^2}\right). \quad (6.7)$$

Due to the antisymmetry of \tilde{Y} , the neutrino mass matrix can also be written as

$$M_\nu = -c\tilde{Y}M_eY(M_{\text{eff}})^{-1}Y^TM_e\tilde{Y}. \quad (6.8)$$

First, we want to derive a parametrization for \tilde{Y} . Therefore, we can use the antisymmetry of \tilde{Y} because this implies that one eigenvalue of \tilde{Y} is zero and the corresponding eigenvector a is given by

$$a = (\tilde{Y}_{23}, -\tilde{Y}_{13}, \tilde{Y}_{12}). \quad (6.9)$$

Regarding equation 6.8, we see that a also has to be an eigenvector of M_ν with the corresponding eigenvalue 0. In addition, we can diagonalize M_ν using the PMNS-Matrix

$$M_\nu = U_{\text{PMNS}}^* \hat{M}_\nu U_{\text{PMNS}}^\dagger . \quad (6.10)$$

This leads to the following equation

$$\hat{M}_\nu U_{\text{PMNS}}^\dagger a = 0 . \quad (6.11)$$

Since one neutrino mass is 0, one equation of the system is trivial. The other two equations can be used to calculate two of the three entries of \tilde{Y} in dependence on the third. In this thesis, we choose \tilde{Y}_{23} as the free parameter. The expressions of the other two parameters depend on the hierarchy. For NH, they are given by

$$\begin{aligned} \frac{(\tilde{Y})_{13}}{(\tilde{Y})_{23}} &= \frac{c_{23}s_{12}}{c_{12}c_{13}} + e^{-i\delta_{CP}} \frac{s_{23}s_{13}}{c_{13}} \\ \frac{(\tilde{Y})_{12}}{(\tilde{Y})_{23}} &= \frac{s_{23}s_{12}}{c_{12}c_{13}} + e^{-i\delta_{CP}} \frac{c_{23}s_{13}}{c_{13}} . \end{aligned} \quad (6.12)$$

For IH, they are given by

$$\begin{aligned} \frac{(\tilde{Y})_{13}}{(\tilde{Y})_{23}} &= e^{i\delta_{CP}} \frac{c_{23}c_{13}}{s_{13}} \\ \frac{(\tilde{Y})_{12}}{(\tilde{Y})_{23}} &= -e^{i\delta_{CP}} \frac{s_{23}c_{13}}{s_{13}} . \end{aligned} \quad (6.13)$$

In the next step, we want to derive a parameterization for the other Yukawa coupling Y as well. Therefore, we write the neutrino mass matrix in the form

$$M_\nu = -c\tilde{Y}M_{\text{aux}}\tilde{Y} . \quad (6.14)$$

Here, we define an auxiliary matrix

$$M_{\text{aux}} = M_e Y (M_{\text{eff}})^{-1} Y^T M_e . \quad (6.15)$$

This auxiliary matrix M_{aux} is symmetric. Thus, it has six independent parameters. Equation 6.14 defines a set of six equations that relate the entries of M_{aux} to neutrino data, but three of these equations are trivial because of the one neutrino mass which is set to 0. The remaining three equations can be used to express three entries of M_{aux} in dependence on the other Yukawa couplings \tilde{Y}_{ij} , neutrino data and the three remaining entries of M_{aux} . We will not

show how to solve the equations in detail because they are very long. We use Wolfram Mathematica [56] to solve the equations. Notice that it does not matter which entries of M_{aux} are chosen as free variables because it is possible to bring this system of equations into a Gaussian form. If this is the case, every possible choice of free variables will parametrize the same solution space, which is shown in [[57], Chapter 1].

After solving the equations, Y can be calculated by

$$Y = M_e^{-1} U_{\text{aux}}^* \hat{M}_{\text{aux}}^{-\frac{1}{2}} R (M_{\text{eff}})^{\frac{1}{2}} . \quad (6.16)$$

Here, \hat{M}_{aux} is the diagonalized auxiliary matrix, U_{aux} is the transformation matrix that diagonalizes M_{aux} , and R is an orthogonal matrix.

6.4 Dark matter

As mentioned above, the \mathbb{Z}_2 symmetry ensures the stability of the lightest odd particle. This particle can be a dark matter candidate if it is electrically neutral. In this model, there is no scalar candidate because the odd scalar particle S_2 is charged. Therefore, the only possible candidates are the three right-handed fermions N_i . In our analysis we regard N_1 as dark matter candidate and consider the freeze-out scenario. The contributing annihilation channel is shown in figure 6.2. Thus, the annihilation channel is a t-channel diagram and we can use [[34], Appendix C] to approximate the thermally averaged cross section for this annihilation

$$\langle \sigma v \rangle = \sum_{\alpha, \beta} \frac{|Y_{1\alpha}|^2 |Y_{1\beta}|^2 m_{N_1}^2 (m_{S_2}^4 + m_{N_1}^4)}{48\pi (m_{S_2}^2 + m_{N_1}^2)^4} v^2 . \quad (6.17)$$

Here, we can observe that this cross section is similar to the cross section in the Scotogenic Model given in equation 4.14. We also assume that the masses of the new particles are in the range of 100 GeV up to 10 TeV. Therefore, we are able to argue that the Yukawa couplings have to be of order $\mathcal{O}(1)$ to obtain the correct relic density as in the Scotogenic Model.

6.5 Vacuum stability

We also have to ensure that the vacuum is stable and the potential is bounded from below in the KNT-Model. Therefore, the scalar couplings have to satisfy some constraints. We want to derive these constraints by performing the same process as we did for the Scotogenic

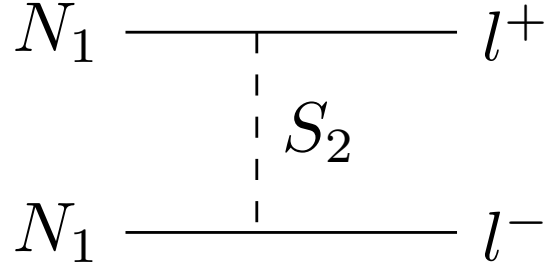


Figure 6.2: Annihilation channel for Fermionic Dark Matter in the KNT-Model.

Model by using the copositivity criteria. This is explained in [35]. The quartic terms of the potential are given by

$$\begin{aligned}
 V_4 = & \frac{\lambda_h}{2}|H|^4 + \frac{\lambda_{S_1}}{2}|S_1|^4 + \frac{\lambda_{S_2}}{2}|S_2|^4 + \lambda_{hS_1}|H|^2|S_1|^2 + \lambda_{hS_2}|H|^2|S_2|^2 \\
 & + \lambda_{S_1S_2}|S_1|^2|S_2|^2 + \frac{1}{2}(\lambda_s(S_1S_2^*)^2 + h.c.) .
 \end{aligned} \tag{6.18}$$

First, we have to bring V_4 into the special form given in equation 4.15. Therefore, we parametrize the field bilinears with

$$|H|^2 = h^2, |S_1|^2 = s_1^2, |S_2|^2 = s_2^2, (S_1S_2^*)^2 = s_1^2s_2^2e^{i\delta} . \tag{6.19}$$

Using this parametrization, the quartic potential can be written as

$$V_4 = x^T \Lambda x, \text{ with } x = \begin{pmatrix} h^2 \\ s_1^2 \\ s_2^2 \end{pmatrix} \tag{6.20}$$

and with the matrix Λ

$$\Lambda = \frac{1}{2} \begin{pmatrix} \lambda_h & \lambda_{hS_1} & \lambda_{hS_2} \\ \lambda_{hS_1} & \lambda_{S_1} & \lambda_{S_1S_2} - |\lambda_s| \cos \delta \\ \lambda_{hS_2} & \lambda_{S_1S_2} - |\lambda_s| \cos \delta & \lambda_{S_2} \end{pmatrix} . \tag{6.21}$$

This potential reaches its minimum for $\delta = \pi$. The matrix Λ has to be copositive to ensure vacuum stability. Applying the copositivity criteria given in [35] to this matrix leads to the following conditions for the scalar couplings

$$\begin{aligned}
& \lambda_h, \lambda_{S_1}, \lambda_{S_2} > 0 \\
& \lambda_{hS_1} + \sqrt{\lambda_h \lambda_{S_1}} > 0 \\
& \lambda_{hS_2} + \sqrt{\lambda_h \lambda_{S_2}} > 0 \\
& \lambda_{S_1 S_2} - |\lambda_s| + \sqrt{\lambda_{S_1} \lambda_{S_2}} > 0 \\
& \frac{\sqrt{\lambda_h \lambda_{S_1} \lambda_{S_2}} + \lambda_{hS_1} \sqrt{\lambda_{S_2}} + \lambda_{hS_2} \sqrt{\lambda_{S_1}} + (\lambda_{S_1 S_1} - |\lambda_s|) \sqrt{\lambda_h}}{\sqrt{2(\lambda_{hS_1} + \sqrt{\lambda_h \lambda_{S_1}})(\lambda_{hS_2} + \sqrt{\lambda_h \lambda_{S_2}})(\lambda_{S_1 S_2} - |\lambda_s| + \sqrt{\lambda_{S_1} \lambda_{S_2}})}} > 0. \tag{6.22}
\end{aligned}$$

6.6 Lepton flavor violation

In the KNT-Model, lepton flavor violating processes are also allowed at one-loop level as in the Scotogenic Model. Here, these processes are possible due to interactions of the charged leptons with the scalar boson S_1 and left-handed neutrinos, as well as interactions with the scalar boson S_2 and right-handed fermions N_i . The Feynman diagrams for the decay $l_\alpha \rightarrow l_\beta \gamma$ for the interaction with S_1 , and the left-handed neutrinos are shown in Figure 6.3 and for the interaction with S_2 and N_i , the Feynman diagrams are shown in Figure 6.3. The branching ratio for this process is calculated in Appendix A following [36]

$$\begin{aligned}
\text{BR}(l_\alpha \rightarrow l_\beta \gamma) &= \text{BR}_1(l_\alpha \rightarrow l_\beta \gamma) + \text{BR}_2(l_\alpha \rightarrow l_\beta \gamma) \\
&= \frac{\pi \alpha_{em}}{G_F^2} \left(\frac{|\tilde{Y}_{\beta i}^* \tilde{Y}_{\alpha i}|^2}{4m_{S_1}^2} + \frac{3|Y_{i\beta}^* Y_{i\alpha}|^2}{2m_{S_2}^2} \right) \text{BR}(l_\alpha \rightarrow l_\beta \nu \bar{\nu}) \tag{6.23}
\end{aligned}$$

with the loop factor

$$F_2(t) = \frac{2t^3 + 3t^2 - 6t^2 \ln t - 6t + 1}{6(t-1)^4}. \tag{6.24}$$

As in the Scotogenic Model, the decay $l_\alpha \rightarrow 3l_\beta$ is also possible. The contributing diagrams are similar to those shown in Figures 6.3 and 6.4. The only difference is that the photon decays into $l_\beta \bar{l}_\beta$ and the photon can also be replaced by a Z-boson. In addition, there are also box diagrams and Z-penguins contributing to this process, as shown in [58]. The experimental limits on the branching ratios of the lepton flavor violating processes set stringent constraints on the model, particularly the processes in which a muon decays into an electron.

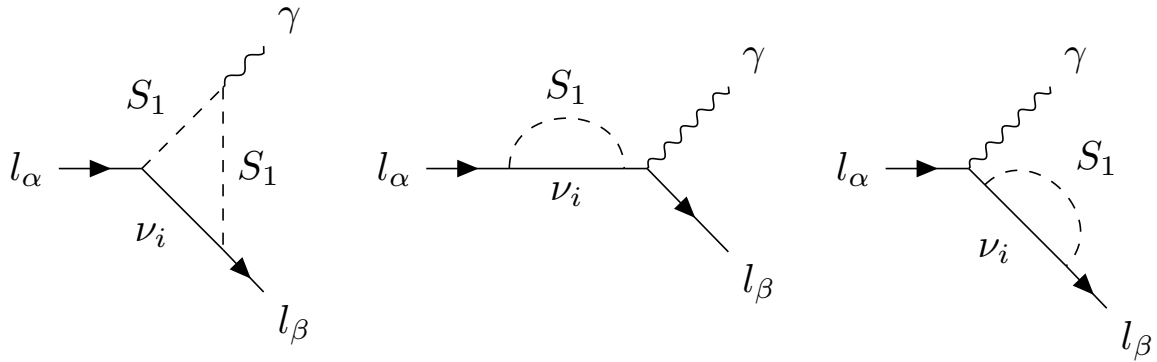


Figure 6.3: 1-loop Feynman diagrams leading to the lepton flavor violating process $l_\alpha \rightarrow l_\beta \gamma$ due to interactions with S_1 and the left-handed neutrinos.

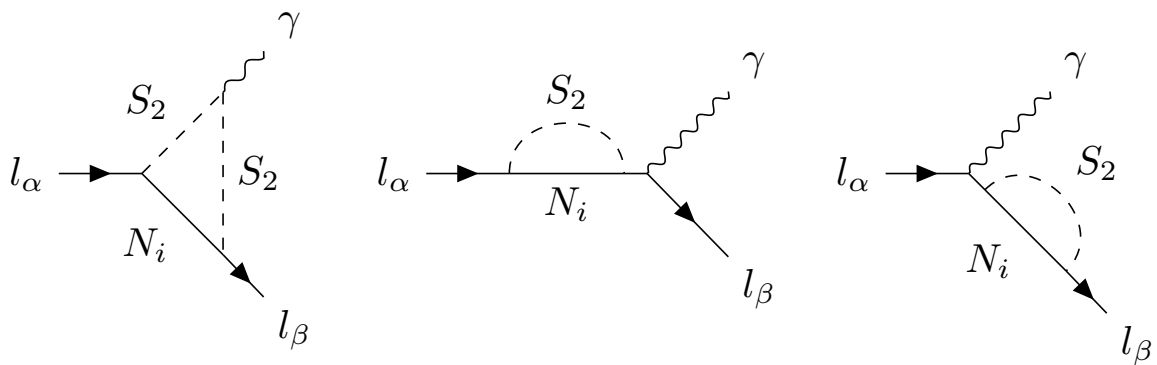


Figure 6.4: 1-loop Feynman diagrams leading to the lepton flavor violating process $l_\alpha \rightarrow l_\beta \gamma$ due to interactions with S_2 and the right-handed fermions N_i .

7 Numerical Analysis of the KNT-Model

In this chapter, we deal with the numerical analysis of the KNT-Model. Therefore, we use the tool chain explained in Chapter 5.1 for the implementation and numerical analysis of the model. To perform the parameter scan, we use emcee [38] which is an implementation of a Monte-Carlo-Markov-Chain Ensemble sampler [39]. The use of emcee and the statistical treatment of the data is explained in Appendix B.

7.1 Constraints

7.1.1 Theoretical Constraints

To ensure that the potential of the model is bounded from below and the vacuum is stable, some constraints for the scalar couplings are required. These constraints are derived in Chapter 6.5 and are given in equation 6.22. Furthermore, the scalar coupling and the Yukawa couplings have to be perturbative to ensure that tree-level and one-loop results can be trusted. Therefore, the following perturbativity limits are imposed

$$|\tilde{Y}_{ij}|^2, |Y_{ij}|^2, |\lambda_{S_1}|, |\lambda_{S_2}|, |\lambda_{HS_1}|, |\lambda_{HS_2}|, |\lambda_{S_1 S_2}|, |\lambda'_{S_1 S_2}| < 4\pi . \quad (7.1)$$

7.1.2 Experimental Constraints

To ensure that our model satisfies the constraints from neutrino masses and mixing angles, we use the parametrization explained in chapter 6.3. This parametrization allows us to calculate the Yukawa couplings in dependence on the neutrino data. The formula for this is given in equation 6.16. The mixing angles and the mass differences are given in Table 3.3 which is taken from [30].

Experimental limits on lepton flavor violating processes also impose stringent constraints on

the model. In our analysis, we calculate the branching ratios for these processes with SPheno [43]. We impose the current experimental limits

$$\begin{aligned}
BR(\mu \rightarrow e\gamma) &< 3.1 \cdot 10^{-13} \text{ [59]} \\
BR(\mu \rightarrow 3e) &< 1.0 \cdot 10^{-12} \text{ [47]} \\
CR(\mu - e, Ti) &< 4.3 \cdot 10^{-12} \text{ [48]} \\
BR(\tau \rightarrow \mu\gamma) &< 4.2 \cdot 10^{-8} \text{ [60]} \\
BR(\tau \rightarrow e\gamma) &< 3.3 \cdot 10^{-8} \text{ [49] .}
\end{aligned} \tag{7.2}$$

Our viable points also have to yield the correct relic density of $\Omega h^2 \approx 0.12$. As in the Scotogenic Model, we allow a deviation of 15%. In Chapter 6.4, we explained that we consider the freeze-out mechanism with N_1 as dark matter particle. Furthermore, we do not consider coannihilation channels. Thus, we have to ensure that N_1 is lighter than the other \mathbb{Z}_2 odd particles. To ensure this, we request that all other odd particles are at least 20% heavier than N_1 .

7.2 Ranges of the parameters

The KNT-Model introduces 23 new parameters which are given in Table 7.1. Here, we can use the parametrization explained in Chapter 6.3. This parametrization allows us to eliminate some of the parameters. Only one entry of the antisymmetric Yukawa couplings \tilde{Y}_{ij} can be freely chosen and the other two depend on this free parameter and neutrino data. We choose \tilde{Y}_{23} as the free parameter. The other Yukawa couplings Y_{ij} can be calculated in terms of an orthogonal matrix and a symmetric auxiliary M_{aux} matrix, which is shown in equation 6.16. We find that only three entries of M_{aux} are and the other three depend on the free ones and the neutrino data. In this thesis, we choose M_{11}, M_{12}, M_{13} as the free parameters. Thus, \tilde{Y} has just one free parameter and Y has six, three angles parametrizing the orthogonal matrix and three free parameters of M_{aux} . Now we have to define the ranges for the parameters. For the couplings, it is very easy, since they have to satisfy the perturbativity limits; for the angles, we can choose the range $0 - 2\pi$ and the masses are usually in the range 100 GeV up to 10 TeV, which is the required mass scale for WIMPs. To choose the limits for the entries of M_{aux} , we regard its structure

$$M_{\text{aux}} = M_e Y (M_{\text{eff}})^{-1} Y^T M_e \tag{7.3}$$

with the effective matrix

$$(M_{\text{eff}})^{-1} = \text{diag}(F_1, F_2, F_3) \text{ with } F_i = F\left(\frac{M_i^2}{m_{S_2}^2}, \frac{m_{S_1}^2}{m_{S_2}^2}\right). \quad (7.4)$$

Here, $F(x, y)$ is the loop function given in equation 6.5. This loop function has a limit of $F(x, y) < 1.05$, which is shown in [61]. Furthermore, the Yukawa couplings Y_{ij} must satisfy the perturbativity limit $|Y_{ij}|^2 < 4\pi$. Hence, we can set a limit on the entries of M_{aux}

$$M_{\text{aux}_{ij}} < 3 \cdot 1.05 \cdot 4\pi \cdot m_{l_i} m_{l_j}. \quad (7.5)$$

Here, m_{l_i} stands for the lepton masses. The parameter scan is performed in the following ranges

$$100 \text{ GeV} < M_i, M_{S_1}, M_{S_2} < 10 \text{ TeV} \quad (7.6)$$

$$|\lambda_{S_1}, \lambda_{S_2}, \lambda_{HS_1}, \lambda_{HS_2}, \lambda_{S_1 S_2}, \lambda'_{S_1 S_2}| < 4\pi \quad (7.7)$$

$$0 < \alpha_i < 2\pi \quad (7.8)$$

$$|\tilde{Y}_{23}|^2 < 4\pi \quad (7.9)$$

$$|(M_{\text{aux}})_{ij}| < m_i m_j \cdot (3 \cdot 1.05 \cdot 4\pi). \quad (7.10)$$

In our numerical analysis, we scan the masses, the scalar couplings, the Yukawa coupling \tilde{Y}_{23} and the entries of M_{aux} on a logarithmic scale. The scan is performed for both hierarchies. In addition to that, we also perform a scan for the normal hierarchy, where we scan the scalar couplings on a linear scale. In this case, the scalar couplings should become larger. In our analysis for the Scotogenic Model, we found that large scalar couplings could lead to a violation of the perturbativity criterion at higher scales. In addition to that, we assumed that it should be possible to reduce the size of the scalar couplings without modifying the rest of the parameter space because the phenomenology does not require them to be large. This is why we want to investigate whether larger scalar couplings affect the parameter space and the evolution of the renormalization group equations in the KNT-Model.

Sort of parameters	Parameters
3 fermion masses	$M_{N_1}, M_{N_2}, M_{N_3}$
2 scalar masses	M_{S_1}, M_{S_2}
6 scalar couplings	$\lambda_{S_1}, \lambda_{S_2}, \lambda_{HS_1}, \lambda_{HS_2}, \lambda_{S_1 S_2}, \lambda'_{S_1 S_2}$
3 complex entries of the Yukawa matrix \tilde{Y}	\tilde{Y}_{ij}
9 complex entries of the Yukawa Matrix Y	Y_{ij}

Table 7.1: New parameters in the KNT-Model.

7.3 Viable Parameter Space

After defining the limits, the parameter scan is performed. In Figure 7.1, the parameter space is illustrated for NH (left) and IH (right). There, it is projected on the plane of dark matter mass versus the maximum size of the Yukawa couplings Y_{ij} . Comparing the two results for the parameter space, it is observable that the parameter space projected on the chosen plane has a similar shape for both hierarchies. One could observe that the lower limit for the maximum size of Y increases if the dark matter mass increases. Furthermore, the largest Yukawa coupling is always of order $\mathcal{O}(1)$. This observation is expected because the Yukawa couplings have to be large enough to satisfy the constraint arising from the relic density, as explained in Chapter 6.4. The shape of this parameter space is also similar to the parameter space of the Scotogenic Model projected on the plane dark matter mass versus largest Yukawa coupling y_{ij} (see Fig. 5.2).

However, there is also a difference between the two hierarchies. For IH, the dark matter mass never exceeds 2.5 TeV, while higher masses up to 4 TeV seem to be possible for NH. The reason therefore could be that for IH the lepton flavor violation constraints arising from the decay $\mu \rightarrow e\gamma$ are significantly more restrictive than for NH, as shown in [61]. This enforces smaller Yukawa couplings in the IH case. As a consequence, the dark matter mass is forced into a narrower and lower range compared to the NH case to obtain the correct relic density.

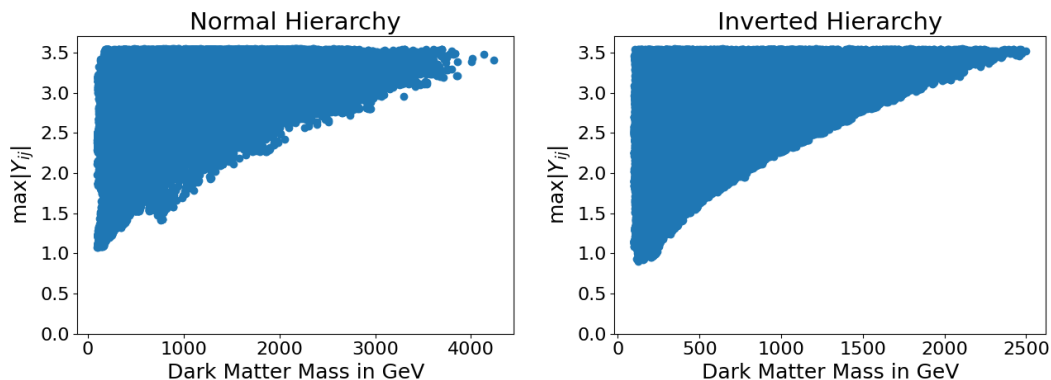


Figure 7.1: Our set of viable points projected on the plane of dark matter mass versus the maximum size of the Y_{ij} Yukawa couplings for NH (left) and IH (right).

7.4 Analysis of the RGE-effects

After performing the parameter scan, we want to investigate how the evolution of the renormalization group equations (RGEs) affects the consistency of our viable points because the running of the couplings might lead to the violation of theoretical constraints at higher scales.

The RGEs for the KNT-Model are derived by SARAH [41] and all relevant RGEs for our analysis are given in Appendix D. In our analysis, the evolution of the RGEs is performed for every viable point, from the weak scale up to the scale Λ_{\max} , where one of the theoretical constraints is violated. This is the case if the vacuum becomes unstable or some couplings are non-perturbative. Thus, Λ_{\max} is the scale up to which the KNT-Model is consistent. Therefore, the KNT-Model can only describe new physics beyond the Standard Model below Λ_{\max} . To perform the evolution of the RGEs, SciPy [50] is used.

We determine Λ_{\max} for every viable point. The results of this are shown in Figure 7.2 for NH in the left panel and for IH in the right panel. There Λ_{\max} is illustrated in dependence on the highest mass scale M_{\max} of the viable model. In addition to that, we also add a red line to the plot, which corresponds to $\Lambda_{\max} = M_{\max}$. If a parameter point lies below this red line, it is inconsistent because the corresponding viable model violates one of the constraints at an energy scale below its highest mass scale. Therefore, new physics would be required below an energy scale intrinsic to the model, which is not possible. Thus, we determined how many points are consistent with this criterion and find that for NH 4.46% of the points are consistent up to a scale $\Lambda_{\max} > M_{\max}$ and for IH 9.23% of the points are consistent. We also determined the fraction of the parameter space that is consistent up to the scales $2M_{\max} - 5M_{\max}$. The results for both hierarchies are shown in Table 7.2. Regarding this table, we see that only a small amount of points is consistent up to high energy scales once taking the RGE effects into account. The table also shows a difference between the two hierarchies because the number of consistent points is larger for IH than for NH. This could be explained by the limits of the parameter space. For NH, the dark matter mass can exceed larger values compared to those of IH. In addition, we determine the regions of the parameter space that remain consistent. This is illustrated in Figure 7.3, where a modified picture of the parameter space is shown. There we mark the points that are consistent up to $2M_{\max}$ respectively $5M_{\max}$ in different colors. This plot shows that consistent models tend to feature small dark matter masses. This explains why the scan for IH generates more consistent points than the scan for NH because the upper limit for the dark matter mass seems to be smaller in IH than in NH. Therefore, the percentage of points that are in regions of low dark matter masses is larger for IH compared to NH, which causes a higher percentage of consistent point in IH. We also see that consistent points feature small Yukawa couplings. This provides evidence that there could be a dependency between the size of the Yukawa couplings and the consistency, as is the case for the Scotogenic Model.

Furthermore, the reason why viable models become inconsistent is determined. Therefore, we differentiate between three scenarios, which are color coded in Figure 7.2. The viable points

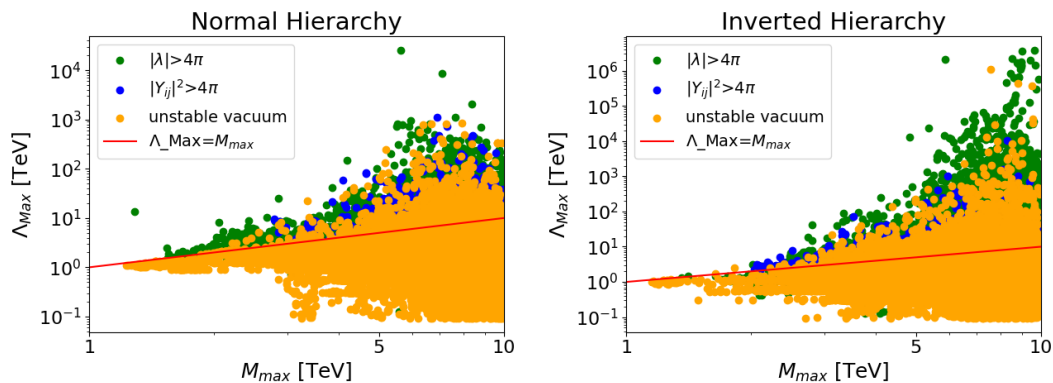


Figure 7.2: Scale of inconsistency Λ_{\max} as function of the largest mass scale M_{\max} in the model for NH (left) and IH (right). The color coding indicates the reason for the inconsistency. All models below the red line are inconsistent because their scale of inconsistency is below the largest mass scale.

Consistency Scale	Fraction of parameter space(NH)	Fraction of parameter space (IH)
M_{\max}	4.46%	9.23%
$2M_{\max}$	1.15%	2.95%
$3M_{\max}$	0.57%	1.67%
$4M_{\max}$	0.30%	1.21%
$5M_{\max}$	0.22%	0.99%

Table 7.2: Fractions of the parameter space that are consistent up to certain energy scale for NH and IH

become inconsistent because the vacuum becomes unstable (orange) or either the scalar couplings (green) or the Yukawa couplings (blue) become non-perturbative. In Table 7.3, the fractions of the parameter space for the different scenarios are given. The main scenario is the violation of vacuum stability with 85.46% for NH and 72.45% for IH. We also investigate which scenario is dominant in certain intervals of dark matter masses. Therefore, histograms for both hierarchies are made, which are shown in Figure 7.4. These histograms illustrate the relative frequencies for the different scenarios in different intervals of dark matter masses. The violation of vacuum stability is dominant in all intervals, but its influence increases if the dark matter mass increases. In addition, we observe the same behavior for the violation of the perturbativity of the Yukawa couplings. In contrast to that, the amount of points violating the perturbativity of the scalar couplings decreases if the dark matter mass increases. Regarding the parameter space, we notice that points with large dark matter masses tend to feature large Yukawa couplings. This is why the amount of points violating the perturbativity of the Yukawa couplings grows with the dark matter mass because these couplings become larger and are closer to the perturbativity limit. The increase in the number of points that violate the vacuum stability can also be explained by the increase in the size of Yukawa couplings because 99% of these points violate the condition $\lambda_{S_2} > 0$ at Λ_{\max} in both hierarchies.

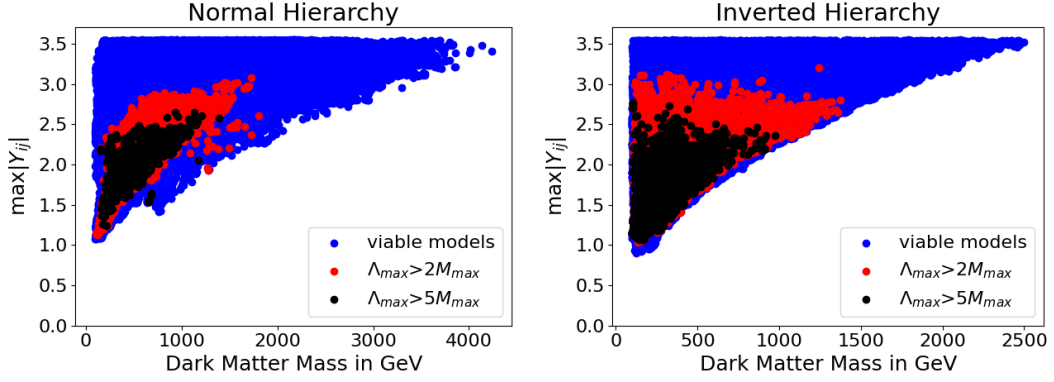


Figure 7.3: Modification of the parameter space once the RGE effects are taken into. The points consistent up to $2M_{\max}$ are color coded in red and the points consistent up to $5M_{\max}$ are color coded in black. Requiring consistency up to $2M_{\max}$ ($5M_{\max}$) leaves only 1.15% (0.22%) of the viable points for NH and 2.95% (0.99%) for IH.

Inconsistency scenario	Fraction of parameter space (NH)	Fraction of parameter space (IH)
unstable vacuum	85.46%	72.45%
$ \lambda > 4\pi$	12.31%	26.55%
$ Y_{ij} ^2 > 4\pi$	2.22%	1.00%

Table 7.3: Distribution of the viable points over the different scenarios for inconsistency for NH and IH.

Thus, the main reason for an inconsistency is that λ_{S_2} becomes negative. This behavior can be explained by the RGE of λ_{S_2} , which is proportional to the following term

$$\beta_{\lambda_{S_2}} \propto -4T_{4Y} = -4\text{Tr}(YY^\dagger YY^\dagger). \quad (7.11)$$

This term is similar to the term that causes the violation of vacuum stability in the Scotogenic Model, which is given in equation 5.8. In the case where the Yukawa couplings are large, this term increases. Then it is the main driving force in the RGE of λ_{S_2} and drives λ_{S_2} to negative values. This explains why the number of points that violate vacuum stability increases if the size of the Yukawa couplings increases.

Assuming that $\beta_{\lambda_{S_2}} \propto -4\text{Tr}(YY^\dagger YY^\dagger)$ is the dominant term in the RGEs, it is possible to derive an analytical estimate for Λ_{\max} , which is given by

$$\log\left(\frac{\Lambda_{\text{est}}}{\mu_0}\right) = \frac{4\pi^2 \lambda_{S_2}}{\text{Tr}(YY^\dagger YY^\dagger)} \Big|_{\mu=\mu_0}. \quad (7.12)$$

We calculate this estimate for every viable model that violates vacuum stability directly from the low-energy data and compare the estimated scale to the scale Λ_{\max} we found in our

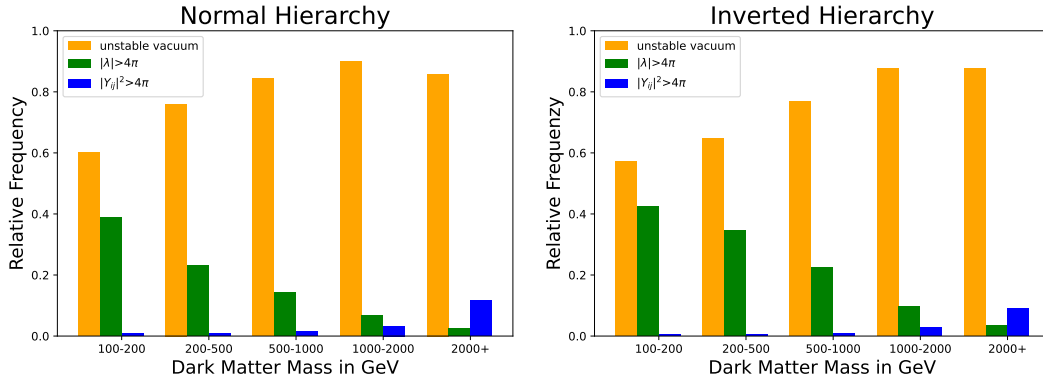


Figure 7.4: Relative frequencies of the different reasons for the inconsistency in different regions of the dark matter mass for NH (left) and IH (right)

numerical analysis. In Figure 7.5, the normalized density of the ratio $\Lambda_{\max}/\Lambda_{\text{est}}$ is illustrated for both hierarchies. The distributions for both hierarchies have a peak at almost $\frac{\Lambda_{\max}}{\Lambda_{\text{est}}} = 1$. This leads to the conclusion that the estimated scale and the scale Λ_{\max} found in the numerical analysis are almost the same for most of the points. Hence, our estimation works very well. This confirms our assumption that the term $\beta_{\lambda_{S_2}} \propto -4\text{Tr}(YY^\dagger YY^\dagger)$ is actually the dominant term in the RGEs. This leads to the conclusion that the consistency of our viable models is related to the size of the Yukawa couplings. If the Yukawa couplings become large, the model tends to become inconsistent. However, the Yukawa couplings have to be large enough to satisfy the constraint arising from the relic density if we consider the freeze-out mechanism without coannihilations. Thus, this constraint drastically restricts large parts of the parameter space.

In Figure 7.4, we observe that the number of points that violate the perturbativity of

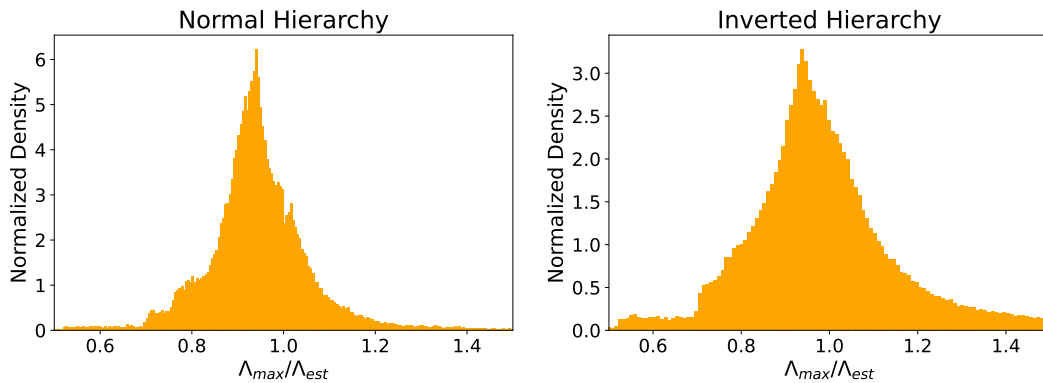


Figure 7.5: Distribution of the ratio $\Lambda_{\max}/\Lambda_{\text{est}}$ shown as normalized density for NH (left) and IH (right).

the scalar couplings falls if the dark matter mass increases. An explanation for this could be that for small dark matter masses the parameter space features more points with small

Yukawa couplings. For those points, the effect of the Yukawa couplings on the RGEs is smaller compared to points with large Yukawa couplings. According to that, there is a higher probability that other parameters, such as the scalar couplings, play an important role in the evolution of the RGEs. In that case, it is possible that the scalar couplings drive themselves to the perturbativity limit because the RGEs of the scalar couplings feature terms of the structure $\beta_\lambda \propto b\lambda^2$, where the coefficient b depends on the scalar coupling. The influence of the scalar couplings on the RGE effects is also analyzed in the next section.

7.5 Influence of the scalar couplings on the RGEs

In the next step, the influence of the scalar couplings on the RGE effects is analyzed. Therefore, we use the data we obtained from the scan, where the scalar couplings were scanned on a linear scale. These results are compared with the results from the scan, where the scalar couplings are scanned logarithmically. First of all, the scalar couplings should be larger in the linear scan than in the logarithmic scan. To ensure this, the largest scalar coupling is determined

$$|\lambda_{\max}| = |\max(\lambda_{S_1}, \lambda_{S_2}, \lambda_{HS_1}, \lambda_{HS_2}, \lambda_{S_1S_2}, \lambda'_{S_1S_2})| \quad (7.13)$$

for every viable point. In Figure 7.6, the normalized density of the largest scalar coupling is illustrated for the logarithmic and linear scan. There, it is observable that the distribution for the linear scan is actually more shifted towards larger values compared to the distribution for the logarithmic scan. We also calculate the mean value for the largest scalar coupling $\overline{|\lambda|}_{\max}$. For the logarithmic scan we get $\overline{|\lambda|}_{\max} = 8.130 \pm 0.002$ and for the linear scan $\overline{|\lambda|}_{\max} = 9.65 \pm 0.02$. Thus, the scalar couplings in the linear scan are larger on average than in the logarithmic scan.

After comparing the size of the scalar couplings, the evolution of the RGEs is performed for our data from the linear scan. In Figure 7.7, the parameter space projected onto the plane of dark matter mass versus the largest Yukawa coupling is illustrated for the logarithmic and linear scan. Here, we also mark the regions where the points remain consistent up to $2M_{\max}$ respectively $5M_{\max}$ in red and black. The plot shows that the parameter space seems to have the same shape in both scans and that the Yukawa couplings are always sizable for both scans. We also see that the regions where the points remain consistent feature small dark matter masses and small Yukawa couplings. Thus, the plots of the parameter space do not show big differences between the two scans. We also compare the results for Λ_{\max} for both scans. In Figure 7.8, Λ_{\max} in dependence on M_{\max} is shown for both scans. There we also notice no big difference between the two scans because the plots almost have the

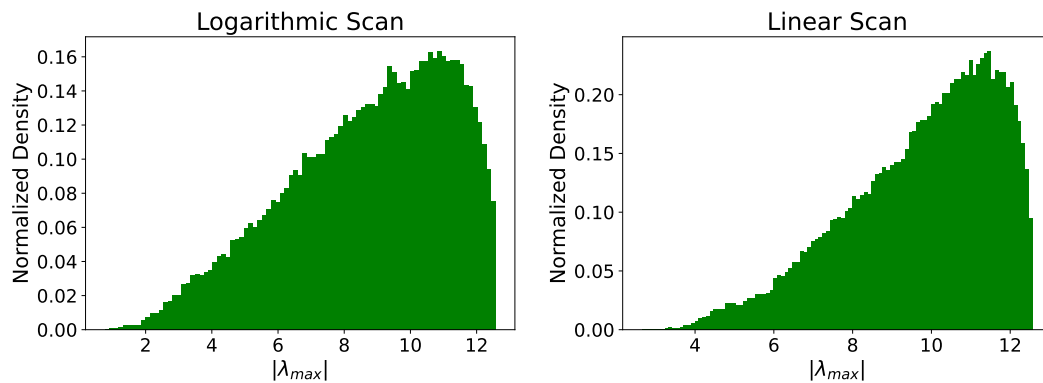


Figure 7.6: Normalized densities for $|\lambda_{\max}|$ for the points of the logarithmic scan (left) and the linear scan (right).

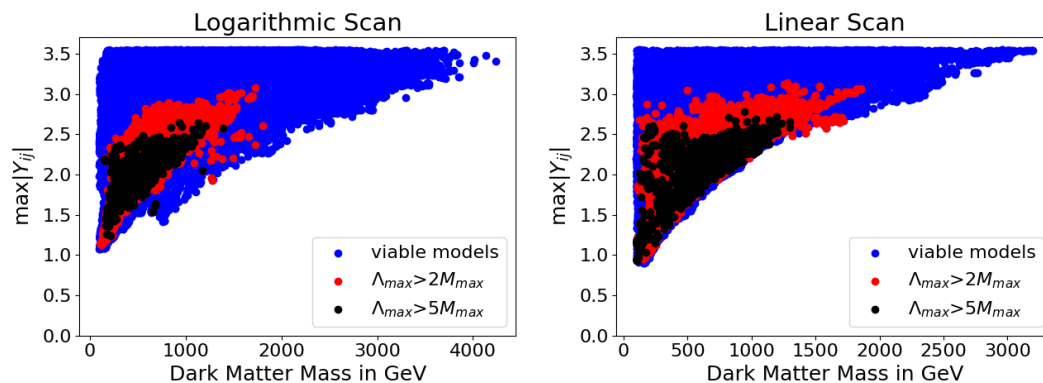


Figure 7.7: Our set of viable points projected on the plane of dark matter mass versus the maximum size of the Y_{ij} Yukawa couplings for the logarithmic scan (left) and the linear scan (right). Points that are consistent up to $2M_{\max}$ are colored in red and points that are consistent up to $5M_{\max}$ are colored in black.

same shape. However, if we analyze the number of points that are consistent up to certain scales, a difference between the two scans occurs. The fractions of the parameter space that are consistent up to certain scales are given in Table 7.4. This table shows that the number of consistent points is larger for the linear scan than for the logarithmic scan. The biggest difference is observed for M_{\max} because the amount of points that are consistent up to this scale is almost three times greater for the linear scan than for the logarithmic scan. For all other scales, the amount of points differs by a factor of approximately 2.

Another big difference arises regarding the reasons for the inconsistency. Table 7.5 shows how the viable points are distributed over the three scenarios. The results show that in the linear scan the dominant scenario is the violation of the perturbativity constraint for the scalar couplings with 72.84%, while the violation of vacuum stability is the main scenario for the logarithmic scan with 85.46%. This can also be seen in Figure 7.9. There, the histogram of the relative frequencies for the three different scenarios in different intervals of the dark

Consistency Scale	Fraction of parameter space (logarithmic scan)	Fraction of parameter space (linear scan)
M_{\max}	4.46%	12.64%
$2M_{\max}$	1.15%	2.24%
$3M_{\max}$	0.57%	0.93%
$4M_{\max}$	0.30%	0.57%
$5M_{\max}$	0.22%	0.42%

Table 7.4: Fractions of the parameter space that are consistent up to certain energy scales for the logarithmic and the linear scan.

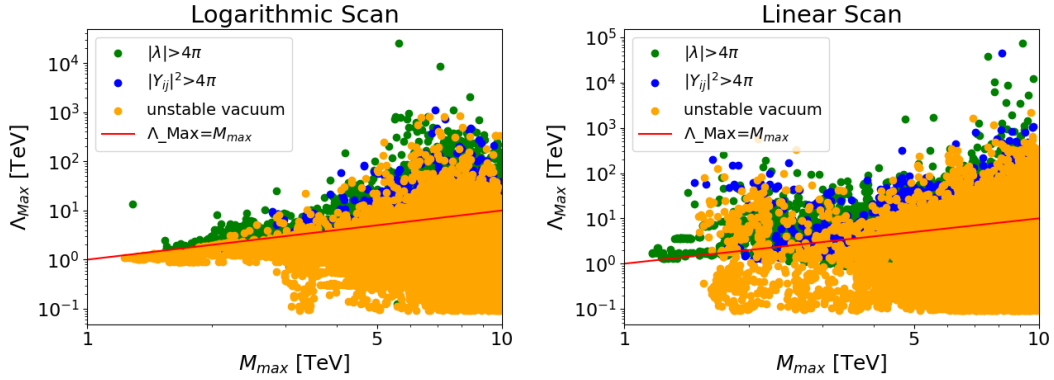


Figure 7.8: Scale of inconsistency Λ_{\max} as function of the largest mass scale M_{\max} in the model for the logarithmic scan (left) and the linear scan (right). The color coding indicates the reason for the inconsistency. All models below the red line are inconsistent because their scale of inconsistency is below the largest mass scale.

matter mass is illustrated. This histogram also shows that for the linear scan the scenario in which the scalar couplings become non-perturbative is the dominant one except for the case where the dark matter mass exceeds 2 TeV. There, the violation of the perturbativity of the Yukawa couplings becomes the dominant reason for the inconsistency. This behavior could be explained by the size of the scalar couplings. If they are larger, they are closer to the perturbativity limit, and it is more likely that they reach this limit. Furthermore, regarding the RGEs for the scalar couplings, we see that they feature terms that are proportional to a product of two scalar couplings

$$\beta_{\lambda_\alpha} \propto \sum_{\beta\delta} c_{\beta\delta} \lambda_\beta \lambda_\delta. \quad (7.14)$$

Here, the indices $\{\alpha, \beta, \delta\}$ stand for $\{H, S_1, S_2, HS_1, HS_2, S_1S_2\}$ and $c_{\beta\delta}$ stands for a coefficient which depends on the scalar couplings. Regarding the RGEs, it is observable that $c_{\beta\delta} \geq 0$ for all β, δ . We assume that these terms become dominant if the scalar couplings are large. In this case, the scalar couplings drive themselves to the perturbativity limit. This behavior could also explain why the violation of the vacuum stability is the weakest reason

for inconsistency in the linear scan. In our analysis of the logarithmic scan, most of the points violate the vacuum stability because λ_{S_2} becomes negative. The main driving force for this is the term $\beta_{\lambda_{S_2}} \propto -4\text{Tr}(YY^\dagger YY^\dagger)$ because of the sizable Yukawa couplings. If the scalar couplings are also large, the terms proportional to them counteract this term because these terms have different signs. This is why it is more likely that one of the scalar couplings becomes non-perturbative before the vacuum stability is violated. This behavior could also explain why the linear scan generates more consistent points compared to the logarithmic scan because the counteraction of the terms proportional to the scalar couplings against the term featuring the Yukawa couplings could lead to a violation of the theoretical constraints at higher scales.

However, we observe that the amount of consistent points generated by the linear scan is still small because if the scalar couplings are too large, the perturbativity criterion is often violated. There is also no phenomenological reason that requires the scalar couplings to be large, like the constraint arising from the relic density which forces the Yukawa couplings to be sizable. Comparing the pictures of the parameter space for the linear and logarithmic scan in Figure 7.7, we observe that the size of the scalar coupling has no big impact on the rest of the parameter space. Therefore, it should be possible to require small scalar couplings without modifying the rest of the parameter space. Thus, if one wants to get more consistent points, it is a better strategy to decrease the size of the Yukawa couplings than to increase the size of the scalar couplings. If the Yukawa couplings and the scalar couplings tend to be small, the perturbativity criterion and the vacuum stability should be satisfied up to high energy scales, and more points of the parameter space should remain consistent. As for the Scotogenic Model, one could also consider coannihilations between the singlet fermions to decrease the size of the Yukawa couplings. In addition to that, it is also possible to consider the freeze-in scenario. As we know so far, these two approaches have not been studied yet for the KNT-Model, but it would be possible that they lead to smaller Yukawa couplings. The reason therefore is that they work for the Scotogenic Model and as we have seen in our analysis, the KNT-Model shows a similar behavior as the Scotogenic Model in many ways. In the Scotogenic Model, we also suggested that considering scalar dark matter avoids large Yukawa couplings, but this does not work for the KNT-Model because this model features no scalar dark matter candidate, since the odd scalar particles are charged.

Inconsistency scenario	Fraction of parameter space (logarithmic scan)	Fraction of parameter space (linear scan)
unstable vacuum	85.46%	5.82%
$ \lambda > 4\pi$	12.31%	72.84%
$ Y_{ij} ^2 > 4\pi$	2.22%	21.34%

Table 7.5: Distribution of the viable points over the different scenarios for inconsistency for the logarithmic scan and the linear scan.

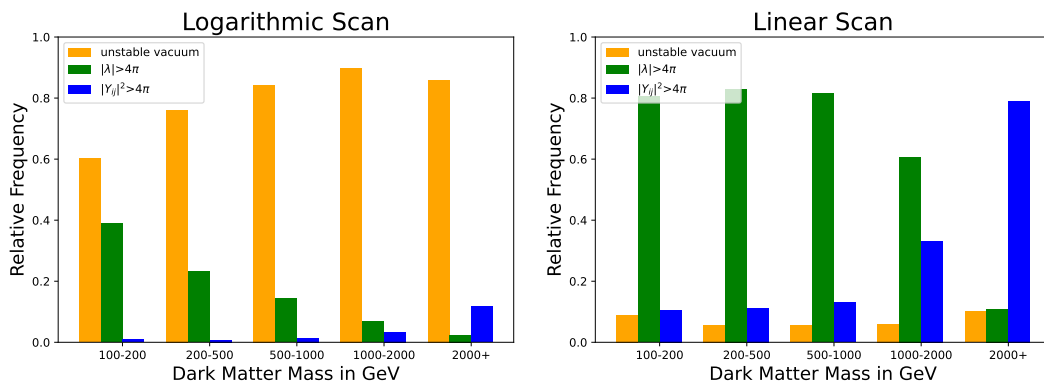


Figure 7.9: Relative frequencies of the different reasons for the inconsistency in different regions of the dark matter mass for the logarithmic scan (left) and the linear scan (right)

8 Conclusion

In this thesis, we studied two radiative seesaw models, the Scotogenic Model [[5], [6]] and the KNT-Model [7]. Therefore, a scan of the viable parameter space was performed and the evolution of the renormalization group equations was performed for every viable point.

After performing the parameter scan, we found that some Yukawa couplings are always sizable. This observation could be made for both models. This event can be explained by the constraint arising from the dark matter relic density because the annihilation cross sections are velocity suppressed in both models. Thus, the Yukawa couplings have to be large enough to obtain the correct relic density.

After scanning the viable parameter space, the effect of the renormalization group evolution on the parameter space was studied because this evolution could lead to a violation of the vacuum stability or the perturbativity constraints at higher scales. We followed the renormalization group evolution for each viable point from the weak scale up to a scale Λ_{\max} , where one of the theoretical constraints is violated. Thus, the model only describes new physics below Λ_{\max} . In our analysis, we found that large parts of the parameter space violate one of the conditions before reaching the highest mass scale of the model M_{\max} . If this is the case, the model is inconsistent because it violates the imposed constraints below an energy scale intrinsic to itself. We found that for the Scotogenic Model 89.39% of our viable points were inconsistent and for the KNT-Model 95.54% of our viable models were inconsistent for NH and 90.77% for IH. Hence, the effects of the renormalization group evolution drastically reduced the size of the parameter space.

We also investigated the reasons for the violation of the theoretical constraints and found that there is a scalar coupling in the Scotogenic Model (λ_2) as well as in the KNT-Model (λ_{S_2}) which is driven towards negative values because of the sizable Yukawa couplings. This leads to the conclusion that the constraint arising from the relic density is a stringent constraint for the parameter space because it causes sizable Yukawa couplings which lead to the violation of vacuum stability. Therefore, the violation of vacuum stability is actually an intrinsic and important feature of the two models with fermionic WIMP dark matter.

We also found that points that violate the perturbativity of the scalar couplings tend to feature large scalar couplings. However, in contrast to the Yukawa couplings, the phenomenology

does not require them to be large. Therefore, it should be possible to consider smaller scalar couplings without modifying the rest of the parameter space. This was checked for the KNT-Model. We scanned the scalar couplings logarithmically and linearly and compared the results. In the linear scan, the scalar couplings obviously tended to be larger compared to the logarithmic scan, but that the rest of the parameter space was not really affected. The numerical analysis showed that less points from the logarithmic scan violated the perturbativity criterion compared to the linear scan. Thus, it is possible to avoid the violation of the perturbativity criterion by choosing smaller scalar couplings.

In contrast to that, it is more difficult to avoid the violation of vacuum stability because it requires small Yukawa couplings, while sizable Yukawa couplings are required by the relic density. Thus, one has to find a way to decrease the Yukawa couplings, while still obtaining the correct relic density. Some ideas for this are given in [40]. There, they suggested that smaller Yukawa couplings can be reached by considering coannihilations in the freeze-out mechanism the freeze-in mechanism to obtain the relic density. This has already been studied for the Scotogenic Model and it has been shown that these approaches actually lead to smaller Yukawa couplings. For the KNT-Model, these approaches have not been studied yet, as we know so far. Thus, it could be the next step to study these approaches in the KNT-Model.

A Lepton Flavor Violation

In this chapter, we want to describe how the branching ratios of lepton flavor violating processes of the form $l_\alpha \rightarrow l_\beta$ are calculated. This calculation is taken from [36].

Thus, we want to compute the process $l_\alpha(p_1) \rightarrow l_\beta(p_2)\gamma(q)$ with $q = p_1 - p_2$. First, we have to calculate the amplitude of this process to get the branching ratio. The amplitude of such a decay is given by $e\epsilon_\mu^* M^\mu$ with the electric charge of a positron e and the polarization vector ϵ_μ^* . Due to gauge invariance $q_\mu M^\mu$ has to vanish. Therefore, M^μ must contain the form with the coefficients σ_L , σ_R , δ_L and δ_R

$$M^\mu = \bar{u}_\beta [i\sigma^{\mu\nu} q_\nu (\sigma_L \gamma_L + \sigma_R \gamma_R) + \delta_L \Delta_L^\mu + \delta_R \Delta_R^\mu] u_\alpha \quad (\text{A.1})$$

Here, u_α and \bar{u}_β represent l_α and l_β , $\sigma^{\mu\nu}$ is defined as $\sigma^{\mu\nu} = \frac{i}{2}[\gamma^\mu, \gamma^\nu]$, γ_L and γ_R are the projectors of chirality and Δ_L^μ and Δ_R^μ are given by

$$\Delta_L^\mu = q^\mu \gamma_L + \frac{q^2}{m_\beta^2 - m_\alpha^2} \gamma^\mu (m_\beta \gamma_L + m_\alpha \gamma_R) \quad (\text{A.2})$$

$$\Delta_R^\mu = q^\mu \gamma_R + \frac{q^2}{m_\beta^2 - m_\alpha^2} \gamma^\mu (m_\beta \gamma_R + m_\alpha \gamma_L) \quad (\text{A.3})$$

Here, m_α and m_β are the masses of l_α and l_β . We can use the fact that the photon is on-shell in this process and $q^2 = 0$. Furthermore, we use the identity $\epsilon_\mu^*(q)q^\mu = 0$. Therefore, only the coefficients σ_L and σ_R are relevant for the calculation of the amplitude. These coefficients can be given in terms of loop integrals, which are also given in [36]. The decay width for our process is given by

$$\Gamma_{\alpha \rightarrow \beta \gamma} = \frac{(m_\alpha^2 - m_\beta^2)^3 (|\sigma_L|^2 + |\sigma_R|^2)}{16\pi m_\alpha^3} \quad (\text{A.4})$$

The branching ratio $\text{BR}(l_\alpha \rightarrow l_\beta \gamma)$ is defined as the decay width of the process $l_\alpha \rightarrow l_\beta \gamma$ divided by the total decay width of l_α . Here, we can use the fact that the branching ratios of the processes $l_\alpha \rightarrow l_\beta \nu \bar{\nu}$ are measured in experiments [30] and the decay width for these

processes is given by $\Gamma_{\alpha \rightarrow \beta \nu \bar{\nu}} \approx \frac{G_F^2 m_\alpha^5}{192\pi^3}$ with the Fermi constant G_F . Hence, we can calculate the branching ratio for our process by

$$\text{BR}(l_\alpha \rightarrow l_\beta \gamma) = \frac{\Gamma_{\alpha \rightarrow \beta \gamma}}{\Gamma_{\alpha \rightarrow \beta \nu \bar{\nu}}} \text{BR}(l_\alpha \rightarrow l_\beta \nu \bar{\nu}) \quad (\text{A.5})$$

Furthermore, we use $m_\alpha \gg m_\beta$ and $\frac{m_\beta}{m_\alpha} \ll 1$ in the processes we calculate. Therefore, we can simplify the branching ratio

$$\text{BR}(l_\alpha \rightarrow l_\beta \gamma) = \frac{12\pi^2}{G_F^2 m_\alpha^2} (|\sigma_L|^2 + |\sigma_R|^2) \text{BR}(l_\alpha \rightarrow l_\beta \nu \bar{\nu}) \quad (\text{A.6})$$

In our models, the lepton flavor violation processes are allowed at one-loop level because of the interaction of l_α and l_β with an additional spin-0 boson B and a fermion F . The Lagrangian for this interaction is given by

$$\mathcal{L}_{Yuk} = \sum_{i=\alpha,\beta} B \bar{F} (L_i \gamma_L + R_i \gamma_R) l_i + B^* \bar{l}_i (L_i^* \gamma_L + R_i^* \gamma_R) F \quad (\text{A.7})$$

with dimensionless coefficients L_α , L_β , R_α and R_β . These coefficients can be used to calculate the following coefficients

$$\begin{aligned} \lambda &= L_\beta^* L_\alpha \\ \rho &= R_\beta^* R_\alpha \\ \zeta &= L_\beta^* R_\alpha \\ \nu &= R_\beta^* L_\alpha \end{aligned} \quad (\text{A.8})$$

These interactions lead to four possible Feynman diagrams, which are shown in Figure A.1. There are two self-energy diagrams in which the photon attaches either to l_α or l_β and these diagrams are proportional to $Q_l = -e$, which is the charge of the leptons. In the other diagrams, the photon attaches to F or B . Thus, these diagrams are proportional to the charges Q_F or Q_B of F or B . Furthermore, $Q_l = Q_F - Q_B$ has to be satisfied. That is why σ_L and σ_R can be written in terms of Q_F and Q_B as

$$\begin{aligned} \sigma_L &= Q_F(\rho k_1 + \lambda k_2 + \nu k_3) + Q_B(\rho \bar{k}_1 + \lambda \bar{k}_2 + \zeta \bar{k}_3) \\ \sigma_R &= Q_F(\lambda k_1 + \rho k_2 + \zeta k_3) + Q_B(\lambda \bar{k}_1 + \rho \bar{k}_2 + \nu \bar{k}_3) \end{aligned} \quad (\text{A.9})$$

Here, k_i and \bar{k}_i are constructed using loop functions

$$\begin{aligned}
k_1 &= m_\alpha(c_1 + d_1 + f) \\
k_2 &= m_\beta(c_2 + d_2 + f) \\
k_3 &= m_F(c_1 + c_2) \\
\bar{k}_1 &= m_\alpha(-\bar{c}_1 + \bar{d}_1 + \bar{f}) \\
\bar{k}_2 &= m_\beta(-\bar{c}_2 + \bar{d}_2 + \bar{f}) \\
\bar{k}_3 &= m_F(-\bar{a} + \bar{c}_1 + \bar{c}_2)
\end{aligned} \tag{A.10}$$

Here, m_F denotes the mass of F . The loop integrals are given in [36]. Using the approximation $m_\alpha^2 = m_\beta^2 = 0$ and $q^2 = 0$, they can be expressed as

$$\begin{aligned}
a &= \frac{i}{16\pi^2 m_B^2} \left[\frac{-1}{t-1} + \frac{\ln t}{(t-1)^2} \right] \\
c_1 = c_2 \equiv c &= \frac{i}{16\pi^2 m_B^2} \left[\frac{t-3}{4(t-1)^2} + \frac{\ln t}{2(t-1)^3} \right] \\
d_1 = d_2 = 2f \equiv d &= \frac{i}{16\pi^2 m_B^2} \left[\frac{-2t^2 + 7t - 11}{18(t-1)^3} + \frac{\ln t}{3(t-1)^4} \right] \\
\bar{a} &= \frac{i}{16\pi^2 m_B^2} \left[\frac{1}{t-1} + \frac{t \ln t}{(t-1)^2} \right] \\
\bar{c}_1 = \bar{c}_2 \equiv \bar{c} &= \frac{i}{16\pi^2 m_B^2} \left[\frac{3t-1}{4(t-1)^2} - \frac{t^2 \ln t}{2(t-1)^3} \right] \\
\bar{d}_1 = \bar{d}_2 = 2\bar{f} \equiv \bar{d} &= \frac{i}{16\pi^2 m_B^2} \left[\frac{11t^2 - 7t + 2}{18(t-1)^3} - \frac{t^3 \ln t}{3(t-1)^4} \right]
\end{aligned} \tag{A.11}$$

Here, m_B is the mass of the scalar boson B and t denotes $t = \frac{m_F^2}{m_B^2}$.

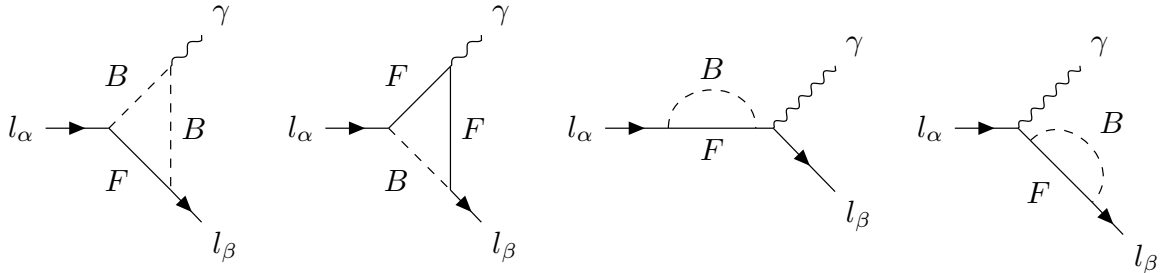


Figure A.1: 1-loop Feynman diagrams for the process $l_\alpha \rightarrow l_\beta$

A.1 Scotogenic Model

We want to calculate the branching ratio for the process $l_\alpha \rightarrow l_\beta \gamma$ in the Scotogenic Model. Therefore, we have to bring the interaction Lagrangian of the Scotogenic Model given in equation 4.1 into the form of equation A.7. The scalar boson is the charged part of the new scalar doublet η^+ and the fermion is represented by the right-handed fermions N_i . Therefore, we can write the interaction Lagrangian as

$$\mathcal{L}_{\alpha\beta} = -y_{i\alpha}\eta^+\bar{N}_i\gamma_L l_\alpha - y_{i\alpha}^*(\eta^+)^*\bar{l}_\alpha\gamma_R N_i \quad (\text{A.12})$$

$$-y_{i\beta}\eta^+\bar{N}_i\gamma_L l_\beta - y_{i\beta}^*(\eta^+)^*\bar{l}_\beta\gamma_R N_i \quad (\text{A.13})$$

Thus, we get for the coefficients $L_\alpha = y_{i\alpha}$, $L_\beta = y_{i\beta}$ and $R_\alpha = R_\beta = 0$. Then we can calculate the other coefficients

$$\begin{aligned} \lambda &= y_{i\beta}^* y_{i\alpha} \\ \rho &= 0 \\ \zeta &= 0 \\ \nu &= 0 \end{aligned} \quad (\text{A.14})$$

Now we can use the fact that the right-handed fermions are neutral ($Q_F = 0$) and the charged scalar has the charge $Q_B = e$. Therefore, we get for σ_L and σ_R

$$\begin{aligned} \sigma_L &= e y_{i\beta}^* y_{i\alpha} \bar{k}_2 \\ \sigma_R &= e y_{i\beta}^* y_{i\alpha} \bar{k}_1 \end{aligned} \quad (\text{A.15})$$

Using the loop function given in A.11, we get the following

$$|\sigma_L|^2 + |\sigma_R|^2 = \left| \frac{e y_{i\beta}^* y_{i\alpha}}{16\pi^2 m_\eta^2} \frac{2t^3 + 3t^2 - 6t^2 \ln t - 6t + 1}{12(t-1)^4} \right|^2 (m_\beta^2 + m_\alpha^2) \quad (\text{A.16})$$

with $t = \frac{m_{N_i}^2}{m_\eta^2}$. If we use the approximation $m_\alpha \gg m_\beta$ again, we get as a result the branching ratio

$$\text{BR}(l_\alpha \rightarrow l_\beta \gamma) = \frac{3\pi\alpha_{em}}{2G_F^2 m_\eta^2} |y_{i\beta}^* y_{i\alpha}|^2 F_2 \left(\frac{m_{N_i}^2}{m_\eta^2} \right) \text{BR}(l_\alpha \rightarrow l_\beta \nu \bar{\nu}) \quad (\text{A.17})$$

with the loop factor

$$F_2(t) = \frac{2t^3 + 3t^2 - 6t^2 \ln t - 6t + 1}{6(t-1)^4} \quad (\text{A.18})$$

A.2 KNT-Model

In the KNT-Model, we have two candidates for the scalar boson and the fermion. Thus, the process $l_\alpha \rightarrow l_\beta \gamma$ can be realized via interactions of the leptons with the scalar boson S_1 and the neutrinos ν_i or interactions with the scalar boson S_2 and the right-handed fermions N_i . That is why we have to consider both cases to calculate the branching ratio. First, we calculate the branching ratio for the interaction with S_1 and neutrinos. Therefore, we have to bring the interaction Lagrangian given in 6.1 into the form of A.7

$$\mathcal{L}_{\alpha\beta 1} = -\tilde{Y}_{\alpha i} S_1 \bar{\nu}_i \gamma_L l_\alpha - \tilde{Y}_{\alpha i}^*(S_1)^* \bar{l}_\alpha \gamma_R \nu_i \quad (\text{A.19})$$

$$-\tilde{Y}_{\beta i} S_1 \bar{\nu}_i \gamma_L l_\beta - \tilde{Y}_{\beta i}^*(S_1)^* \bar{l}_\beta \gamma_R \nu_i \quad (\text{A.20})$$

Thus, we get the coefficients $L_\alpha = \tilde{Y}_{\alpha i}$, $L_\beta = \tilde{Y}_{\beta i}$ and $R_\alpha = R_\beta = 0$. Here, we see that the same coefficients vanish as in the Scotogenic Model. Furthermore, the fermion ν_i is neutral and the boson S_1 is charged with $Q_{S_1} = e$ as it is in the Scotogenic Model. Therefore, we will get the same result as for the Scotogenic Model. We just have to change the Yukawa couplings and get the following

$$\text{BR}_1(l_\alpha \rightarrow l_\beta \gamma) = \frac{3\pi\alpha_{em}}{2G_F^2 m_{S_1}^2} |\tilde{Y}_{\beta i}^* \tilde{Y}_{\alpha i}|^2 F_2 \left(\frac{m_{\nu_i}^2}{m_{S_1}^2} \right) \text{BR}(l_\alpha \rightarrow l_\beta \nu \bar{\nu}) \quad (\text{A.21})$$

with the loop factor

$$F_2(t) = \frac{2t^3 + 3t^2 - 6t^2 \ln t - 6t + 1}{6(t-1)^4} \quad (\text{A.22})$$

Here, we can use the fact that the masses of the left-handed neutrinos are very small compared to the other masses in the model ($\frac{m_\nu^2}{m_{S_1}^2} \approx 0$). We can simplify the branching ratio by taking $F_2(0) = \frac{1}{6}$. This brings us to

$$\text{BR}_1(l_\alpha \rightarrow l_\beta \gamma) = \frac{\pi\alpha_{em}}{4G_F^2 m_{S_1}^2} |\tilde{Y}_{\beta i}^* \tilde{Y}_{\alpha i}|^2 \text{BR}(l_\alpha \rightarrow l_\beta \nu \bar{\nu}) \quad (\text{A.23})$$

At least we calculate the branching ratio for the interaction with S_2 and the right-handed neutrinos. Therefore, we bring the interaction Lagrangian in the form of A.7 again

$$\mathcal{L}_{\alpha\beta} = Y_{i\alpha} S_2 \bar{N}_i \gamma_L l_\alpha + Y_{i\alpha}^*(S_2)^* \bar{l}_\alpha \gamma_R N_i \quad (\text{A.24})$$

$$Y_{i\beta} S_2 \bar{N}_i \gamma_R l_\beta + Y_{i\beta}^*(S_2)^* \bar{l}_\beta \gamma_L N_i \quad (\text{A.25})$$

Here, we get the coefficients $R_\alpha = Y_{i\alpha}$, $R_\beta = Y_{i\beta}$ and $L_\alpha = L_\beta = 0$. This brings us to the following coefficients: $\rho = Y_{i\beta}^* Y_{i\alpha}$ and $\lambda = \zeta = \nu = 0$. Now we can use the fact the N_i is neutral and S_2 has the charge $Q_{S_2} = 0$ to calculate

$$\begin{aligned}\sigma_L &= eY_{i\beta}^* Y_{i\alpha} \bar{k}_1 \\ \sigma_R &= eY_{i\beta}^* Y_{i\alpha} \bar{k}_2\end{aligned}\tag{A.26}$$

Thus, using the loop functions in A.11, we get the branching ratio

$$\text{BR}_2(l_\alpha \rightarrow l_\beta \gamma) = \frac{3\pi\alpha_{em}}{2G_F^2 m_{S_2}^2} |Y_{i\beta}^* Y_{i\alpha}|^2 F_2\left(\frac{m_{N_i}^2}{m_{S_2}^2}\right) \text{BR}(l_\alpha \rightarrow l_\beta \nu \bar{\nu})\tag{A.27}$$

Hence, we get the total branching ratio of this process

$$\begin{aligned}\text{BR}(l_\alpha \rightarrow l_\beta \gamma) &= \text{BR}_1(l_\alpha \rightarrow l_\beta \gamma) + \text{BR}_2(l_\alpha \rightarrow l_\beta \gamma) \\ &= \frac{\pi\alpha_{em}}{G_F^2} \left(\frac{|\tilde{Y}_{\beta i}^* \tilde{Y}_{\alpha i}|^2}{4m_{S_1}^2} + \frac{3|Y_{i\beta}^* Y_{i\alpha}|^2}{2m_{S_2}^2} \right) \text{BR}(l_\alpha \rightarrow l_\beta \nu \bar{\nu})\end{aligned}\tag{A.28}$$

B Methods

In this thesis, we want to perform parameter scans for radiative seesaw models. Our first attempt to do that was to perform a random scan, but we found out that this is really slow and that it takes a long time to collect enough data for further analysis. Thus, we had to come up with a different strategy. This chapter introduces the methods we used for our parameter scan.

B.1 Monte-Carlo-Markov-Chain

The sampling of the parameter space is done by a Monte-Carlo-Markov-Chain (MCMC) ensemble sampling. This method is introduced in this section. First, we explain the basic idea and properties of a Monte-Carlo-Markov-Chain. After that, we extend this idea to MCMC ensemble sampling. This section is based on [62].

B.1.1 MCMC

The aim of a Monte-Carlo-Markov-Chain (MCMC) is to characterize a distribution without knowing its analytical expression by trying to sample values randomly out of the distribution. This is can very useful in Bayesian inference, because in this context one often deals with the problem of giving an analytical expression of the posterior distribution $p(x|D)$. Although it is possible to calculate the likelihood $p(D|x)$ and the prior $p(x)$ for a point x and given data D . Then the posterior is proportional to the product of prior and likelihood

$$p(x|D) \propto p(D|x) \cdot p(x) \tag{B.1}$$

MCMC combines the properties of Monte-Carlo sampling and Markov-Chains. Monte-Carlo sampling describes the idea of characterizing a distribution by sampling from it randomly. Markov-Chains are series of points, where every point depends only on its previous point, which is called Markov-Property. Thus, the idea of MCMC is to use the current point x_i in the sampling process to make a proposal for the next point x_{i+1} . After proposing a new point x_{i+1} , an acceptance probability $p(x_{i+1}|x_i)$ is calculated. Then the proposed point is

accepted with the calculated probability. If the proposed point is accepted, it becomes the next point in the chain. Otherwise, the chain stays in the previous state. The acceptance probability compares the posterior of the proposed point with the posterior of the previous point and is given by

$$p(x_{i+1}|x_i) = \frac{p(x_{i+1}|D)}{p(x_i|D)} = \frac{p(D|x_{i+1})p(x_{i+1})}{p(D|x_i)p(x_i)} \quad (\text{B.2})$$

This is the basic idea of MCMC. However, one still has to define, how to propose the next step. There are many different approaches for this process. An easy way to propose a new point x_{i+1} is to add a small perturbation δ to the current point x_i

$$x_{i+1} = x_i + \delta \quad (\text{B.3})$$

However, there is still the question of how to choose δ , which remains. In our following example, δ is generated from a proposal distribution, which is a normal distribution $\mathcal{N}(0, \sigma)$ with a mean value of 0 and a standard deviation σ . The choice of σ depends on the distribution from which we want to sample. If σ is too small, the chain makes very small steps and it takes a long time to sample the whole distribution. Then the sampling process becomes inefficient. Otherwise, if σ is too large, the chain can make too big steps. In this case, it is very likely that the chain jumps out of the distribution and the acceptance probability becomes small. In this case, the chain could stay in the same position for a long time, and the sampling process also becomes inefficient. This is, why one has to choose σ carefully. In practice, it is very common to do the sampling multiple times with different σ to choose the best σ in the end. Thus, σ is a tuning parameter.

We want to do an MCMC sampling process for a simple example to practice this method and to analyze the influence of the starting point x_0 in the chain and the tuning parameter σ . Therefore, we used MCMC sampling to sample from a normal distribution $\mathcal{N}(0, 10)$ with a mean value $\mu_0 = 0$ and a standard deviation $\sigma_0 = 10$. First, we did a sampling for 5000 steps and used $x_0 = 1$ as the starting point and $\sigma = 10$ as the tuning parameter. Thus, the proposal distribution is $\mathcal{N}(0, 10)$. The results for this sampling are shown in figure B.1, where we plotted the sampling results after different amount of steps. We also added the distribution, from which we sample, to the plots to see, how well our sampling results represent this distribution. There one can observe, that the sampled values fit the sampling distribution better, if the sampling is done for more steps. The results after 100 and even after 500 steps do not really show the shape of the sampling distribution. After 1000 steps the sampled values begin to show the shape of the expected distribution, but the result is still not good. However, it gets better after doing more iterations in the sampling process and after 5000

steps, one can observe, that the sampled values represent the sampling distribution very well. This leads to the conclusion that the Markov chain needs some time to converge.

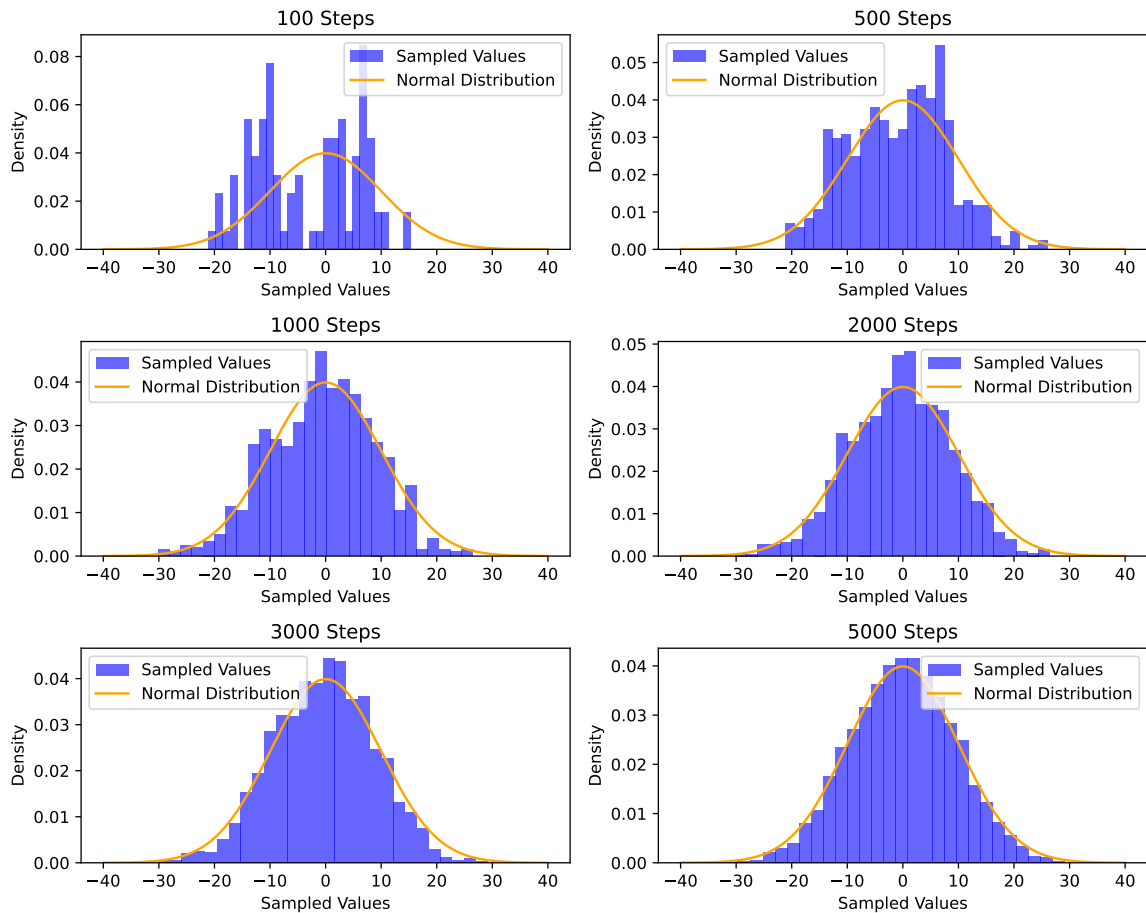


Figure B.1: Sampling results after different amount of steps (blue) and Sampling Distribution (orange)

In the next step, we want to investigate the influence of the tuning parameter σ on the sampling process. Therefore, we conduct the sampling process with $\sigma = 1, 10, 100$. We choose $x_0 = 10$ as the starting point in every sampling process, and every sampling is done for 5000 steps. Our results are shown in figure B.2. For every σ , we made a plot showing the sampled values in dependence on the iteration, and a plot showing the density of the sampled values and the sampling distribution. For $\sigma = 1$ one can observe, that the sampled values oscillate less than for larger σ . This means, that the chain moves slower than for $\sigma = 10, 100$. It is also observable, that the sampled values do not represent the sampling distribution very well. The reason for this could be, that the 5000 steps were not enough for the Chain to converge because of the slow motion. This is why $\sigma = 1$ is not a good choice for σ , because it might be too small. For $\sigma = 10$ one can see, that the sampled values oscillate faster than for $\sigma = 1$ and that there are no observable points, where the chain stays in one position for some

iterations. Looking at the density of the sampled values, we see that the data fit the sampling distribution very well. This leads to the conclusion that the chain has already converged and that $\sigma = 10$ might be a good choice. At least, we did the sampling with $\sigma = 100$. Therefore, we see, that the chain can make big steps and the sampled values also oscillate faster than for $\sigma = 1$, but looking at the sampled values in dependence on the iteration, we also observe some points, where the chain does small steps or stays in one position over a few iterations. This means, that at these points the proposed steps are not accepted and the chain does not move. This behavior is typical, if σ is too large. Regarding the density of the sampled values, one also comes to the conclusion, that the sampled values do not fit the expected distribution well and that $\sigma = 100$ might not be a good choice.

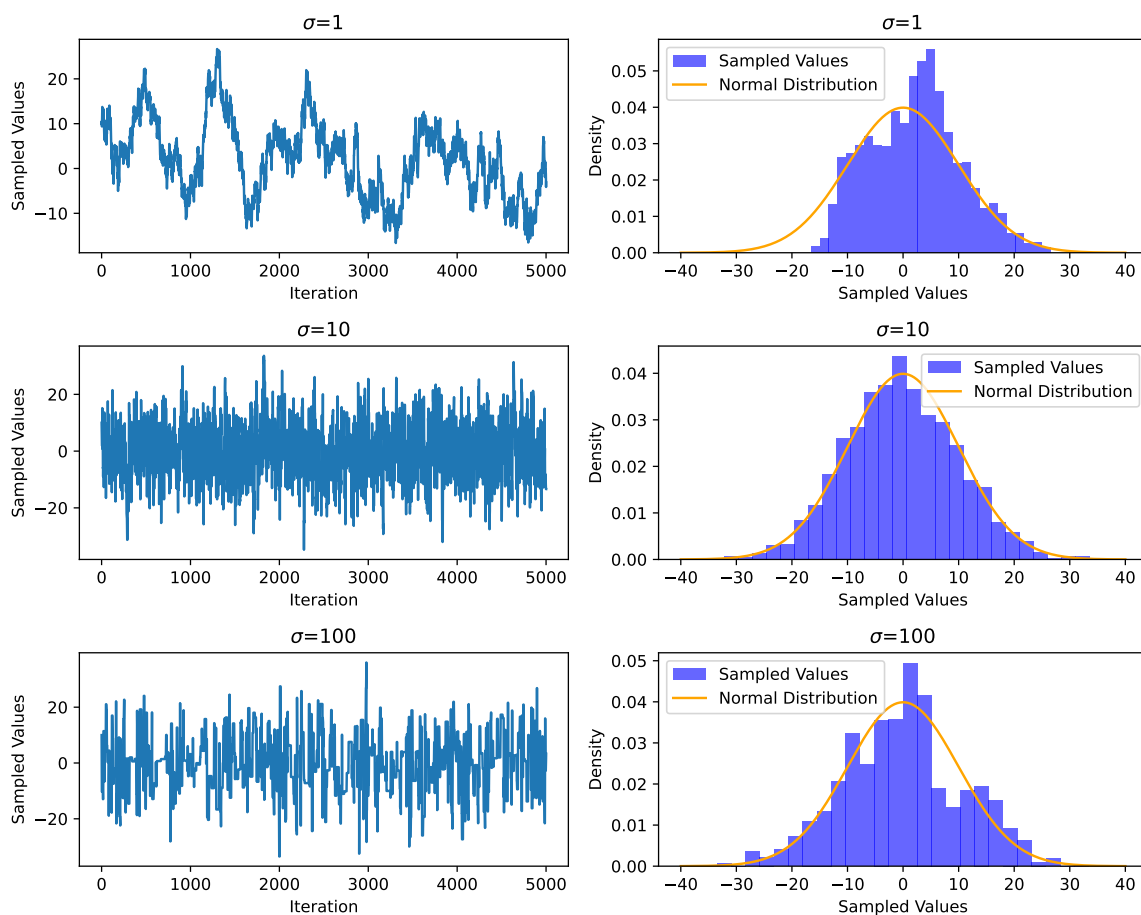


Figure B.2: The evolution of the Markov Chain (left) and the density of the sampled values (right) for different values for σ

At least we want to investigate the influence of the starting value of the sampling process. Therefore, we conduct the sampling process for the starting values $x_0 = 1, 100, 300$. Here, we choose $\sigma = 10$ and perform the sampling processes for 5000 steps. The results are shown in figure B.3. We do a plot showing the density of the sampled values and the sampling

distribution and a plot showing the sampled values for the first 300 steps of the chain for each starting value. The first observation is that the sampled values represent the expected distribution very well for all three starting values. Thus, it seems that the chain converged in all three cases. Furthermore, we observe that the density for values in the region of the starting value for $x_0 = 100, 300$ is not observable in the plots. Hence, the density there is really low, as it should be. Regarding the Markov-Chains for the first 300 steps, one can observe that the sampled values start to oscillate directly from the beginning for $x_0 = 1$. For $x_0 = 100$ and $x_0 = 300$, the chain does not oscillate from the beginning. Instead, the values of the chain decrease until the right region of the distribution is reached. For $x_0 = 100$ it takes approximately 50 steps, and for $x_0 = 300$ 150. This period is called burn-in phase. Thus, we can conclude that the chain needs some time for the burn-in if the starting value is too far away from the mean value of the distribution, but after the burn-in the chain will converge. So, if it is possible to choose a starting value in a good region, one should do that to avoid the burn-in. Otherwise, if one does not know how to choose the starting value, it is not a big problem because the chain will still converge. Then one should just identify the burn-in steps and cut the sampled values by this number of steps.

B.1.2 Ensemble Sampler

In this subsection, we introduce MCMC ensemble sampling. This sampling method was proposed by Goodman and Weare in 2010 [39]. The idea of ensemble sampling is that one state in the chain does not consist of one point X . Instead, one state consists of an ensemble of points (X_1, \dots, X_k) . The different chains are called walker. Combining the properties of ensemble sampling with the properties of MCMC sampling gives us the opportunity to use more than one point for the proposed step. This can be an advantage, if one wants to sample multidimensional distributions. If the distribution has d dimensions, one sampled point X consists of d variables $X = (x_1, x_2, \dots, x_d)$. Therefore, if one wants to use basic MCMC sampling, as explained in the previous section, where a small perturbation δ is added to X for the proposed step, δ also has to be d dimensional, as well as the distribution δ is sampled from. We saw in the previous section that the distribution used to sample δ has a tuning parameter. For d dimensions, this distribution will have d tuning parameters. Thus, it will take longer to find the best set of tuning parameters, because one has to do this for each dimension. In this case, the different variables of X are treated independently of each other. This also can cause problems, because the variables can be correlated. For example, if we

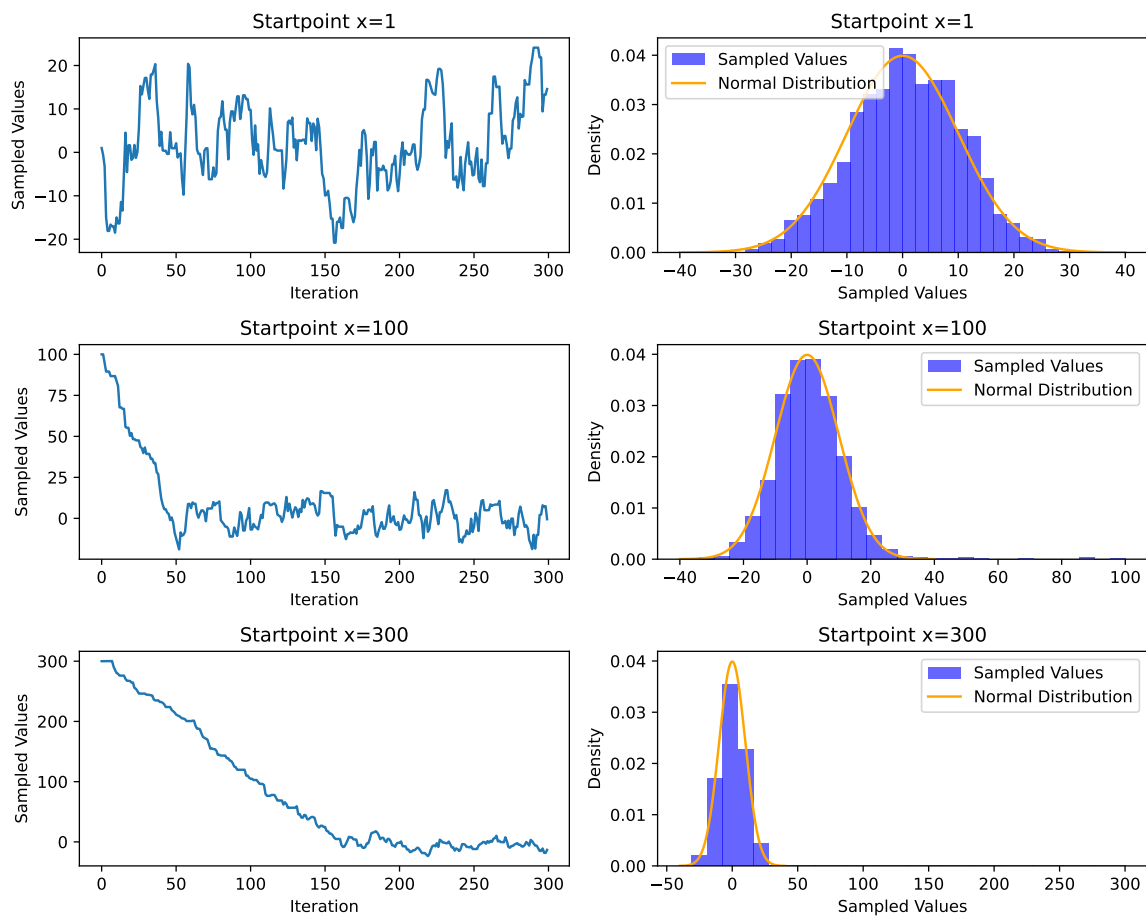


Figure B.3: The evolution of the Markov-Chain for the first 300 steps (left) and the density of the sampled values (right) for different starting values

want to sample the point of a circle with radius r , the two variables $X = (x, y)$ have to satisfy the condition

$$x^2 + y^2 < r^2 \quad (\text{B.4})$$

If x is almost as large as r , y has to be small to satisfy the condition, and vice versa. This means that the sampling process can become more efficient if the variables are not treated independently, which can be done if more points are taken into account for the proposed step. There are many different ways to propose a new step in ensemble sampling. In our sampling process, we use two different methods, the so-called Stretch Move and DE-Move.

The stretch move was also proposed by Goodman and Weare [39]. If the proposed step for walker i at position X_i is done by the Stretch Move, another walker j at position X_j has to be chosen randomly. After that, walker i is moved in the direction of walker j by a stretch factor z .

$$X'_i = X_i + z(X_j - X_i) \quad (\text{B.5})$$

The stretch factor z is chosen from a distribution $g(z)$ with

$$g(z) \propto \begin{cases} \frac{1}{\sqrt{z}} & \text{if } z \in \left[\frac{1}{a}, a\right] \\ 0 & \text{otherwise} \end{cases} \quad (\text{B.6})$$

Here a is the so-called stretching parameter, which is a tuning parameter in this case. The acceptance probability is given by

$$p(X'_i|X_i) = \min\left(1, z^{d-1} \frac{p(X'_i)}{p(X_i)}\right) \quad (\text{B.7})$$

The DE-Move uses differential evolution for the proposal step. The first approach to using differential evolution in the MCMC context was taken by ter Braak in 2006 [63]. The idea of this method is to use the difference between two walker to propose the next step for another walker. If one wants to propose a step for walker i at position X_i by the DE-Move, two other walker j and k at positions X_j and X_k have to be chosen randomly. Then the proposal step X'_i for walker i is calculated by

$$X'_i = X_i + \gamma(X_j - X_k) + \epsilon \quad (\text{B.8})$$

Here, γ is the scale factor and ϵ is a small perturbation. These are the tuning parameters of the DE-Move. The optimal choice for γ is $\gamma = \frac{2.38}{\sqrt{2d}}$, which is recommended by [63]. Typically ϵ

is drawn from a d dimensional distribution with a small variance. The acceptance probability is given by

$$p(X'_i|X_i) = \min\left(1, \frac{p(X'_i)}{p(X_i)}\right) \quad (\text{B.9})$$

The DE-Move works very well if the distribution we want to sample is highly multimodal and correlated.

In our parameter scan, we implement the ensemble sampler using the Python package `emcee` [38]. In this package, it is possible to use different moves. This means that we can allocate probabilities to different moves, and then one move is used with a certain probability for the proposal step. In our parameter scan for the KNT-Model, we use the Stretch Move with a probability of 65 % and the DE-Move with a probability of 35 %.

For the numerical implementation of the ensemble sampler, we use the Python package `emcee` [38]. Now we want to show some properties of ensemble sampling and the explained moves. Therefore, we use the example already mentioned. We want to sample the points $X = (x, y)$ of a circle with radius $r = 1$. As a posterior distribution $p(x, y)$ we use

$$p(x, y) = \begin{cases} 1 & \text{if } x^2 + y^2 < 1 \\ 0 & \text{otherwise} \end{cases} \quad (\text{B.10})$$

This means that all points inside the circle receive a probability of 1 and all points outside receive a probability of 0. Since all points inside the circle receive the same probability, the sampled point should spread homogeneously around the circle. The structure of the posterior causes some consequences for the chain. One consequence is that the chain has to start at a point that is already inside the circle. Otherwise, the posterior would be 0 at the beginning of the chain and the acceptance probability cannot be calculated because there one has to divide by the posterior of the starting point. However, after choosing a possible starting point, the movement of the chain is very simple. If a proposed step moves the chain outside the circle, the step is not accepted. Otherwise, if the proposed step is inside the circle, it is definitely accepted. This example is also a good model for our parameter scan for the KNT-Model, because there we also want to find the points, which satisfy some constraints. Therefore, it makes sense to define the posterior in such a way that all points which satisfy the constraints are accepted and all other points are neglected. Thus, the posterior has the same structure as the one in equation B.10 with the difference that its dimension is higher and that more than one constraint has to be satisfied. Returning to our example, we first have to choose a suitable starting point. In this example, we choose the center of the circle $X_0 = (0, 0)$ and for the starting ensemble, we choose random points in the neighborhood of the starting point,

because the walker have to start at different points. Otherwise, they would not move because the proposal steps are based on the difference between walkers. Here, we choose the starting region so that the coordinates of every walker differ by a maximum of 10^{-8} from the starting point.

First, we want to analyze the behavior of the sampling process throughout different amounts of iteration steps. Therefore, we sampled the circle with 10 walker for different numbers of steps for the Stretch Move and the DE-Move. The results are shown in figure B.4. The first observation is that the sampling results improve if the sampling process takes more steps because then more points can be sampled. This leads to the conclusion that we have to be careful with the number of steps because if this number is too small, the ensemble does not have the opportunity to sample the whole parameter space, which can be seen for the examples with 100 steps. Another observation is that the starting region is very dense in the plots. This can be observed very well in the plots for 100 and 200 steps. The explanation for this behavior is that the ensemble starts in a small area around the starting point. Thus, the differences between the walker are very small. This causes small proposal steps because the Stretch Move as well as the DE-Move use difference between walker to propose the next step. This is why the ensemble stays near the starting point at the beginning of the sampling process and the starting region is overrepresented. This means that the ensemble needs some time to spread out from the starting region. Nevertheless, this behavior is different for the Stretch Move and the DE-Move. Regarding the plots for the Stretch Move, one can observe the high density of the starting region in every plot except the plot for 1000 steps because there the density is very high almost everywhere. Additionally, it seems that the Stretch Move favors one direction in the parameter space before spreading out on the whole space because one can observe lines of high density in the plots. Comparing the plots for the DE-Move to the ones for the Stretch Move, we observe that the DE-Move spreads out from the starting region faster because there the starting region appears less dense than in the plots for the Stretch Move and it seems that the ensemble reaches out to the full circle earlier. This can be observed in the plots for 100 steps. While the plot for the Stretch Move shows some area with no or few points, the plot for the DE-Move almost shows a homogeneous distribution of points throughout the whole circle with a small dense area around the starting point. Furthermore, it seems that the DE-Move does not favor one direction because the points spread out into all directions right from the beginning.

In the next step, we want to analyze the influence of the number of walker on the sampling process. Therefore, we sampled the circle again with 500 steps and a different number of walker. The results are shown in figure B.5. The results show that the sampling results improve after using more walker. This is expected because the more walker that are used,

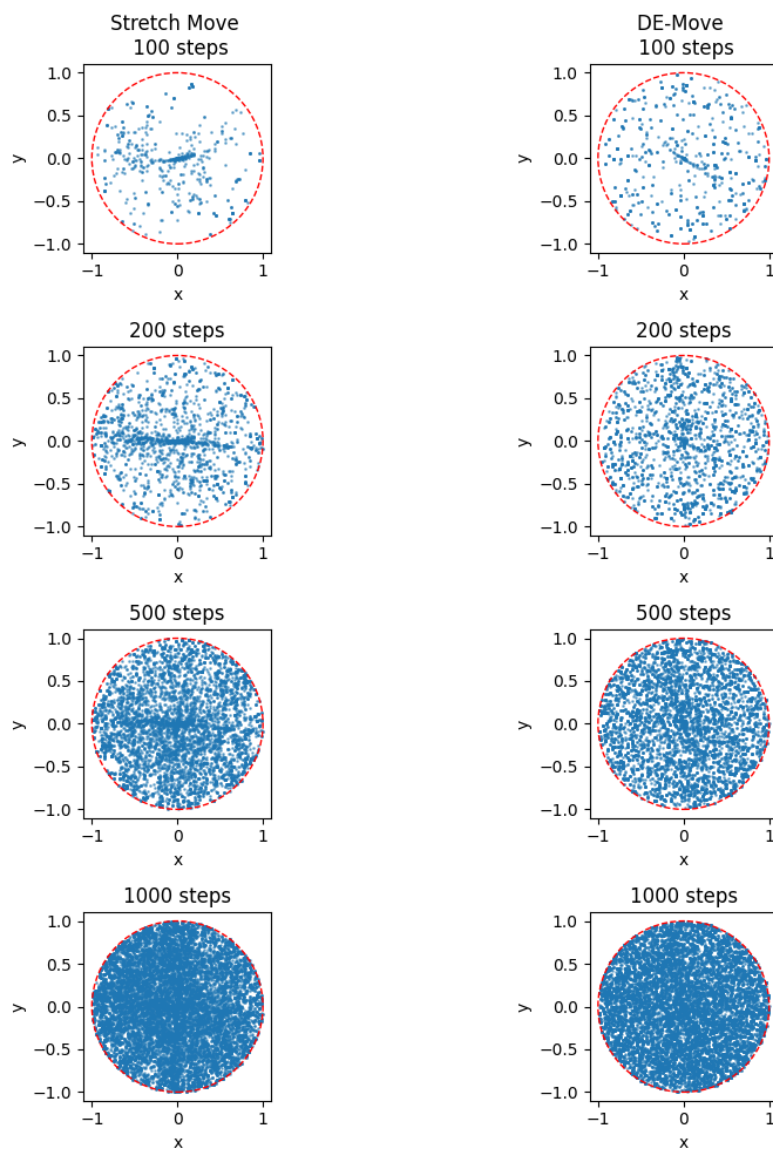


Figure B.4: Sampling results for the sampling of a circle with different number of steps

the more points are sampled and the points better represent the full circle. One also can observe that the points spread out from the starting region faster if more walker are used. This behavior can be observed very well by looking at the plots for the Stretch Move. In the plots for 5 and 10 walker, one clearly sees the dense starting region and a dense line, which is the favored direction of the ensemble at the beginning. These things cannot be observed in the plots for 15 and 20 walker. In these cases, the spread-out process has improved. However, we can still observe the differences between the two moves as before. We still observe that the results for the DE-Move are more homogeneous spread than the results for the Stretch Move. We can conclude that the sampling process improves if more walker are used, but we have to be careful with the number of walker because an increasing number of walker leads to an increasing computation time.

At least we want to analyze the effect of the tuning parameters on the sampling process. Therefore, we sampled the circle for 500 steps and used 10 walker. We used different stretch parameters a for the Stretch Move and different scaling factors γ for the DE-Move. The results for the Stretch Move are shown in figure B.6 and the results for the DE-Move are shown in figure B.7. For the Stretch Move we observe that the spread-out process from the starting region is faster if we use a larger stretching parameter because then the proposed steps are larger. For example, for $a = 1.5$ and $a = 2$ one can observe the typical dense line, and for $a = 10$ the points spread almost homogeneously around the circle. However, for $a = 100$, we see that the points also spread homogeneously, but the plot shows fewer points than the other plots. The reason for this is that large stretching parameters can lead to large proposal steps. As a consequence, it is very likely that the proposed point is outside the circle and neglected in the sampling process. The same behavior can be observed for the DE-Move with different scale factor γ . In figure B.7, we observe that the spread-out process improves for larger scale parameters because of larger proposed steps. Furthermore, we also see that the scale parameter can be too large, which can be observed in the plot for $\gamma = 5$ because this plot has fewer points than the other plots. The explanation is the same as for the Stretch Move. If the scale parameter is too large, the proposed steps are outside the circle and neglected. This leads to the conclusion that we have to be careful with the stretching parameter and the scale parameter because if they are too small, the spread-out process takes too long, but if they are too large, the proposed steps are too large. In practice, it is even better to choose these parameters a little bit too small than too large because then it is still possible to take the sampling results after the spread-out process is done. This means that the sampled points at the beginning are neglected. This strategy is similar to the burn-in phase.

Thus, it is a good strategy to neglect the first iteration steps to avoid a high density in the

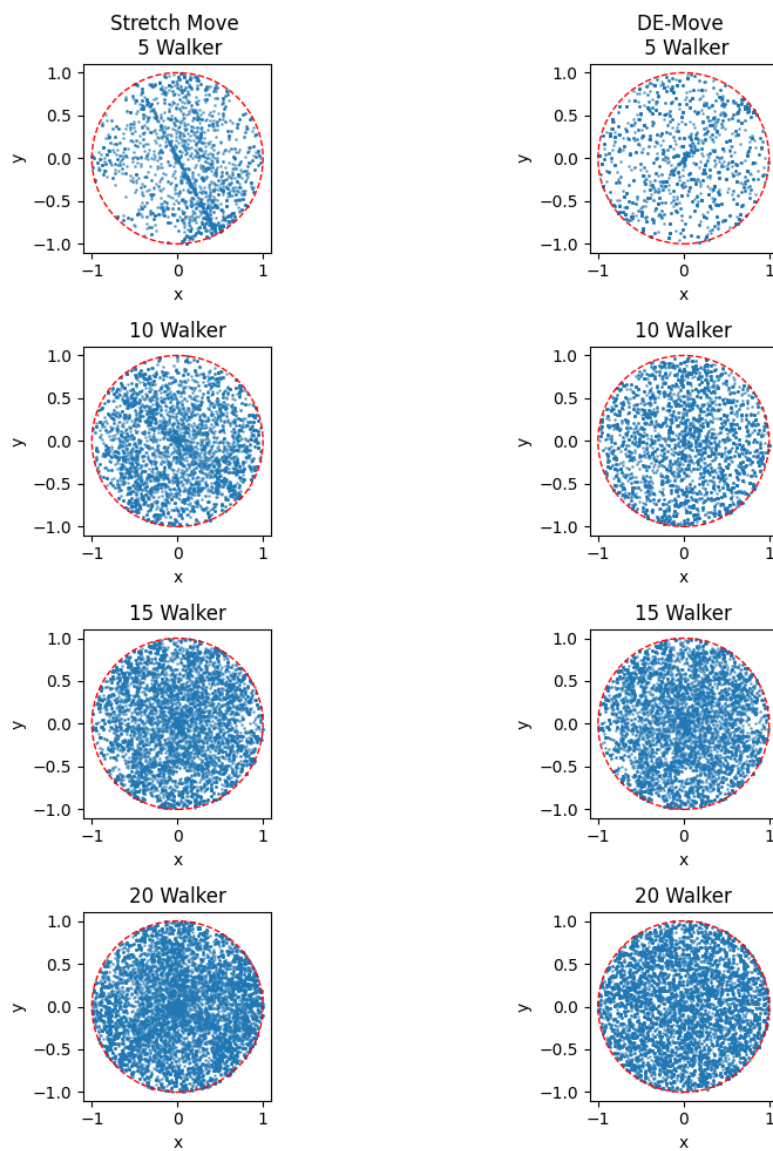


Figure B.5: Sampling results for the sampling of a circle with different number of walker

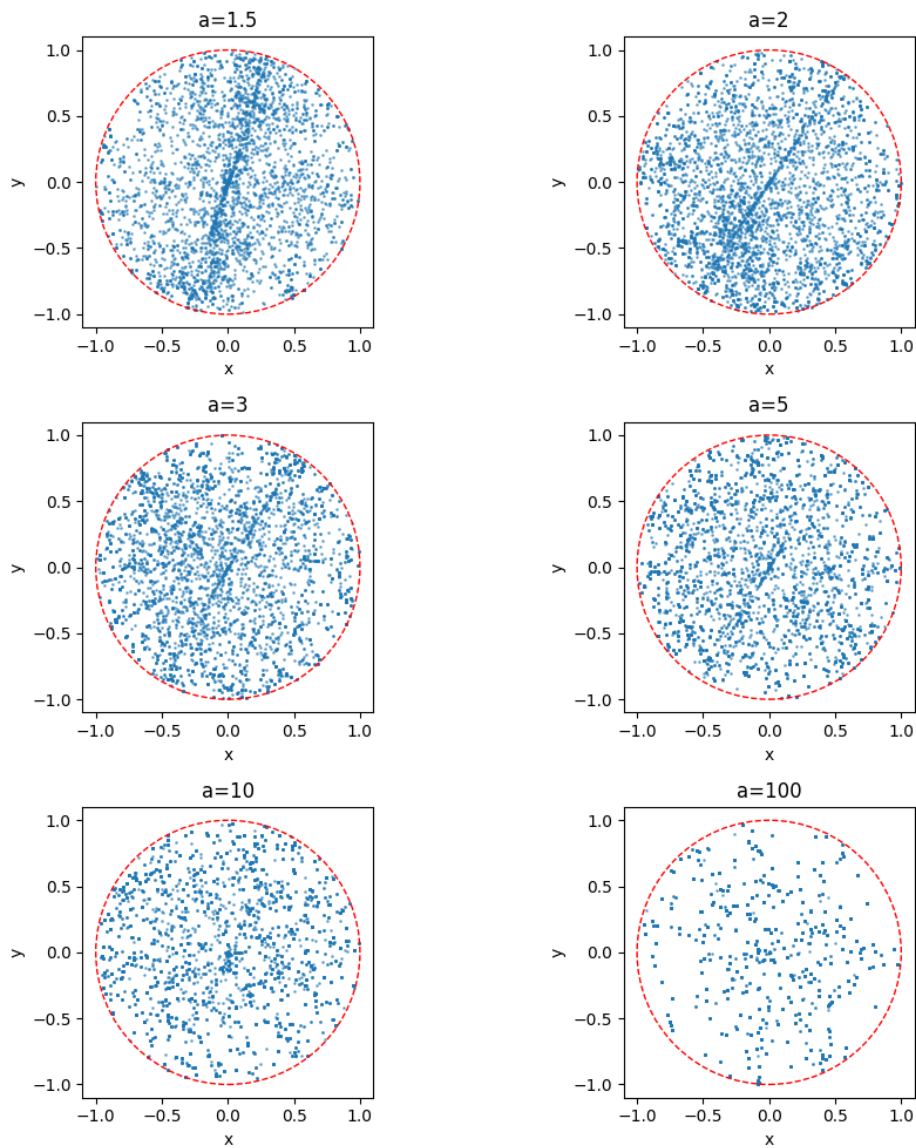


Figure B.6: Sampling results for a circle sampled with the Stretch Move with different stretch parameter

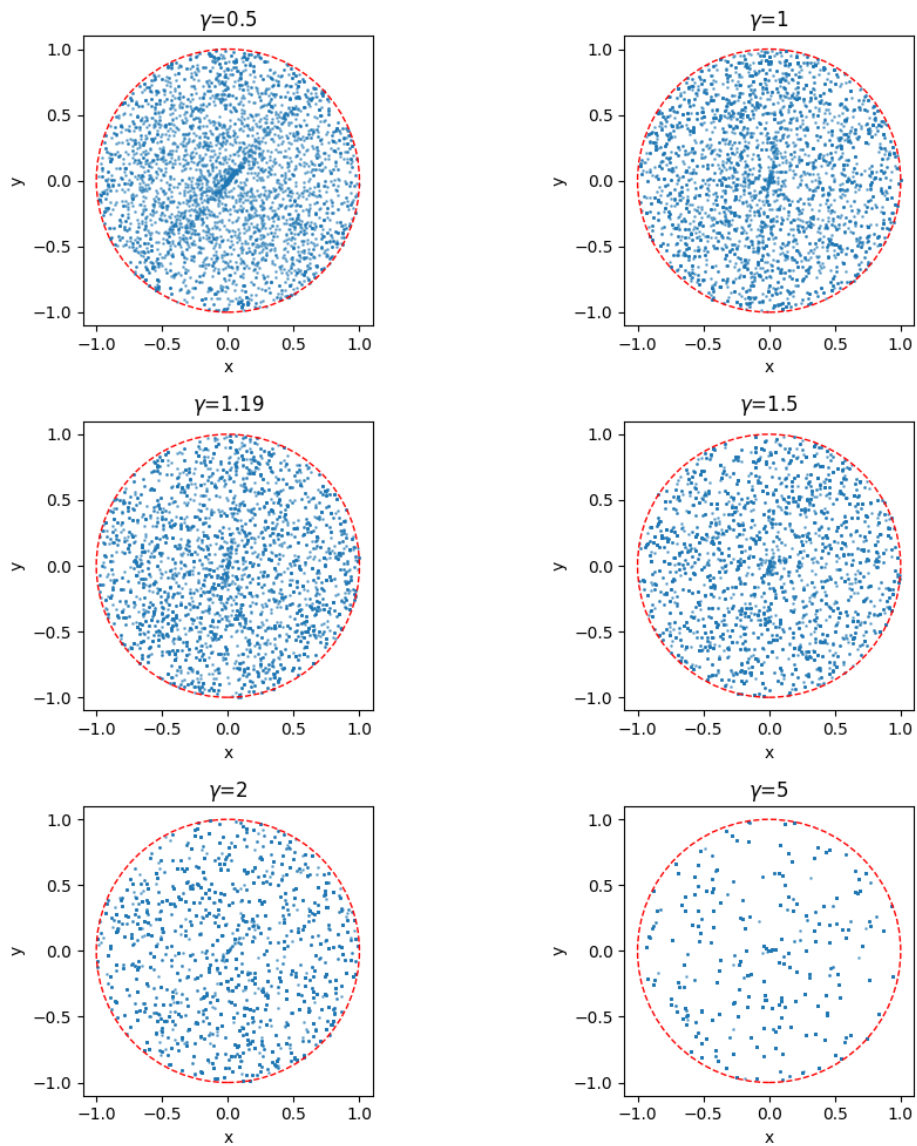


Figure B.7: Sampling results for a circle sampled with the DE-Move with different scale parameter

starting region. Nevertheless, it is very hard to determine, when the spread-out process is done, if the parameter space is high dimensional, for example the parameter space of the KNT-Model has 28 dimensions. Furthermore, since the states of the chain depend on the previous state, the states are not independent from each other and can be correlated. Therefore, we have to find a strategy how we could analyze the sampling results statistically, even if the starting region is very dense and the states in the chain are correlated. This strategy is explained in the next section, but before explaining the strategy we want to demonstrate the problem with our example. Therefore, we did a scan with 10 walker for 500 steps. The results are shown in figure B.8. In the left plot, the sampled points are shown. There we observe that the points almost spread homogeneously around the circle and the starting region appears a little bit more dense, but this is barely observable. Here, we also do further analysis of the sampling results to investigate the influence of the dense starting region. Therefore, we calculate the mean radius \bar{r} of the sampling results and investigate the distribution of points depending on the radius and compared the results with those theoretically expected. The expected density for a homogeneous circle depending on x and y is $\rho(x, y) = \frac{1}{A}$ with the area $A = \pi R^2$ of a circle. Hence, we can set $R = 1$ in our case. If we want to calculate the density in dependence of the radius r , we have to integrate the angle. Therefore, we get for the density depending on the radius

$$\rho(r) = \int_0^{2\pi} \frac{1}{\pi} r d\phi = 2r \quad (\text{B.11})$$

Using this density, we are also able to calculate the expected mean radius \bar{r}

$$\bar{r} = \int_0^1 r \rho(r) dr = \frac{2}{3} \quad (\text{B.12})$$

In the right plot of figure B.8, we show the density of our sampling results and the expected density. There, we see that the data match the expected density pretty well, except for small r , which is the starting region. The density of the points in that region is higher than expected. Thus, the influence of the starting region is observable in this analysis, even if it seems that the points in the left plot spread almost homogeneously. This influence can be seen in the calculation of \bar{r} because for the sampled points we get $\bar{r} = 0.6209$. This result is less than expected, and the reason could be that we have more points than expected with a small r . This result confirms that another strategy is needed to analyze the results.

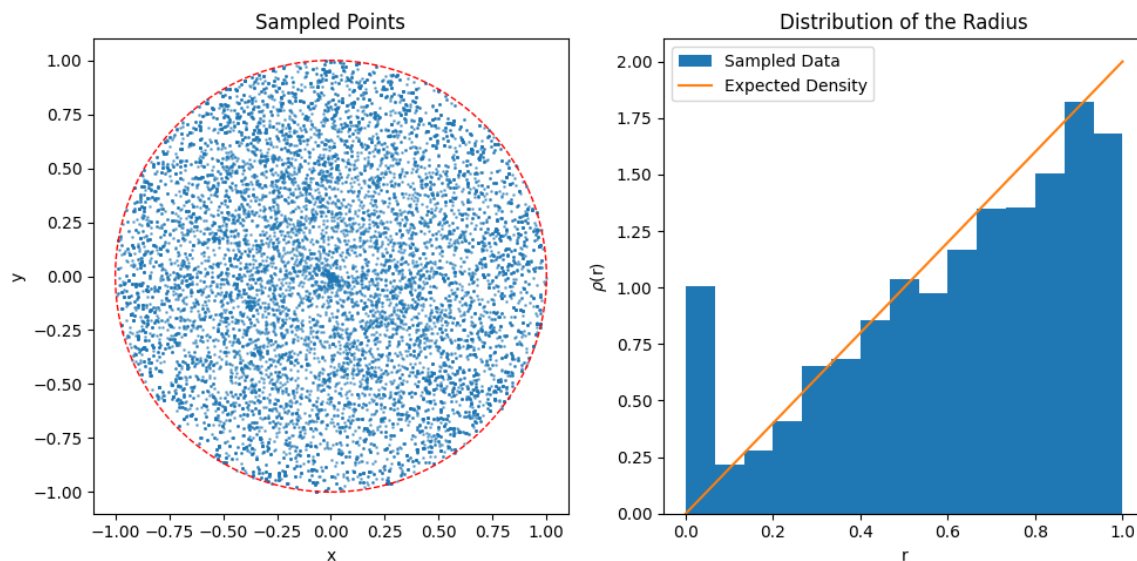


Figure B.8: Sampling results for the circle (left) and the density of points depending on the radius (right)

B.2 Importance Sampling

In our case, the density of points should be homogeneous as explained in the previous chapter, but due to the choice of a starting region and correlations they are not. Therefore, the real distribution of the points does not match the expected distribution, which leads to misleading statistics. This problem can be solved by using importance sampling. This method is explained in this subsection based on [[64], Chapter 29.2]. The idea of importance sampling is to reweight the data if it does not show the expected distribution. For example, if the data should be distributed in the shape of a distribution $p(x)$, the mean value of an observable is calculated by

$$\bar{f} = \int f(x)p(x)dx \quad (\text{B.13})$$

Now we consider the case where the data is distributed in the shape of another distribution $q(x)$ instead of $p(x)$. Then it is still possible to calculate the mean value of an observable f , if we weight the data with a factor $w(x) = \frac{p(x)}{q(x)}$ and the mean value is calculated by

$$\bar{f} = \int f(x)p(x)dx = \int f(x)w(x)q(x)dx \quad (\text{B.14})$$

Thus, we need to know the distributions $p(x)$ and $q(x)$ to weight the data and perform the statistical analysis. In our case, the expected distribution should be homogeneous. Therefore, $p(x)$ is constant. According to that, we just need to determine the real distribution of the

data $q(x)$. Therefore, we have to estimate the density of the points, which we do by using a method called normalizing flows. This is explained in the next section.

B.3 Normalizing Flows

Normalizing Flows can be used to estimate the density of a dataset. The basic knowledge of this method is given in this section. It is based on [65]. The main idea of flow-based models is to express a data point x as a transformation T of a point u which is sampled from a distribution $p_u(u)$

$$x = T(u) \tag{B.15}$$

The flow-based model takes a base distribution $p_u(u)$ and tries to find a transformation T , which transforms the points sampled from p_u into the data. The transformation and the base distribution can have parameters of their own, which induces a family of distributions over the data x parametrized by these parameters $\{\phi, \psi\}$. Transformation T has to be a diffeomorphism. This means that T is invertible and T , as well as inversion T^{-1} are differentiable. If this is the case, the distribution of the data $p_x(x)$ can be calculated by change of variables

$$p_x(x) = p_u(u) |\det J_T(u)|^{-1} \tag{B.16}$$

This can also be written in terms of x using $u = T^{-1}(x)$

$$p_x(x) = p_u(T^{-1}(x)) |\det J_{T^{-1}}(x)| \tag{B.17}$$

Here, J_T is the Jacobian of T given by

$$J_T(u) = \begin{bmatrix} \frac{\partial T_1}{\partial u_1} & \dots & \frac{\partial T_1}{\partial u_D} \\ \vdots & \ddots & \vdots \\ \frac{\partial T_D}{\partial u_1} & \dots & \frac{\partial T_D}{\partial u_D} \end{bmatrix} \tag{B.18}$$

Here, D is the number of dimensions of the data. An important property of diffeomorphisms is that the composition of diffeomorphisms is also a diffeomorphism. Thus, we are able to construct T as a chain of n transformations

$$T = T_1 \circ T_2 \circ \dots \circ T_n \tag{B.19}$$

This means that it is possible to construct a complex transformation as a chain of many simpler transformations. In this case, the Jacobian is given by

$$\det J_T(u) = \det J_{T_1}(u) \cdot \det J_{T_2}(u) \cdot \dots \cdot \det J_{T_n}(u) \quad (\text{B.20})$$

The easiest way to construct such a flow is to use one kind of transformation and chain it multiple times. We use a transformation called Masked Autoregressive Flow (MAF) [66]. Autoregressive flows have the property that the transformation is done dimension-wise and the transformation of one dimension only depends on previous dimensions. This means that if we consider that our data x have dimension D , the transformation T_i of dimension i depends only on the previous dimensions $j < i$

$$T_i(x) = T_i(x_{j < i}) \quad (\text{B.21})$$

The advantage of this property is that our Jacobian gets a triangular structure because the differentials $\frac{\partial T_i}{\partial T_{k > i}} = 0$ vanish. In this case, it is very easy to calculate the determinant

$$\det J_T = \prod_{i=1}^D \frac{\partial T_i}{\partial x_i} \quad (\text{B.22})$$

The distribution of our data can be calculated using equation B.17. Our specific transformation (MAF) has the following structure

$$y_i = T_i(x) = x_i \cdot \exp(s_i) + t_i \quad (\text{B.23})$$

Here, s_i and t_i are functions that depend on $x_{j < i}$. Thus, the transformation scales a variable x_i with a scale factor $\exp(s_i)$ and shifts it by t_i . The functions s_i and t_i are determined by neural networks throughout the normalizing flow process.

We use the package nflows [67] for our normalizing flow application. This is a comprehensive collection of normalizing flows using PyTorch [68]. The training process to estimate the density of our points is structured as follows. First, we have to choose a base distribution $p_u(u)$. Usually a normal distribution is chosen. Then we have to choose a number of layers. This defines how many transformation steps are done. The complete transformation T is then determined by the neural networks. After that, our data is transformed by the inverse transformation T^{-1} to get the positions of our data in the base distribution. In the next step, the logarithm of the density of our data is calculated

$$\log(p_x(x)) = \log(p_u(u)) + \log |\det J_T(u)|^{-1} \quad (\text{B.24})$$

After that, we are able to calculate the loss function \mathcal{L} , which is the average negative log-likelihood of the data

$$\mathcal{L} = -\frac{1}{N} \sum_{i=1}^N \log p_x(x^{(i)}) \quad (\text{B.25})$$

Here, N is the number of points and $x^{(i)}$ is the i -th point. The loss function measures how well the density given by the transformation of the base distribution fits the data. Therefore, the aim of the training process is to minimize the loss function. After this step, the gradients of transformation parameters are calculated and the parameters are updated. Then the whole process starts from the beginning again until the loss function is minimized.

Now we want to return to our example that we showed at the end of Section appendix B.1.2. There we saw that our sampling results did not match the expected results for the density depending on the radius and the mean radius because the starting region of the sampling was really dense, which leads to misleading statistics. Thus, we estimate the density of our data using normalizing flows and weight our data to use importance sampling. Now we can plot the density with weights taken into account. This is shown in figure B.9. In the left plot, the density without the weights is shown, and in the right plot the weights are taken into account. In addition, we plot the expected density $\rho(r) = 2r$ in both plots. We observe that the weighted density matches the expected density very well because the density for small r the weighted density is also small compared to the original density. We also calculated the mean radius taking the weights into account and the result is $\bar{r} = 0.668$. This also matches the expected value $\bar{r} = \frac{2}{3}$ compared to the original result $\bar{r} = 0.6209$. This leads to the conclusion that importance sampling actually improves the results of our sampling process.

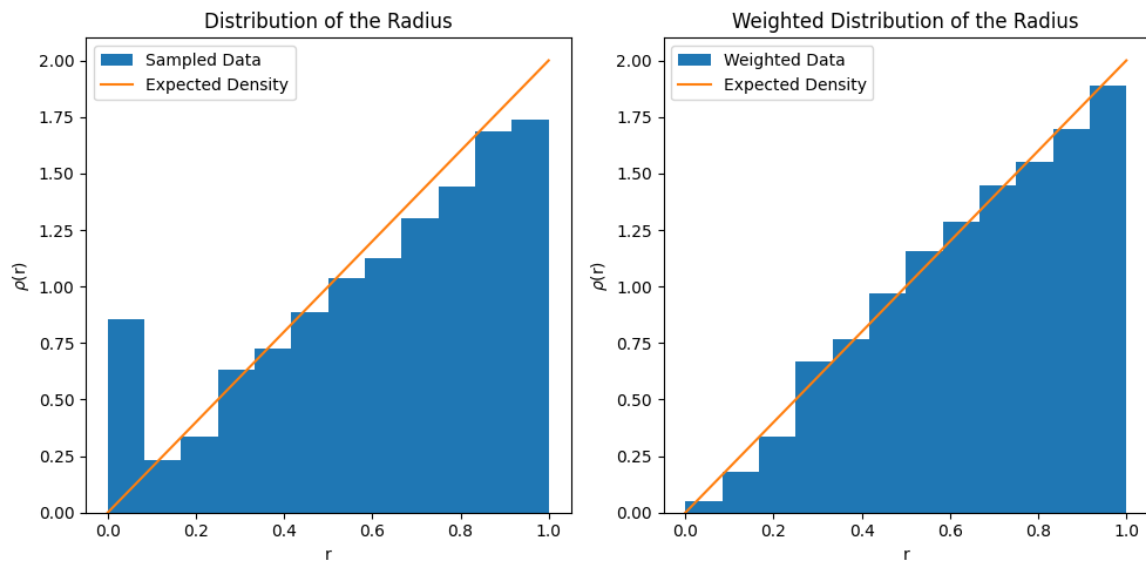


Figure B.9: Density of the sampled points of the circle depending on the radius with not taking the weights into account (left) and taking the weights into account (right)

C RGEs of the Scotogenic Model

In the following section, we give the 1-loop RGEs for the Scotogenic Model. We derived these equations with the help of SARAH [41] and compared them with [69]. We write down the RGEs in terms of the beta functions, which are defined as

$$\beta_g = 16\pi^2 \mu \frac{dg}{d\mu} \quad (\text{C.1})$$

In the following equations, we are using the short-hand notations

$$T = \text{Tr}(Y_e^\dagger Y_e + 3Y_u^\dagger Y_u + 3Y_d^\dagger Y_d) \quad (\text{C.2})$$

$$T_y = \text{Tr}(y^\dagger y) \quad (\text{C.3})$$

$$T_4 = \text{Tr}(Y_e^\dagger Y_e Y_e^\dagger Y_e + 3Y_u^\dagger Y_u Y_u^\dagger Y_u + 3Y_d^\dagger Y_d Y_d^\dagger Y_d) \quad (\text{C.4})$$

$$T_{4y} = \text{Tr}(y^\dagger y y^\dagger y) \quad (\text{C.5})$$

$$T_{ye} = \text{Tr}(y^\dagger y Y_e^\dagger Y_e) \quad (\text{C.6})$$

C.1 Gauge couplings

$$\beta_{g_1} = 7g_1^3 \quad (\text{C.7})$$

$$\beta_{g_2} = -3g_2^3 \quad (\text{C.8})$$

$$\beta_{g_3} = -7g_3^3 \quad (\text{C.9})$$

C.2 Yukawa couplings

$$\beta_{Y_u} = Y_u \left\{ \frac{3}{2}(Y_u^\dagger Y_u - Y_d^\dagger Y_d) + T - \frac{17}{12}g_1^2 - \frac{9}{4}g_2^2 - 8g_3^2 \right\} \quad (\text{C.10})$$

$$\beta_{Y_d} = Y_d \left\{ \frac{3}{2}(Y_d^\dagger Y_d - Y_u^\dagger Y_u) + T - \frac{5}{12}g_1^2 - \frac{9}{4}g_2^2 - 8g_3^2 \right\} \quad (\text{C.11})$$

$$\beta_{Y_e} = Y_e \left\{ \frac{3}{2}Y_e^\dagger Y_e + \frac{1}{2}y^\dagger y + T - \frac{15}{4}g_1^2 - \frac{9}{4}g_2^2 \right\} \quad (\text{C.12})$$

$$\beta_Y = Y \left\{ \frac{3}{2}y^\dagger y + \frac{1}{2}Y_e^\dagger Y_e + T_y - \frac{3}{4}g_1^2 - \frac{9}{4}g_2^2 \right\} \quad (\text{C.13})$$

C.3 Quartic scalar couplings

$$\beta_{\lambda_1} = 12\lambda_1^2 + 4\lambda_3^2 + 4\lambda_3\lambda_4 + 2\lambda_4^2 + 2\lambda_5^2 + \frac{3}{4}(g_1^4 + 3g_2^4 + 2g_1^2g_2^2) - 3\lambda_1 \left[g_1^2 + 3g_2^2 - \frac{4}{3}T \right] - 4T_4 \quad (\text{C.14})$$

$$\beta_{\lambda_2} = 12\lambda_2^2 + 4\lambda_3^2 + 4\lambda_3\lambda_4 + 2\lambda_4^2 + 2\lambda_5^2 + \frac{3}{4}(g_1^4 + 3g_2^4 + 2g_1^2g_2^2) - 3\lambda_2 \left[g_1^2 + 3g_2^2 - \frac{4}{3}T_y \right] - 4T_{4y} \quad (\text{C.15})$$

$$\beta_{\lambda_3} = (\lambda_1 + \lambda_2)(6\lambda_3 + 2\lambda_4) + 4\lambda_3^2 + 2\lambda_4^2 + 2\lambda_5^2 + \frac{3}{4}(g_1^4 + 3g_2^4 - 2g_1^2g_2^2) - 3\lambda_3 \left[g_1^2 + 3g_2^2 - \frac{4}{3}(T_y + T) \right] - 4T_{ye} \quad (\text{C.16})$$

$$\beta_{\lambda_4} = 2(\lambda_1 + \lambda_2)\lambda_4 + 8\lambda_3\lambda_4 + 4\lambda_4^2 + 8\lambda_5^2 + 3g_1^2g_2^2 - 3\lambda_4 \left[g_1^2 + 3g_2^2 - \frac{2}{3}(T_y + T) \right] - 4T_{ye} \quad (\text{C.17})$$

$$\beta_{\lambda_5} = 2(\lambda_1 + \lambda_2)\lambda_5 + 8\lambda_3\lambda_5 + 12\lambda_4\lambda_5 - 3\lambda_5 \left[g_1^2 + 3g_2^2 - \frac{2}{3}(T_y + T) \right] \quad (\text{C.18})$$

D RGEs of the KNT-Model

In the following section, the 1-loop RGEs for the KNT-Model are given. These equations are also derived by SARAH[41]. We write down the RGEs in terms of the beta functions, which are defined as

$$\beta_g = 16\pi^2 \mu \frac{dg}{d\mu} \quad (\text{D.1})$$

We use the following short-hand notations

$$T = \text{Tr}(Y_e^\dagger Y_e + 3Y_u^\dagger Y_u + 3Y_d^\dagger Y_d) \quad (\text{D.2})$$

$$T_{\tilde{Y}} = \text{Tr}(\tilde{Y}^\dagger \tilde{Y}) \quad (\text{D.3})$$

$$T_Y = \text{Tr}(Y Y^\dagger) \quad (\text{D.4})$$

$$T_4 = \text{Tr}(Y_e^\dagger Y_e Y_e^\dagger Y_e + 3Y_u^\dagger Y_u Y_u^\dagger Y_u + 3Y_d^\dagger Y_d Y_d^\dagger Y_d) \quad (\text{D.5})$$

$$T_{4\tilde{Y}} = \text{Tr}(\tilde{Y}^\dagger \tilde{Y} \tilde{Y}^\dagger \tilde{Y}) \quad (\text{D.6})$$

$$T_{4Y} = \text{Tr}(Y Y^\dagger Y Y^\dagger) \quad (\text{D.7})$$

$$T_{\tilde{Y}e} = \text{Tr}(\tilde{Y}^\dagger \tilde{Y} Y_e^\dagger Y_e) \quad (\text{D.8})$$

$$T_{Ye} = \text{Tr}(Y^\dagger Y Y_e^\dagger Y_e) \quad (\text{D.9})$$

D.1 Gauge couplings

$$\beta_{g_1} = \frac{15}{2} g_1^3 \quad (\text{D.10})$$

$$\beta_{g_2} = -\frac{19}{6} g_2^3 \quad (\text{D.11})$$

$$\beta_{g_3} = -7 g_3^3 \quad (\text{D.12})$$

D.2 Yukawa coupling

$$\beta_{Y_u} = Y_u \left(\frac{3}{2} (Y_u^\dagger Y_u - Y_d^\dagger Y_d) + T - \frac{17}{12} g_1^2 - \frac{9}{4} g_2^2 - 8g_3^2 \right) \quad (\text{D.13})$$

$$\beta_{Y_d} = Y_d \left(\frac{3}{2} (Y_d^\dagger Y_d - Y_u^\dagger Y_u) + T - \frac{5}{12} g_1^2 - \frac{9}{4} g_2^2 - 8g_3^2 \right) \quad (\text{D.14})$$

$$\beta_{Y_e} = Y_e \left(\frac{3}{2} Y_e^\dagger Y_e - 2\tilde{Y}^\dagger \tilde{Y} \right) + \frac{1}{2} Y Y^\dagger Y_e + Y_e \left(T - \frac{15}{4} g_1^2 - \frac{9}{4} g_2^2 \right) \quad (\text{D.15})$$

$$\beta_{\tilde{Y}} = \tilde{Y} \left(4\tilde{Y}^\dagger \tilde{Y} + \frac{1}{2} Y_e^\dagger Y_e \right) + \frac{1}{2} Y_e^T Y_e^* \tilde{Y} + \tilde{Y} \left(4T_{\tilde{Y}} - \frac{3}{2} g_1^2 - \frac{9}{2} g_2^2 \right) \quad (\text{D.16})$$

$$\beta_Y = Y Y^\dagger Y + Y_e Y_e^\dagger Y + Y \left(T_Y - \frac{9}{5} g_2^2 \right) \quad (\text{D.17})$$

D.3 Quartic scalar couplings

$$\begin{aligned} \beta_{\lambda_H} &= 12\lambda_H^2 + 2\lambda_{HS_1}^2 + 2\lambda_{HS_2}^2 + \frac{3}{4} \left(g_1^4 + 2g_1^2 g_2^2 + 3g_2^4 \right) \\ &\quad + \lambda_H \left(4T - 3(g_1^2 + 3g_2^2) \right) - 4T_4 \end{aligned} \quad (\text{D.18})$$

$$\beta_{\lambda_{S_1}} = 10\lambda_{S_1}^2 + 4\lambda_{HS_1}^2 + 2\lambda_{S_1 S_2}^2 + 2|\lambda'_{S_1 S_2}|^2 + 12g_1^4 + \lambda_{S_1} \left(16T_{\tilde{Y}} - 12g_1^2 \right) - 64T_{4\tilde{Y}} \quad (\text{D.19})$$

$$\beta_{\lambda_{S_2}} = 10\lambda_{S_2}^2 + 4\lambda_{HS_2}^2 + 2\lambda_{S_1 S_2}^2 + 2|\lambda'_{S_1 S_2}|^2 + 12g_1^4 + \lambda_{S_2} \left(4T_Y - 12g_1^2 \right) - 4T_{4Y} \quad (\text{D.20})$$

$$\begin{aligned} \beta_{\lambda_{HS_1}} &= 4\lambda_{HS_1}^2 + 6\lambda_H \lambda_{HS_1} + 4\lambda_{S_1} \lambda_{HS_1} + 2\lambda_{S_1 S_2} \lambda_{HS_2} + 3g_1^4 \\ &\quad + \lambda_{HS_1} \left(2T + 8T_{\tilde{Y}} - \frac{3}{2} (5g_1^2 + 3g_2^2) \right) - 16T_{\tilde{Y}e} \end{aligned} \quad (\text{D.21})$$

$$\begin{aligned} \beta_{\lambda_{HS_2}} &= 4\lambda_{HS_2}^2 + 6\lambda_H \lambda_{HS_2} + 4\lambda_{S_2} \lambda_{HS_2} + 2\lambda_{S_1 S_2} \lambda_{HS_1} + 3g_1^4 \\ &\quad + \lambda_{HS_2} \left(2T + 2T_Y - \frac{3}{2} (5g_1^2 + 3g_2^2) \right) - 16T_{Ye} \end{aligned} \quad (\text{D.22})$$

$$\begin{aligned} \beta_{\lambda_{S_1 S_2}} &= 4\lambda_{S_1 S_2}^2 + 4\lambda_{S_1} \lambda_{S_1 S_2} + 4\lambda_{S_2} \lambda_{S_1 S_2} + 4\lambda_{HS_1} \lambda_{HS_2} + 8|\lambda'_{S_1 S_2}|^2 + 12g_1^4 \\ &\quad + \lambda_{S_1 S_2} \left(8T_{\tilde{Y}} + 2T_Y - 12g_1^2 \right) \end{aligned} \quad (\text{D.23})$$

$$\beta_{\lambda'_{S_1 S_2}} = \lambda'_{S_1 S_2} \left(2\lambda_{S_1} + 2\lambda_{S_2} + 8\lambda_{S_1 S_2} + 8T_{\tilde{Y}} + 2T_Y - 12g_1^2 \right) \quad (\text{D.24})$$

Bibliography

- [1] Georges Aad et al. “Observation of a new particle in the search for the Standard Model Higgs boson with the ATLAS detector at the LHC”. In: *Phys. Lett. B* 716 (2012), pp. 1–29. DOI: 10.1016/j.physletb.2012.08.020. arXiv: 1207.7214 [hep-ex].
- [2] Serguei Chatrchyan et al. “Observation of a New Boson at a Mass of 125 GeV with the CMS Experiment at the LHC”. In: *Phys. Lett. B* 716 (2012), pp. 30–61. DOI: 10.1016/j.physletb.2012.08.021. arXiv: 1207.7235 [hep-ex].
- [3] Y. Fukuda et al. “Evidence for oscillation of atmospheric neutrinos”. In: *Phys. Rev. Lett.* 81 (1998), pp. 1562–1567. DOI: 10.1103/PhysRevLett.81.1562. arXiv: hep-ex/9807003.
- [4] Alan W. P. Poon et al. “Neutrino observations from the Sudbury Neutrino Observatory”. In: *AIP Conf. Proc.* 610.1 (2002). Ed. by E. Norman, L. Schroeder, and G. Wozniak, pp. 218–230. DOI: 10.1063/1.1469931. arXiv: nucl-ex/0110005.
- [5] Zhi-jian Tao. “Radiative seesaw mechanism at weak scale”. In: *Phys. Rev. D* 54 (1996), pp. 5693–5697. DOI: 10.1103/PhysRevD.54.5693. arXiv: hep-ph/9603309.
- [6] Ernest Ma. “Verifiable radiative seesaw mechanism of neutrino mass and dark matter”. In: *Phys. Rev. D* 73 (2006), p. 077301. DOI: 10.1103/PhysRevD.73.077301. arXiv: hep-ph/0601225.
- [7] Lawrence M. Krauss, Salah Nasri, and Mark Trodden. “A Model for neutrino masses and dark matter”. In: *Phys. Rev. D* 67 (2003), p. 085002. DOI: 10.1103/PhysRevD.67.085002. arXiv: hep-ph/0210389.
- [8] F. Zwicky. “Die Rotverschiebung von extragalaktischen Nebeln”. In: *Helv. Phys. Acta* 6 (1933), pp. 110–127. DOI: 10.1007/s10714-008-0707-4.
- [9] Sinclair Smith. “The Mass of the Virgo Cluster”. In: 83 (Jan. 1936), p. 23. DOI: 10.1086/143697.
- [10] A. V. Zasov et al. “Dark matter in galaxies”. In: *Phys. Usp.* 60.1 (2017), pp. 3–39. DOI: 10.3367/UFNe.2016.03.037751. arXiv: 1710.10630 [astro-ph.GA].
- [11] Douglas Clowe et al. “A direct empirical proof of the existence of dark matter”. In: *Astrophys. J. Lett.* 648 (2006), pp. L109–L113. DOI: 10.1086/508162. arXiv: astro-ph/0608407.

- [12] Tim Zimmermann et al. “Dwarf Galaxies Imply Dark Matter is Heavier than 2.2×10^{-21} eV”. In: *Phys. Rev. Lett.* 134.15 (2025), p. 151001. DOI: 10.1103/PhysRevLett.134.151001. arXiv: 2405.20374 [astro-ph.CO].
- [13] Mordehai Milgrom. “Dynamics with a non-standard inertia-acceleration relation: an alternative to dark matter”. In: *Annals Phys.* 229 (1994), pp. 384–415. DOI: 10.1006/aphy.1994.1012. arXiv: astro-ph/9303012.
- [14] Marco Cirelli, Alessandro Strumia, and Jure Zupan. “Dark Matter”. In: (June 2024). arXiv: 2406.01705 [hep-ph].
- [15] Gerard Jungman, Marc Kamionkowski, and Kim Griest. “Supersymmetric dark matter”. In: *Physics Reports* 267.5 (1996), pp. 195–373. ISSN: 0370-1573. DOI: [https://doi.org/10.1016/0370-1573\(95\)00058-5](https://doi.org/10.1016/0370-1573(95)00058-5). URL: <https://www.sciencedirect.com/science/article/pii/0370157395000585>.
- [16] Ya. B. Zel’dovich and I. D. Novikov. “The Hypothesis of Cores Retarded during Expansion and the Hot Cosmological Model”. In: 10 (Feb. 1967), p. 602.
- [17] C. Alcock et al. “The MACHO Project: Microlensing Results from 5.7 Years of Large Magellanic Cloud Observations”. In: *The Astrophysical Journal* 542.1 (Oct. 2000), p. 281. DOI: 10.1086/309512. URL: <https://dx.doi.org/10.1086/309512>.
- [18] Edward Witten. “Dynamical breaking of supersymmetry”. In: *Nuclear Physics B* 188.3 (1981), pp. 513–554. ISSN: 0550-3213. DOI: [https://doi.org/10.1016/0550-3213\(81\)90006-7](https://doi.org/10.1016/0550-3213(81)90006-7). URL: <https://www.sciencedirect.com/science/article/pii/0550321381900067>.
- [19] John Preskill, Mark B. Wise, and Frank Wilczek. “Cosmology of the invisible axion”. In: *Physics Letters B* 120.1 (1983), pp. 127–132. ISSN: 0370-2693. DOI: [https://doi.org/10.1016/0370-2693\(83\)90637-8](https://doi.org/10.1016/0370-2693(83)90637-8). URL: <https://www.sciencedirect.com/science/article/pii/0370269383906378>.
- [20] John Ellis et al. “Supersymmetric relics from the big bang”. In: *Nuclear Physics B* 238.2 (1984), pp. 453–476. ISSN: 0550-3213. DOI: [https://doi.org/10.1016/0550-3213\(84\)90461-9](https://doi.org/10.1016/0550-3213(84)90461-9). URL: <https://www.sciencedirect.com/science/article/pii/0550321384904619>.
- [21] W. Busza et al. “Review of speculative ‘disaster scenarios’ at RHIC”. In: *Rev. Mod. Phys.* 72 (2000), pp. 1125–1140. DOI: 10.1103/RevModPhys.72.1125. arXiv: hep-ph/9910333.
- [22] Edward Witten. “Cosmic separation of phases”. In: *Phys. Rev. D* 30 (2 July 1984), pp. 272–285. DOI: 10.1103/PhysRevD.30.272. URL: <https://link.aps.org/doi/10.1103/PhysRevD.30.272>.

- [23] Yang Bai and Andrew J. Long. “Six Flavor Quark Matter”. In: *JHEP* 06 (2018), p. 072. DOI: 10.1007/JHEP06(2018)072. arXiv: 1804.10249 [hep-ph].
- [24] Edward W. Kolb and Richard Slansky. “Dimensional reduction in the early universe: Where have the massive particles gone?” In: *Physics Letters B* 135.5 (1984), pp. 378–382. ISSN: 0370-2693. DOI: [https://doi.org/10.1016/0370-2693\(84\)90298-3](https://doi.org/10.1016/0370-2693(84)90298-3). URL: <https://www.sciencedirect.com/science/article/pii/0370269384902983>.
- [25] Gary Steigman and Michael S. Turner. “Cosmological constraints on the properties of weakly interacting massive particles”. In: *Nuclear Physics B* 253 (1985), pp. 375–386. ISSN: 0550-3213. DOI: [https://doi.org/10.1016/0550-3213\(85\)90537-1](https://doi.org/10.1016/0550-3213(85)90537-1). URL: <https://www.sciencedirect.com/science/article/pii/0550321385905371>.
- [26] Alexey Boyarsky, Oleg Ruchayskiy, and Mikhail Shaposhnikov. “The Role of sterile neutrinos in cosmology and astrophysics”. In: *Ann. Rev. Nucl. Part. Sci.* 59 (2009), pp. 191–214. DOI: 10.1146/annurev.nucl.010909.083654. arXiv: 0901.0011 [hep-ph].
- [27] Wayne Hu, Rennan Barkana, and Andrei Gruzinov. “Cold and fuzzy dark matter”. In: *Phys. Rev. Lett.* 85 (2000), pp. 1158–1161. DOI: 10.1103/PhysRevLett.85.1158. arXiv: astro-ph/0003365.
- [28] C. Boehm and Pierre Fayet. “Scalar dark matter candidates”. In: *Nucl. Phys. B* 683 (2004), pp. 219–263. DOI: 10.1016/j.nuclphysb.2004.01.015. arXiv: hep-ph/0305261.
- [29] Martin Bauer and Tilman Plehn. *Yet Another Introduction to Dark Matter: The Particle Physics Approach*. Vol. 959. Lecture Notes in Physics. Springer, 2019. DOI: 10.1007/978-3-030-16234-4. arXiv: 1705.01987 [hep-ph].
- [30] S. Navas et al. “Review of particle physics”. In: *Phys. Rev. D* 110.3 (2024), p. 030001. DOI: 10.1103/PhysRevD.110.030001.
- [31] R. N. Cahn et al. “White Paper: Measuring the Neutrino Mass Hierarchy”. In: *Snowmass 2013: Snowmass on the Mississippi*. July 2013. arXiv: 1307.5487 [hep-ex].
- [32] KATRIN Collaboration† et al. “Direct neutrino-mass measurement based on 259 days of KATRIN data”. In: *Science* 388.6743 (2025), pp. 180–185. DOI: 10.1126/science.adq9592. eprint: <https://www.science.org/doi/pdf/10.1126/science.adq9592>. URL: <https://www.science.org/doi/abs/10.1126/science.adq9592>.
- [33] J. A. Casas and A. Ibarra. “Oscillating neutrinos and $\mu \rightarrow e, \gamma$ ”. In: *Nucl. Phys. B* 618 (2001), pp. 171–204. DOI: 10.1016/S0550-3213(01)00475-8. arXiv: hep-ph/0103065.
- [34] Asher Berlin, Dan Hooper, and Samuel D. McDermott. “Simplified Dark Matter Models for the Galactic Center Gamma-Ray Excess”. In: *Phys. Rev. D* 89.11 (2014), p. 115022. DOI: 10.1103/PhysRevD.89.115022. arXiv: 1404.0022 [hep-ph].

- [35] Kristjan Kannike. “Vacuum Stability Conditions From Copositivity Criteria”. In: *Eur. Phys. J. C* 72 (2012), p. 2093. DOI: 10.1140/epjc/s10052-012-2093-z. arXiv: 1205.3781 [hep-ph].
- [36] L. Lavoura. “General formulae for $f(1) \rightarrow f(2) \gamma$ ”. In: *Eur. Phys. J. C* 29 (2003), pp. 191–195. DOI: 10.1140/epjc/s2003-01212-7. arXiv: hep-ph/0302221.
- [37] Takashi Toma and Avelino Vicente. “Lepton Flavor Violation in the Scotogenic Model”. In: *JHEP* 01 (2014), p. 160. DOI: 10.1007/JHEP01(2014)160. arXiv: 1312.2840 [hep-ph].
- [38] Daniel Foreman-Mackey et al. “`emcee`: The MCMC Hammer”. In: *Publications of the Astronomical Society of the Pacific* 125.925 (Mar. 2013), pp. 306–312. ISSN: 1538-3873. DOI: 10.1086/670067. URL: <http://dx.doi.org/10.1086/670067>.
- [39] Jonathan Goodman and Jonathan Weare. “Ensemble samplers with affine invariance”. In: *Communications in Applied Mathematics and Computational Science* 5.1 (2010), pp. 65–80. DOI: 10.2140/camcos.2010.5.65.
- [40] Manfred Lindner et al. “Fermionic WIMPs and vacuum stability in the scotogenic model”. In: *Phys. Rev. D* 94.11 (2016), p. 115027. DOI: 10.1103/PhysRevD.94.115027. arXiv: 1608.00577 [hep-ph].
- [41] Florian Staub. “Exploring new models in all detail with SARAH”. In: *Adv. High Energy Phys.* 2015 (2015), p. 840780. DOI: 10.1155/2015/840780. arXiv: 1503.04200 [hep-ph].
- [42] Simon May. “minimal-lagrangians: Generating and studying dark matter model Lagrangians with just the particle content”. In: *Comput. Phys. Commun.* 261 (2021), p. 107773. DOI: 10.1016/j.cpc.2020.107773. arXiv: 2003.08037 [hep-ph].
- [43] W. Porod and F. Staub. “SPHeno 3.1: Extensions including flavour, CP-phases and models beyond the MSSM”. In: *Comput. Phys. Commun.* 183 (2012), pp. 2458–2469. DOI: 10.1016/j.cpc.2012.05.021. arXiv: 1104.1573 [hep-ph].
- [44] Geneviève Bélanger et al. “micrOMEGAs5.0 : Freeze-in”. In: *Comput. Phys. Commun.* 231 (2018), pp. 173–186. DOI: 10.1016/j.cpc.2018.04.027. arXiv: 1801.03509 [hep-ph].
- [45] F. Capozzi et al. “Status of three-neutrino oscillation parameters, circa 2013”. In: *Phys. Rev. D* 89 (2014), p. 093018. DOI: 10.1103/PhysRevD.89.093018. arXiv: 1312.2878 [hep-ph].
- [46] J. Adam et al. “New constraint on the existence of the $\mu^+ \rightarrow e^+ \gamma$ decay”. In: *Phys. Rev. Lett.* 110 (2013), p. 201801. DOI: 10.1103/PhysRevLett.110.201801. arXiv: 1303.0754 [hep-ex].

- [47] U. Bellgardt et al. “Search for the decay $\mu \rightarrow e+e+e$ ”. In: *Nuclear Physics B* 299.1 (1988), pp. 1–6. ISSN: 0550-3213. DOI: [https://doi.org/10.1016/0550-3213\(88\)90462-2](https://doi.org/10.1016/0550-3213(88)90462-2). URL: <https://www.sciencedirect.com/science/article/pii/0550321388904622>.
- [48] C. Dohmen et al. “Test of lepton-flavour conservation in $\mu \rightarrow e$ conversion on titanium”. In: *Physics Letters B* 317.4 (1993), pp. 631–636. ISSN: 0370-2693. DOI: [https://doi.org/10.1016/0370-2693\(93\)91383-X](https://doi.org/10.1016/0370-2693(93)91383-X). URL: <https://www.sciencedirect.com/science/article/pii/037026939391383X>.
- [49] Bernard Aubert et al. “Searches for Lepton Flavor Violation in the Decays $\tau^\pm \rightarrow e^\pm\gamma$ and $\tau^\pm \rightarrow \mu^\pm\gamma$ ”. In: *Phys. Rev. Lett.* 104 (2010), p. 021802. DOI: 10.1103/PhysRevLett.104.021802. arXiv: 0908.2381 [hep-ex].
- [50] Pauli Virtanen et al. “SciPy 1.0: Fundamental Algorithms for Scientific Computing in Python”. In: *Nature Methods* 17 (2020), pp. 261–272. DOI: 10.1038/s41592-019-0686-2.
- [51] Avelino Vicente and Carlos E. Yaguna. “Probing the scotogenic model with lepton flavor violating processes”. In: *JHEP* 02 (2015), p. 144. DOI: 10.1007/JHEP02(2015)144. arXiv: 1412.2545 [hep-ph].
- [52] Lawrence J. Hall et al. “Freeze-In Production of FIMP Dark Matter”. In: *JHEP* 03 (2010), p. 080. DOI: 10.1007/JHEP03(2010)080. arXiv: 0911.1120 [hep-ph].
- [53] Emiliano Molinaro, Carlos E. Yaguna, and Oscar Zapata. “FIMP realization of the scotogenic model”. In: *JCAP* 07 (2014), p. 015. DOI: 10.1088/1475-7516/2014/07/015. arXiv: 1405.1259 [hep-ph].
- [54] Amine Ahriche and Salah Nasri. “Dark matter and strong electroweak phase transition in a radiative neutrino mass model”. In: *JCAP* 07 (2013), p. 035. DOI: 10.1088/1475-7516/2013/07/035. arXiv: 1304.2055 [hep-ph].
- [55] Ricardo Cepedello et al. “Minimal 3-loop neutrino mass models and charged lepton flavor violation”. In: *JHEP* 08 (2020), p. 067. DOI: 10.1007/JHEP08(2020)067. arXiv: 2005.00015 [hep-ph].
- [56] Wolfram Research Inc. *Mathematica, Version 14.2*. Champaign, IL, 2025. URL: <https://www.wolfram.com/mathematica>.
- [57] David C. Lay, Steven R. Lay, and Judi J. McDonald. *Linear Algebra and Its Applications*. 5th ed. Harlow, UK: Pearson, 2016. ISBN: 978-0321982384.
- [58] Talal Ahmed Chowdhury and Salah Nasri. “Charged Lepton Flavor Violation in a class of Radiative Neutrino Mass Generation Models”. In: *Phys. Rev. D* 97.7 (2018), p. 075042. DOI: 10.1103/PhysRevD.97.075042. arXiv: 1801.07199 [hep-ph].

- [59] K. Afanaciev et al. “A search for $\mu^+ \rightarrow e^+$ with the first dataset of the MEG II experiment”. In: *Eur. Phys. J. C* 84.3 (2024). [Erratum: *Eur.Phys.J.C* 84, 1042 (2024)], p. 216. DOI: 10.1140/epjc/s10052-024-12416-2. arXiv: 2310.12614 [hep-ex].
- [60] A. Abdesselam et al. “Search for lepton-flavor-violating tau-lepton decays to $\ell\gamma$ at Belle”. In: *JHEP* 10 (2021), p. 19. DOI: 10.1007/JHEP10(2021)019. arXiv: 2103.12994 [hep-ex].
- [61] Osamu Seto, Tetsuo Shindou, and Takanao Tsuyuki. “Lower bounds on lepton flavor violating branching ratios in a radiative seesaw model”. In: *Phys. Rev. D* 105.9 (2022), p. 095018. DOI: 10.1103/PhysRevD.105.095018. arXiv: 2202.00931 [hep-ph].
- [62] Don van Ravenzwaaij, Peter Cassey, and Scott Brown. “A simple introduction to Markov Chain Monte–Carlo sampling”. In: *Psychonomic Bulletin Review* 25 (Mar. 2016). DOI: 10.3758/s13423-016-1015-8.
- [63] Cajo J. F. ter Braak. “A Markov Chain Monte Carlo version of the genetic algorithm Differential Evolution: easy Bayesian computing for real parameter spaces”. In: *Statistics and Computing* 16.3 (2006), pp. 239–249. DOI: 10.1007/s11222-006-8769-1.
- [64] David J. C. MacKay. *Information Theory, Inference, and Learning Algorithms*. Cambridge University Press, 2003. URL: <http://www.inference.org.uk/mackay/itila/>.
- [65] George Papamakarios et al. *Normalizing Flows for Probabilistic Modeling and Inference*. 2021. arXiv: 1912.02762 [stat.ML]. URL: <https://arxiv.org/abs/1912.02762>.
- [66] George Papamakarios, Theo Pavlakou, and Iain Murray. “Masked Autoregressive Flow for Density Estimation”. In: *Advances in Neural Information Processing Systems*. Ed. by I. Guyon et al. Vol. 30. Curran Associates, Inc., 2017. URL: https://proceedings.neurips.cc/paper_files/paper/2017/file/6c1da886822c67822bcf3679d04369fa-Paper.pdf.
- [67] Conor Durkan et al. *nflows: normalizing flows in PyTorch*. Version v0.14. Nov. 2020. DOI: 10.5281/zenodo.4296287. URL: <https://doi.org/10.5281/zenodo.4296287>.
- [68] Adam Paszke et al. “PyTorch: An Imperative Style, High-Performance Deep Learning Library”. In: *Advances in Neural Information Processing Systems (NeurIPS)*. Vol. 32. 2019. URL: https://papers.nips.cc/paper_files/paper/2019/hash/bdbca288fee7f92f2bfa9f70127Abstract.html.
- [69] Romain Bouchand and Alexander Merle. “Running of Radiative Neutrino Masses: The Scotogenic Model”. In: *JHEP* 07 (2012), p. 084. DOI: 10.1007/JHEP07(2012)084. arXiv: 1205.0008 [hep-ph].

Acknowledgements

First, I would like to thank Michael Klasen for the opportunity to write this thesis and his guidance during my work. I also thank Vishnu Padmanabhan Kovilakam for his constant support and his explanations of physics-related questions. Another special thanks goes to Luca Wiggering who helped me a lot with the installation and the usage of the computer tools I used.

To Adrian Finke and Daniel Woitaschek thank you for reading parts of my master thesis and helping me polish it.

I also would like to thank Jan Ravi Bade, Jannis Brirup, Adrian Finke, Luca Wiggering and Daniel Woitaschek for sharing an office with me. You made the time at the university really enjoyable.

Declaration of Academic Integrity

I hereby confirm that this thesis, entitled “Dark matter and vacuum stability in a 3-loop radiative seesaw model”, is solely my own work and that I have used no sources or aids other than the ones stated. All passages in my thesis for which other sources, including electronic media, have been used, be it direct quotes or content references, have been acknowledged as such and the sources cited. I am aware that plagiarism is considered an act of deception which can result in sanction in accordance with the examination regulations.

Münster, August 31, 2025

(signature of student)

I consent to having my thesis cross-checked with other texts to identify possible similarities and to having it stored in a database for this purpose.

I confirm that I have not submitted the following thesis in part or whole as an examination paper before.

Münster, August 31, 2025

(signature of student)